THE UNIVERSITY *of* LIVERPOOL

The Cerenkov Free Electron Laser

Thesis submitted in accordance with the requirements of the University of
Liverpool for the degree of Doctor of Philosophy

by

Christos Petichakis

July, 2003

Abstract

This thesis reports on an investigation into Cerenkov Free Electron Lasers. These devices are basically travelling wave tubes but having a dielectrically lined cylinder as the slow wave structure rather than a helix. If an electron beam is injected into the centre of this structure, an interaction between the electrons and the electromagnetic (e-m) TM_{01} mode can occur which can lead to amplification of the e-m wave.

Two different systems have been constructed. The first one was designed to operate as an oscillator at 12.4GHz and used a rectangular X-band waveguide microwave coupler. It was thought that the non-operation of this device could have been due to a lack of net gain, and so a second system was designed having a smaller diameter dielectric liner in order to achieve higher gain but at a slightly higher frequency of operation (16.9GHz). In both systems, the interception of the electron beam with the dielectric liner was small. Unfortunately, even though a maximum electron beam current of 120mA was achieved, leading to an expected small signal gain of 1200%, no microwave output was observed either. At this stage it was considered that there must be something more fundamental at fault with these systems.

After a thorough investigation, it was discovered that the small gap which always exists between the dielectric liner and the waveguide affected the dispersion relation of a Cerenkov system. Theoretically, gaps as small as 1% of the diameter of the waveguide were found to have a serious effect, and although these gaps would not stop the operation of the Cerenkov device, microwave output would only be expected at a voltage far from that expected. It was found that the problem could be overcome by coating the outer surface of the dielectric tube with a layer of conducting material, such as silver paint, which effectively removes the gap. Further tests of a Cerenkov free electron laser with this improvement are in progress.

Στον εαυτο μου!

Acknowledgments

Chiefly, I would like to thank my supervisor, Dr. R. A. Stuart for his continuous enthusiasm, encouragement and support throughout the duration of this course. His unique and distinctive way when explaining my questions helped me greatly to start understanding the micro-cosmos inside the Cerenkov system.

At the same time, I would like to express my appreciation to the valuable assistance I received from Dr. C. C. Wright. His practical experience, especially after building the first operational FEL in Liverpool, was most of the time welcomed but all the time useful.

Furthermore, I would like to thank Professor J. Lucas and Dr. A. I. Al-Shamma'a for providing me with all the required equipment and supporting me financially during my stay with the *Free Electron Laser and Microwave Applications Group*.

Also, I would like to thank all the other members of the group for their valuable comments and making my stay in the group most enjoyable.

Finally, and most importantly to me, I would like to thank my Mother – Stamatia, my Father – Manolis and my Sister – Fotini, for their support, understanding and total love.

Christos Pelichakis

July 2003

Contents

Chapter 1

Introduction

1.1. The Free Electron Laser project in Liverpool

The Liverpool Free Electron Laser (FEL) and Microwave Applications group first started research on FELs in 1987 [1]. Since that time, a substantial number of devices have been built and considerable knowledge and technical expertise has been acquired [2,3,4,5,6,7,8]. In all these systems, a wiggler magnet was used to allow an interaction between the electrons in the electron beam and an electromagnetic wave. The alternating direction of the field of the wiggler magnet transverse to the initial direction of the electrons causes them to be deflected from side to side. This controlled oscillation of the electrons allows them to radiate. This radiation is referred to as spontaneous emission and is very weak. However, if this radiation is trapped in a cavity, then, as it builds up, it reacts back onto the electron beam causing it to become "bunched". As each bunch of electrons undulates its way through the wiggler, the electrons now tend to radiate in phase with each other (and with other bunches since they are spaced one wavelength apart). This is what corresponds to the stimulated emission process in more standard lasers, and can lead to a greatly increased output.

It can be easily understood that the wiggler magnet is of vital importance for the successful operation of an FEL. However, the construction and setting up of a wiggler magnet is a very difficult, time consuming and cost-demanding task, because the individual permanent magnets from which it is constructed have to be very carefully selected and aligned. An FEL, which did not have to use a wiggler magnet, would have definite advantages.

Other types of FEL do exist. In fact, the helix travelling wave tube (TWT) [9,10] invented by Kompfner in 1944 can be thought of as an early FEL. The TWT consists of an electron beam and a slow wave structure to allow an interaction to take place. This slow wave structure (which replaces the wiggler) is a wire in the shape of a helix and its task is to reduce the velocity of the propagating e-m wave close to that of the electrons to allow them to interact. However, as in the case of the wiggler magnet, the helix TWT is delicate and difficult to construct, and power levels are limited.

The Cerenkov FEL does not require either a wiggler magnet or a helix for its operation. Its construction would then appear to be simplicity itself, consisting of a dielectric tube or liner fitted inside a copper pipe. The dielectric liner acts as the slow wave structure in this case, since the phase velocity of an electromagnetic wave propagating through the system will lie somewhere between the velocity in free space, c, and the velocity in a dielectric $c/\sqrt{\varepsilon_r}$ where ε_r is the dielectric constant of the liner. If the e-m wave has a longitudinal component of electric field, i.e. it has a TM character, then it is possible to obtain a TWT type interaction.

1.2. The Cerenkov radiation

In free space, the speed of light, c, is equal to 2.998 x 10^8 m/sec. In different materials, for example air, water or glass, light travels slower than in free space, and although particles can not move faster than the speed of light in free space, they can move faster than c/n, the speed of light in a substance whose index of refraction is n (n=speed of light in free space / speed of light in a substance). When an electrically charged particle moves through a substance at a speed exceeding the speed of light in the substance, a cone of light waves is emitted that corresponds to the bow wave produced by a ship moving through the water faster than water waves do or an aircraft travelling faster than the speed of sound. These light waves are known as *Cerenkov radiation* and form the basis of a method of determining the speed of such particles [11].

The principle of the Cerenkov radiation can be demonstrated by considering the analogy of an aircraft breaking the speed of sound, known as a sonic boom. Figure 1.1 shows an aircraft at point A travelling with a subsonic speed, u. It is clear that the waves surrounding the aircraft keep pace with the speed of the aircraft. However, in Figure 1.2, when the aircraft travels with a speed higher than the speed of sound u_m (Mach 1), the wavefronts (W1, W2) get concentrated along the surface of the cone. This cone signifies a shock wave and is referred to as the Mach cone.

A similar situation occurs in the case of an electron travelling inside a medium with a speed greater than the speed of light in the medium.

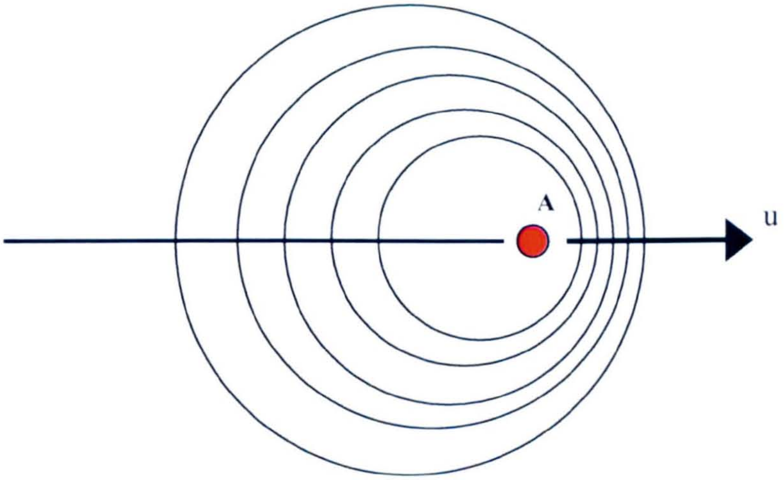

Figure 1.1. Pattern of the waves for an aircraft travelling below the speed of sound.

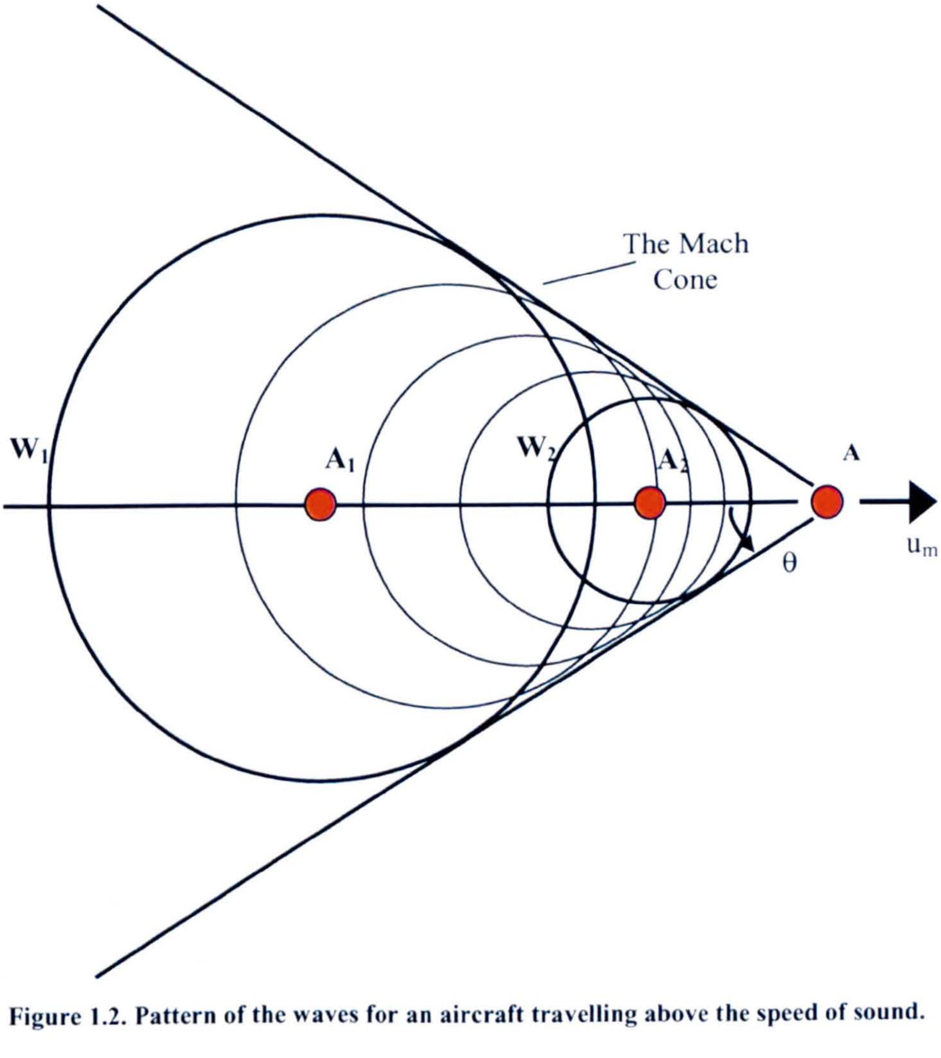

Figure 1.2. Pattern of the waves for an aircraft travelling above the speed of sound.

As Figure 1.3 shows, the envelope of the radiation is a cone of half angle θ with the particle at its apex moving with a speed u, and,

$$\sin(\theta) = \frac{(c/n)t}{ut} = \frac{c}{nu} \qquad 1.1$$

Equation 1.1 represents one of the most important results of the theory of Tamm and Frank [12], which shows that it is possible to produce radiation only after the condition u>c/n, i.e. the velocity of the particle exceeds the velocity of light in the medium. Also, when a beam of fast charged particles moves through a medium, the radiation can be detected and the angle θ measured, which makes it possible to determine the speed of the particle. Cerenkov radiation is visible as a bluish glow when an intense beam of particles is involved. This emission of blue light was observed by Cerenkov in 1934 from a bottle of water subjected to radioactive bombardment. However, Cerenkov claimed in his Nobel Lecture [13] in 1958, that it would be a mistake for him to claim that such a characteristic phenomenon had not been discovered earlier, instead he was convinced that it had been accidentally overlooked.

1.3. Thesis outline

The scope of this thesis is to detail the various stages of the design of a Cerenkov FEL both theoretically and experimentally. The theoretical part of this thesis is outlined in Chapter 2 where the dispersion relation of the system and the feedback oscillators are defined, together with the theoretical calculation of the small signal gain. In Chapter 4, the theoretical characteristics of circular and rectangular waveguides are analysed.

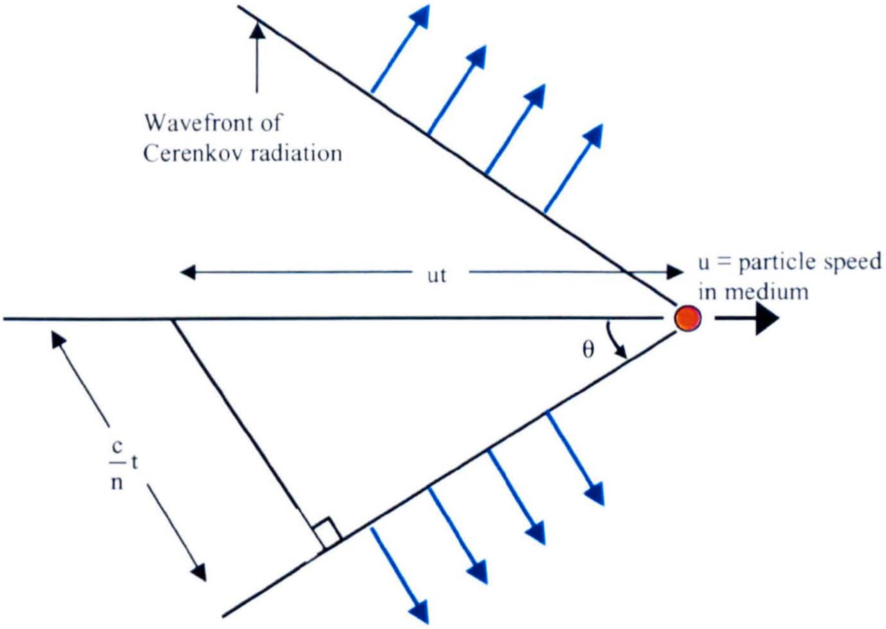

Figure 1.3. Schematic diagram of the Cerenkov effect.

Moving to the experimental part of the thesis, Chapter 3 describes the basic parts of the system. These include the vacuum layout, the electron gun and the circuitry used to accelerate the electron beam to 70 kV. Chapter 5 outlines the use made of a simulation package in the design of the cavities, while Chapter 6 reports on the very important task of focusing the electron beam and achieving efficient beam transportation through the loaded cavity. In this chapter, two different focusing devices are investigated and their advantages and disadvantages are documented. Chapters 7,8,9 and 10 describe the design process for two cavities intended for operation at 12.4GHz and 16.9GHz. The gain of each cavity was calculated and the electron beam transportation results are presented. Finally, Chapter 11 presents a detailed analysis of the dielectric liner characteristics and shows the importance of a good fit between the liner and the waveguide. The conclusions extracted from this chapter gave a sufficient explanation why both systems did not operate in the manner originally expected.

Chapter 2

Theory

2.1. The dispersion relation

The relationship between the frequency ω and the wavenumber β, the so-called dispersion relationship depends on,

a. The geometry of the guide - whether cylindrical or rectangular for example.
b. The dimensions of the guide, and
c. The dielectric material filling the guide.

In the last case, two different conditions can be distinguished determined by whether the dielectric completely fills the waveguide or not.

In free space, the dispersion relation of an electromagnetic wave is given by,

$$\omega^2 = c^2\beta^2 \qquad 2.1$$

where c is the speed of light in free space.

Equation 2.1 leads to $\omega = \pm c\beta$ which represents both a "forward" TEM (transverse electromagnetic) mode with $\omega = c\beta$ that travels in the positive direction of the axis, and a "reverse" mode with $\omega = -c\beta$. The forward dispersion relation $\omega = c\beta$ is also known as the vacuum light line.

However, inside a waveguide the dispersion relation changes to,

$$\omega^2 = \omega_{co}^2 + c^2\beta^2 \qquad 2.2$$

An extra factor needs to be incorporated since a guided wave has a cut off frequency ω_{co} below which it is not possible to transmit any power down the guide at all. The cut off frequency is normally of the form $c\frac{2\pi}{d}$ where d is the length related to the dimensions of the guide. Figure 2.1 illustrates a typical example of a dispersion relation diagram.

If the guide is completely filled with a dielectric medium rather than vacuum, both the wavenumber term $c\beta$ and the cut off frequency change. This is due to the fact that the velocity of a TEM mode is reduced in a dielectric medium to $c/\sqrt{\varepsilon_r}$, where ε_r is the dielectric constant of the medium. Consequently, the dispersion relation for a fully loaded guide changes to,

$$\omega^2 = \left(\frac{\omega_{co}}{\sqrt{\varepsilon_r}}\right)^2 + \left(\frac{c}{\sqrt{\varepsilon_r}}\right)^2 \beta^2 \qquad 2.3$$

The last case we consider is when the waveguide is only partially filled with a dielectric tube liner. This is the case of importance as far as Cerenkov devices are concerned, since the dielectric liner has to be hollow to allow the electron beam to pass through. For this case, the calculation of the dispersion relationship is a good deal more complex. When Maxwell's equations are solved, the Bessel function solutions must be matched in the vacuum and dielectric regions simultaneously. In order to solve these differential equations, a program was written by R.A. Stuart [14] using the MathCAD package [15]. It would be expected that the dispersion curve for this case lies between the empty and fully loaded guide curves. Figure 2.2 shows the dispersion curves for a cylindrical waveguide for all three cases and confirms the expected result. The dielectric constant of the medium used in Figure 2.2 was equal to 10 (corresponding to approximately to alumina).

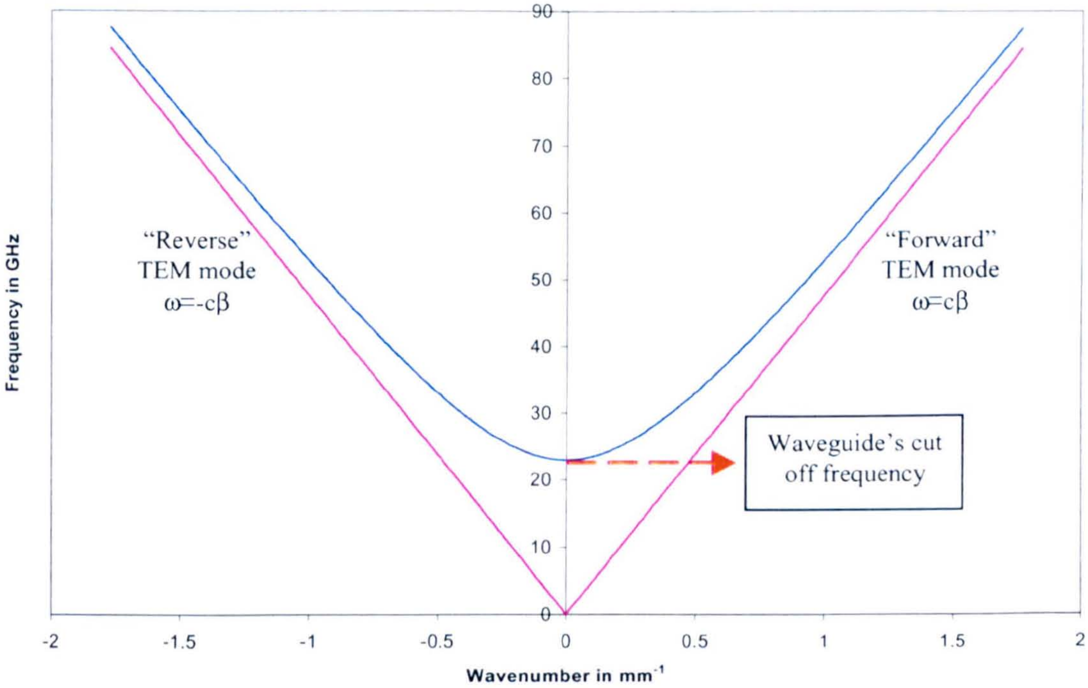

Figure 2.1. A typical waveguide dispersion relation.

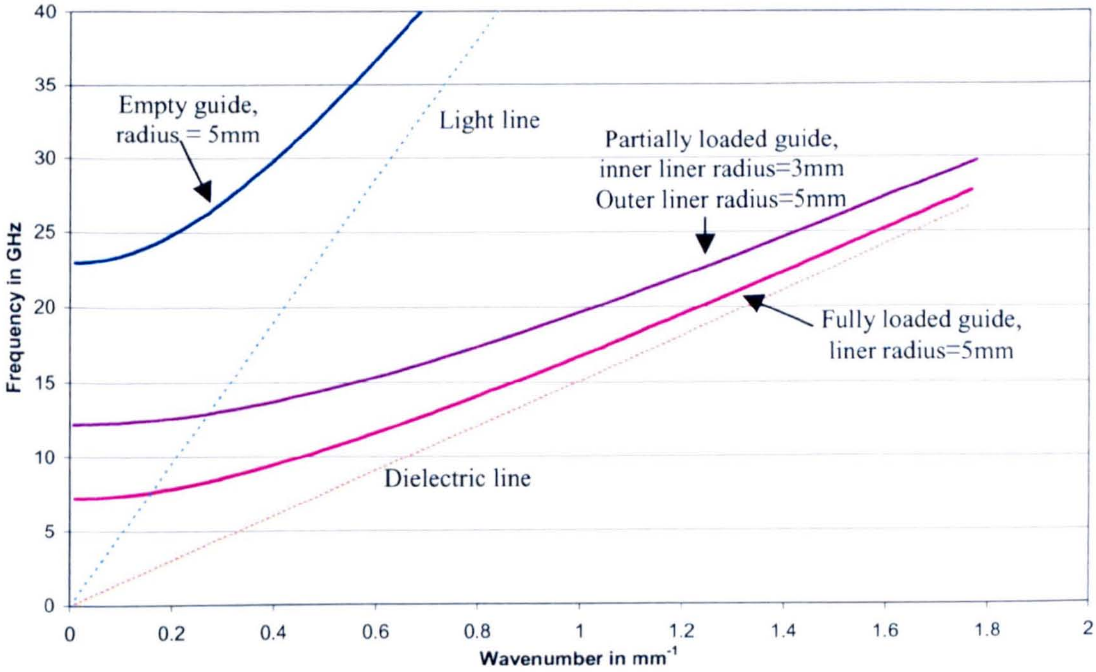

Figure 2.2. Dispersion relations for an empty, partially loaded and fully loaded waveguide.

2.2. Feedback oscillators

A block diagram of a feedback oscillator [16] can be seen in Figure 2.3. It consists of a forward gain block and a feedback path. For such a system to start oscillating, two conditions must be satisfied, known as the Barkhausen criteria. Firstly, the product of the amplifier's gain, A, and the fraction of the output fed back to the input, β, must be at least equal to unity, $A \bullet \beta \geq 1$. In other words, the gain must be greater than the system losses, 1/β. Secondly, the phase change in going round the loop must be 0, or 360° etc., so that constructive interference can take place, $\angle A + \angle \beta = 0$. If these conditions are satisfied at any particular frequency, the system will then start to oscillate at this frequency. If these oscillations start from noise, then we must have $A \bullet \beta > 1$ in order for the oscillation to grow. The gain A, here, is the small signal gain of the system, A_{ss}. Since the oscillation cannot grow forever, eventually non-linear processes will set in and reduce the gain below its small signal value. Eventually, saturation will be reached, when the output reaches its maximum, stable value and $A \bullet \beta = 1$.

A Cerenkov FEL can be viewed as a feedback oscillator. The closed cavity of the FEL acts as the feedback circuit, as it forces the trapped microwave power to return from the output back to the input. The attenuation of the waveguide /dielectric liner ensure that the feedback fraction β is less than 1. The forward gain of the system is provided by the electronic interaction. Figure 2.4 illustrates this situation. The calculation of the small signal gain for a Cerenkov FEL, A_{ss}, which controls whether the oscillations can grow from noise or not will be illustrated in the next section.

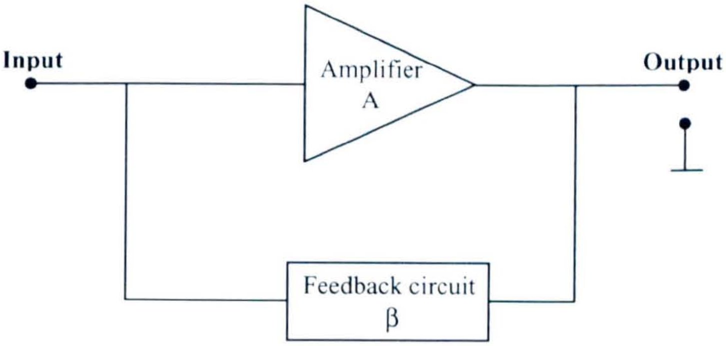

Figure 2.3. Block diagram of a feedback oscillator.

Figure 2.4. The feedback and amplification process of the FEL power.

2.3. The system gain calculation

The waveguide structure shown in Figure 2.5 is assumed for a TM_{01} mode of frequency ω and wavenumber β.

Along the z axis at the centre of the guide, it is assumed that the only field is,

$$E_z(z,t) = E_{z0}\cos(\omega t - \beta z) \qquad 2.4$$

with the other components E_r, E_ϕ, H_z, H_r, H_ϕ being zero.

Conservation of energy for an electron injected into the guide requires that,

$$\frac{d}{dt}\left(\gamma mc^2\right) = -eE_z u \qquad 2.5$$

where u is the electron velocity, m is the mass of the electron, e is the electron charge and γ is the electron energy and can be calculated using Equation 2.6 as follows,

$$\gamma = 1 + \frac{V_{acc}}{511} \qquad 2.6$$

where V_{acc} is the system's accelerating voltage in kVs.

Instead of considering an electron beam as composed of electrons entering the waveguide at a set of different times $\{t_i\}$ uniformly spaced over one period of electromagnetic wave, it is assumed that each electron enters at t=0 but the phase of the electromagnetic mode is different for each electron $\{\phi_i\}$, distributed uniformly over the range from 0 to 2π.

Hence,

$$\frac{d}{dt}\left(\gamma mc^2\right) = -euE_{z0}\cos(\omega t - \beta z + \phi_i) \qquad 2.7$$

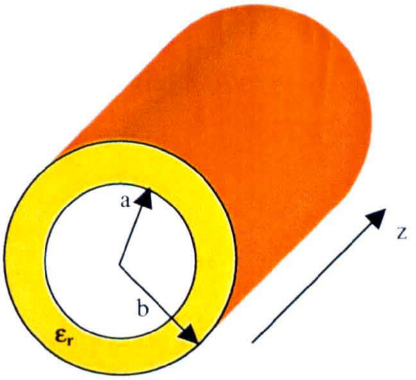

Figure 2.5. The cylindrical waveguide geometry.

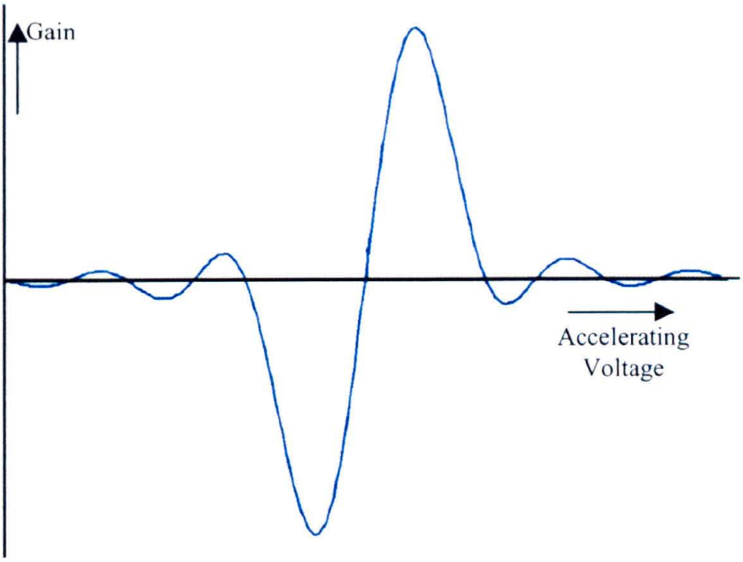

Figure 2.6. The gain characteristic curve.

or $\frac{d\gamma}{dt} = \frac{-e}{mc^2} uE_{z0} \cos(\omega t - \beta z + \phi_i)$

If E_{z0} is small, then the changes in γ and u over an interaction length L are small, so that it is possible to put approximately,

$$\frac{d\gamma}{dt} = \frac{-e}{mc^2} u_{z0} E_{z0} \cos(\omega t - \beta u_{z0} t + \phi_i) \tag{2.8}$$

where u_{z0} is the initial velocity of each electron entering the interaction zone. Integrating the expression above over a length L gives,

$$\gamma(L) - \gamma(0) = \frac{-e}{mc^2} u_{z0} E_{z0} \int_0^{L/u_{z0}} \cos[(\omega - \beta u_{z0})t + \phi_i] dt$$

$$\text{i.e. } \gamma(L) - \gamma(0) = \frac{-e}{mc^2} u_{z0} E_{z0} \left. \frac{\sin[(\omega - \beta u_{z0})t + \phi_i]}{(\omega - \beta u_{z0})} \right|_0^{L/u_{z0}}$$

Setting $\omega - \beta u_{z0} = \Delta\omega$ gives

$$\gamma(L) - \gamma(0) = \frac{-e}{mc^2} u_{z0} E_{z0} \frac{\left[\sin\left(\Delta\omega \frac{L}{u_{z0}} + \phi_i \right) - \sin(\phi_i) \right]}{\Delta\omega} \tag{2.9}$$

Madey's theorem [17,18] requires $\left\langle [\gamma(L) - \gamma(0)]^2 \right\rangle$ to be found i.e. the change in rms energy averaged over ϕ_i.

Now,

$$[\gamma(L)-\gamma(0)]^2=\left(\frac{e}{mc^2}\right)^2\frac{u_{z0}^2E_{z0}^2}{(\Delta\omega)^2}\left\{\sin^2\left(\Delta\omega\frac{L}{u_{z0}}+\phi_i\right)-2\sin\left(\Delta\omega\frac{L}{u_{z0}}+\phi_i\right)\sin(\phi_i)+\sin^2(\phi_i)\right\}$$

With $\left\langle\sin^2(a+\phi_i)\right\rangle=\frac{1}{2}$ then,

$$\left\langle[\gamma(L)-\gamma(0)]^2\right\rangle=\left(\frac{e}{mc^2}\right)^2\frac{u_{z0}^2E_{z0}^2}{(\Delta\omega)^2}\left\{\frac{1}{2}-2\left\langle\sin\left(\Delta\omega\frac{L}{u_{z0}}+\phi_i\right)\sin(\phi_i)\right\rangle+\frac{1}{2}\right\}$$

and using $\sin(x)\sin(y)=\frac{1}{2}[-\cos(x+y)+\cos(x-y)]$ we get

$$\left\langle[\gamma(L)-\gamma(0)]^2\right\rangle=\left(\frac{e}{mc^2}\right)^2\frac{u_{z0}^2E_{z0}^2}{(\Delta\omega)^2}\left\{1-2\left\langle\frac{1}{2}\left[\cos\left(\Delta\omega\frac{L}{u_{z0}}\right)-\cos\left(\frac{\Delta\omega L}{u_{z0}}+2\phi_i\right)\right]\right\rangle\right\}$$

But $\left\langle\cos(a+\phi_i)\right\rangle=0$ and hence,

$$\left\langle[\gamma(L)-\gamma(0)]^2\right\rangle=\left(\frac{e}{mc^2}\right)^2\frac{u_{z0}^2E_{z0}^2}{(\Delta\omega)^2}\left\{1-\cos\left(\Delta\omega\frac{L}{u_{z0}}\right)\right\}.$$

Using $1-\cos(a)=2\sin^2\left(\frac{a}{2}\right)$ gives,

$$\left\langle[\gamma(L)-\gamma(0)]^2\right\rangle=\left(\frac{e}{mc^2}\right)^2\frac{u_{z0}^2E_{z0}^2}{(\Delta\omega)^2}2\sin^2\left(\frac{\Delta\omega L}{2u_{z0}}\right)$$

which leads to,

$$\left\langle[\gamma(L)-\gamma(0)]^2\right\rangle=\frac{1}{2}\left(\frac{e}{mc^2}\right)^2E_{z0}^2L^2\,\mathrm{sinc}^2\left(\frac{\Delta\omega L}{2u_{z0}}\right) \qquad 2.10$$

Madey's theorem states that,

the average energy change per electron $\equiv\left\langle[\gamma(L)-\gamma(0)]\right\rangle=\frac{1}{2}\frac{d}{d\gamma}\left\langle[\gamma(L)-\gamma(0)]^2\right\rangle$.

Then conservation of energy gives the gain as,

$$\text{Gain} = \frac{\Delta P}{P_0} = \frac{-\langle[\gamma(L)-\gamma(0)]\rangle mc^2 \frac{I}{e}}{P_0} \qquad 2.11$$

since I/e is the number of electrons entering the cavity per second.

Now,

$$\langle[\gamma(L)-\gamma(0)]\rangle = \frac{1}{2}\frac{d}{d\gamma}\left\{\frac{1}{2}\left(\frac{e}{mc^2}\right)^2 E_{z0}^2 L^2 \sin c^2\left(\frac{\Delta\omega L}{2u_{z0}}\right)\right\} \qquad 2.12$$

Remembering that ω and β and hence E_{z0} are fixed, only u_{z0} varies with γ and therefore,

$$\langle[\gamma(L)-\gamma(0)]\rangle = \frac{1}{4}\left(\frac{e}{mc^2}\right)^2 E_{z0}^2 L^2 \frac{d}{d\gamma}\left\{\sin c^2\left(\frac{(\omega-\beta u_{z0})L}{2u_{z0}}\right)\right\}$$

By letting $\frac{(\omega-\beta u_{z0})L}{2u_{z0}} = \left(\frac{\omega}{u_{z0}}-\beta\right)\frac{L}{2} = \Delta\beta\frac{L}{2}$

then,

$$\langle[\gamma(L)-\gamma(0)]\rangle = \frac{1}{4}\left(\frac{e}{mc^2}E_{z0}L\right)^2 \frac{d}{d\left(\frac{\Delta\beta L}{2}\right)}\left[\sin c^2\left(\frac{\Delta\beta L}{2}\right)\right]\frac{d}{d\gamma}\left(\frac{\Delta\beta L}{2}\right) \qquad 2.13$$

Now, $\frac{d}{d\gamma}\left(\frac{\Delta\beta L}{2}\right) = \frac{d}{d\gamma}\left\{\left(\frac{\omega}{u_{z0}}-\beta\right)\frac{L}{2}\right\} = \frac{-\omega}{u_{z0}^2}\frac{L}{2}\frac{du_{z0}}{d\gamma}$

But $u_{z0} = c\sqrt{1-\frac{1}{\gamma^2}}$ and hence

$$\frac{du_{z0}}{d\gamma} = \frac{c}{2\sqrt{1-\dfrac{1}{\gamma^2}}}\frac{-(-2)}{\gamma^3} = \frac{c^2}{u_{z0}\gamma^3}$$

and $$\frac{d}{d\gamma}\left(\frac{\Delta\beta L}{2}\right) = \frac{-\omega}{u_{z0}^2}\frac{L}{2}\frac{c^2}{u_{z0}\gamma^3} = \frac{-1}{2}\frac{\omega L c^2}{u_{z0}^3\gamma^3} = \frac{-1}{2}\frac{\omega L}{c}\frac{1}{\beta_{z0}^3\gamma^3}$$

where $\beta_{z0} = \dfrac{u_{z0}}{c}$,

so that,

$$\langle[\gamma(L)-\gamma(0)]\rangle = \frac{1}{4}\left(\frac{e}{mc^2}E_{z0}L\right)^2 \frac{d}{dx}\operatorname{sinc}^2(x)\Big|_{x=\frac{\Delta\beta L}{2}}\left(\frac{-1}{2}\frac{\omega L}{c\beta_{z0}^3\gamma^3}\right)$$

Consequently the gain is,

$$\frac{\Delta P}{P_0} = \frac{1}{8}\left(\frac{e}{mc^2}\right)\left(\frac{E_{z0}^2}{P_0}\right)L^3\frac{\omega}{c\beta_{z0}^3\gamma^3}I\frac{d}{dx}\operatorname{sinc}^2(x)\Big|_{\frac{\Delta\beta L}{2}}$$

Plotting the gain against the accelerating voltage of the system gives the graph shown in Figure 2.6. The point where the maximum gain can be achieved is the required accelerating voltage that has to be used by the system.

Chapter 3

The Basic System

3.1. Introduction

This chapter will describe the basic apparatus used to set up a Cerenkov Free Electron Laser system. By basic system is meant all the components that compose the equipment with the exception of the loaded circular waveguide, which is the heart of the Cerenkov laser itself and is described separately. The components of the basic system are the electron gun, the beam current measuring system, the vacuum apparatus and the way all these components are connected together and how they are controlled in general. The description of the electron gun and its associated devices can best be analyzed by using a circuit diagram where each component is clearly marked. For the case of the vacuum system, it is easier to use a block diagram explaining the utility of each component. The components of this basic were the first parts of this project to be constructed and care was needed to ensure that the dielectrically loaded waveguide and the microwave coupler could be finally fitted in to this system without any problems.

3.2. The circuit

The electrical circuit diagram describing the major parts of the gun electronics can be seen in Figure 3.1. The heater that thermally activates the electrons from the cathode is controlled by a VARIAC, which provides the heater with from 0 to 6.3Vac. A high voltage switch connects the electron gun cathode to a variable voltage supply providing a first anode to cathode accelerating voltage of between 0 and 10 kV. The size of this voltage controls the magnitude of the electron beam current. A standard laboratory pulse generator controls the switch. The first anode of the system is grounded while the second anode is at high voltage (70kV). This further accelerates the electrons generated by the pulse applied to the cathode – first anode electrodes. The cavity through which the beam passes and the solenoid used to control the electron beam were also held at this high voltage. A Spellman (SL 1200) power supply was used for this purpose. It can supply 130 kV at up to 9.0 mA. In order to provide electron beam current greater than 9.0mA, an energy storage system incorporating a 0.0625 μF capacitor charged via a 25 MΩ resistor was used. Such a large resistor is used to limit the power supply current to a safe level of 3 mA in the event of a breakdown taking place. The capacitor when fully charged is discharged through the 800Ω resistor by means of the pulse on the high voltage switch which causes the electron beam current to flow. As the capacitor discharges, the second anode voltage droops at a rate given by $C\frac{dV}{dt} = I$ so that if the beam current I is 100 mA for example then the droop rate is only 1.6 V/μs, so that pulses of up to 100 μs long can be achieved with only 0.2% drop in voltage over the duration of the pulse. The 800Ω resistor limits the maximum discharge current to 90 A in the event of a breakdown between the cathode and first anode and therefore also acts as a protective device for the electron gun.

3.3. The electron gun

To set an electron free from its rest state in a material, sufficient kinetic energy must be given to allow the electron overcome the potential energy and escape from the surface of the material. A way of achieving this is by thermionic emission, which involves heating the cathode of the electron gun. However, to prevent the emitted electrons from accumulating around the cathode which would prevent further electrons being emitted, it is necessary to use an anode held at a positive voltage relative to the cathode. The current from a cathode of area A to an anode separated by a distance s and potential V, is described by the Child-Langmuir Law [19],

$$I = P \cdot V^{3/2} \qquad \text{3-1}$$

where, for planar geometry, P, is given by $\frac{4}{9}\varepsilon_0\left(\frac{2e}{m}\right)^{1/2}\frac{A}{s^2}$, and is known as the perveance. In other geometries a similar relationship holds with the perveance depending on the shape of the cathode and its relative position to the anode. The specification for the Cerenkov Free Electron Laser required an electron beam current of 120mA at an acceleration voltage of 70kV. Stuart, in [20], first suggested and provided the design for this type of 2 anode electron gun. The first anode is grounded (positive voltage with respect to the anode) and controls the electron beam current, while the second anode is at high voltage (70 kV) and controls the acceleration voltage. Further design details are given in [3].

The basic gun as provided by EEV was capable of supplying 285 mA, with a first anode to cathode voltage of 9.1 kV. Using Child-Langmuir space charge law, the perveance of this gun is then equal to 0.328 μpervs. For the specification of our CFEL, the required current is 120 mA and therefore, the voltage supplied to the cathode should be around -5.2 kV.

3.3.1. Activation of the electron gun

To activate the gun after it has been installed in the system, a gradual increase of the voltage applied to the heater is recommended. Increasing the voltage in steps of 0.35V every 10 minutes, which is enough time for the vacuum to recover, was the procedure recommended by EEV [21]. Figure 3.2 shows a graphical representation of the activation process. The left hand y-axis shows the voltage applied to the VARIAC varying from 0 to 222, which corresponds to 0 to 6.3 Volts applied to the heater. The right hand y-axis shows the corresponding variation of the vacuum pressure.

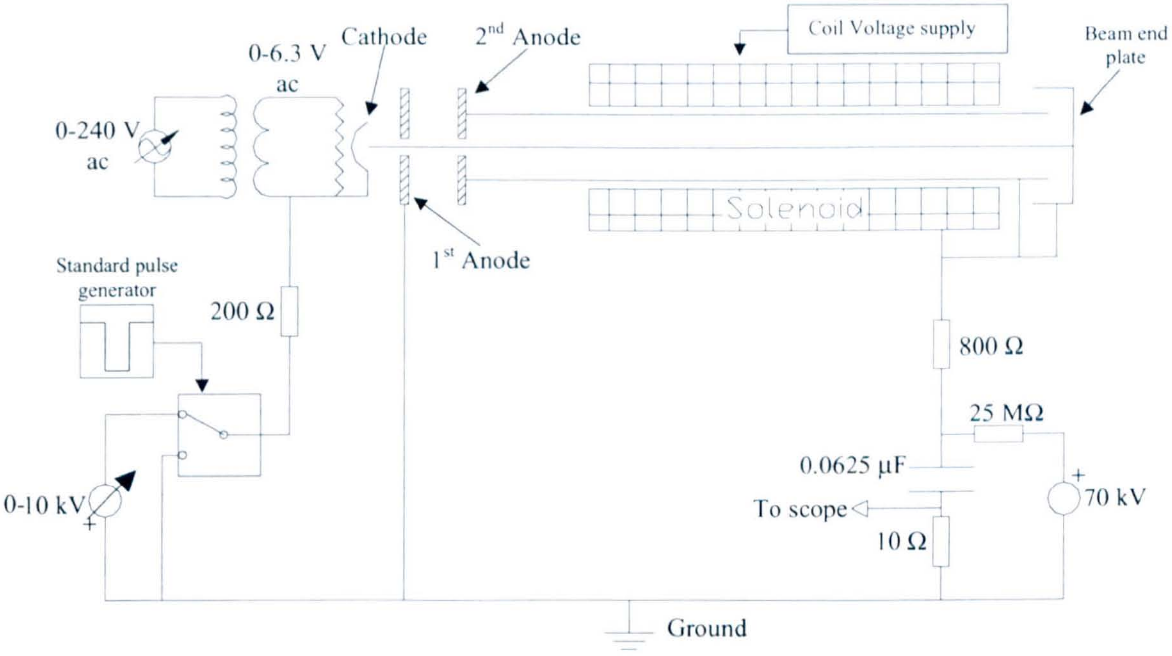

Figure 3.1. Circuit of the main parts of the base system.

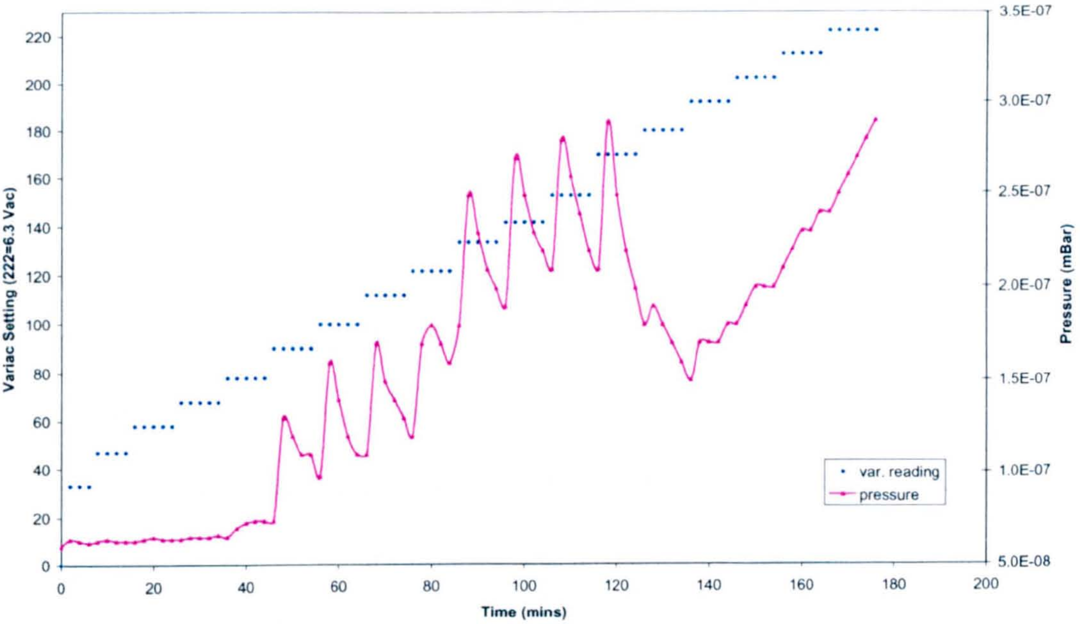

Figure 3.2. Activation of the electron gun.

6.3 Volts is the recommended heater voltage for this gun. From the graph in Figure 3.2, it can be seen that the activation procedure lasted about 3 hours. During this period, two different processes were in progress in parallel. The first one was the burn off of the oxides (like barium – $BaCO_3$) on the surface of the cathode releasing carbon dioxide ($BaCO_3 \rightarrow BaO + CO_2$) and affecting dramatically the vacuum pressure. It can be seen that shortly after the heater voltage was raised the pumps were able to reduce the pressure to a lower value. However because the envelope of this electron gun is also rising in temperature causing it to de-gas, there is a gradual rise of pressure in the background. By switching off the heater and leaving the system off overnight, the next day, vacuum pressure had recovered to a level of around 10^{-8} mbar, which was an acceptable pressure for the operation of the system.

3.4. Measuring the electron beam current

In order to be able to check how much of the electron beam could be transported through the whole length of the loaded cavity, it was important to be able to have an accurate value for both the current leaving the electron gun (input current) and the current reaching the beam end plate (output current).

To measure the input current, a 10 Ω resistor was added between the high voltage capacitor and the ground point of the circuit, as shown in Figure 3.1. The voltage across this resistor was recorded using an oscilloscope. To measure the output current reaching the beam end plate was more difficult, as this part of the system is raised to 70 kV. A light emitting diode whose light output was proportional to the current through it was connected between the beam end plate and the high voltage supply, and its light output was detected by a photodiode at the end of a fibre optic cable, which also provided the high voltage isolation. The output of the photodiode was observed on the oscilloscope. In order to be able to convert the oscilloscope reading to a corresponding current value, the system was calibrated. Figure 3.3 shows the results of the calibration procedure. As expected a reasonably linear variation was observed.

3.5. The vacuum system

To achieve a substantial amount of electron beam transportation through a 600 mm long cavity it is important to construct a reliable vacuum system capable of achieving pressures in the ultra high vacuum region ($>10^{-8}$ millibar). For the CFEL, two different pumps connected in series were used. The first pump is a METROVAC rotary pump, which takes the system from atmospheric pressure down to 10^{-2} mbar and hence provides the right condition for the engagement of the turbo molecular pump. The Leybold Turbo Vac 361 turbo molecular pump uses high speed rotating turbine blades (45000 revs/min) and is capable of pumping out 360 litres/sec [22]. During the operation of the turbo molecular pump, the rotary pump acts as a backing pump.

Two different gauges monitor the performance of the vacuum in the system. The first one is a pirani gauge [23] and is connected close to the rotary pump. It measures system pressures from atmospheric down to 10^{-3} mBar. To measure higher vacuum levels, an ion gauge is used. This type of gauge is based on the Bayard-Alpert (B-A) ionisation gauge [24,25] and as it is very fragile, extra care must be taken when it is installed. The ion gauge is positioned close to the electron gun. The ion gauge consists of a tungsten filament surrounded by a grid and it is capable of measuring pressures down to the ultra high vacuum region (from 10^{-3} up to 10^{-11} mBar). The B-A ionisation gauge used in the CFEL can be seen in Figure 3.4. Both the pirani and the ion gauge are electronically controlled by an ultra high pressure gauge control unit [26], which can accommodate up to 2 pirani gauges and one ion gauge. This unit monitors and displays continuously the pressure level and has a leak detector with volume controlled audio output to warn the user.

Apart from the pumps and the gauges the vacuum system consists of three valves. Between the rotary and the turbo molecular there are two valves. The first one shown in Figure 3.5 as "Safe Valve 1", allows the user to see whether the pirani and the rotary pump are operating as expected. The second valve shown as "Safe Valve 2", protects the vacuum system from a sudden power failure. Its job is to shield and isolate the turbo molecular pump and the rest of the vacuum system and maintain a high-vacuum condition. The third valve shown as "nitrogen valve" provides a way of allowing nitrogen inside the system. This is useful in case the whole system is required to be at atmospheric pressure in order to repair or replace a component, when it is important to flood the interior of the whole system with dry nitrogen.

The electron gun and the ion gauge are then protected from attack by air and water molecules.

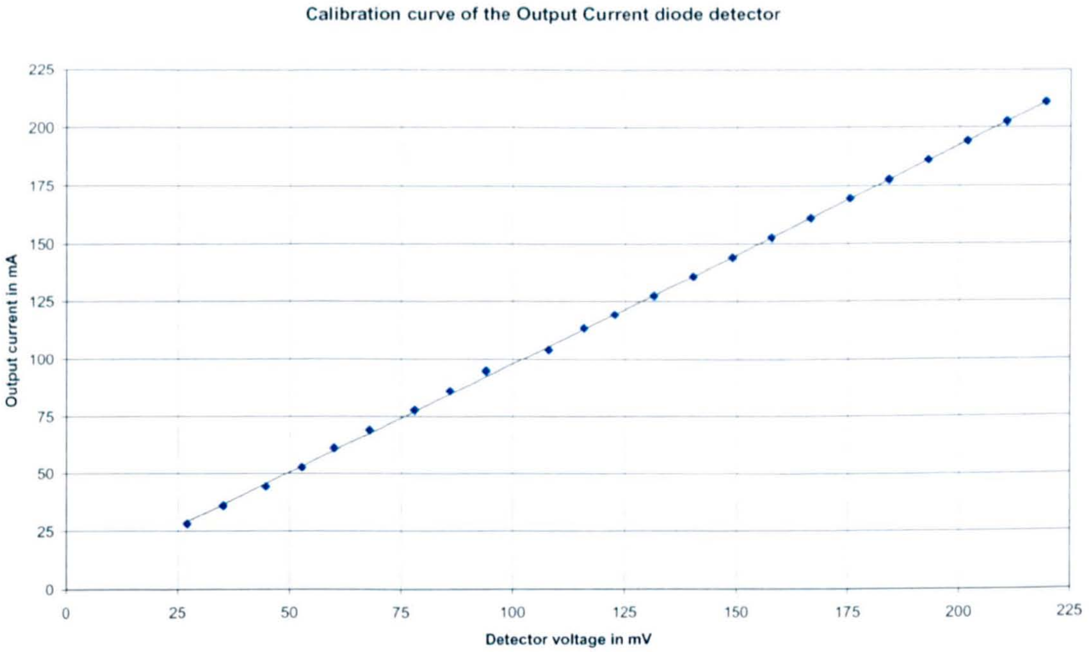

Figure 3.3. Graph for calculating the current reaching the top end of the loaded cavity.

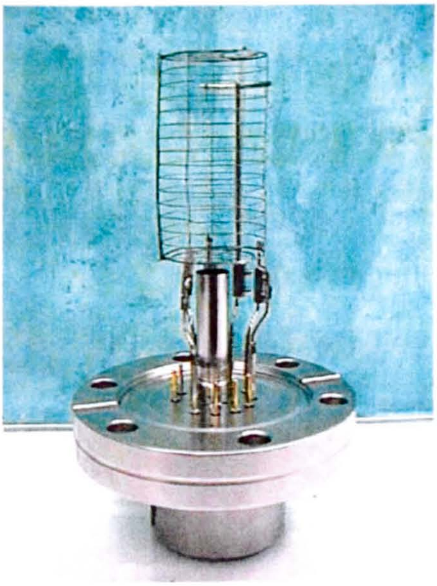

Figure 3.4. The B-A ionization gauge.

3.5.1. The process of pumping down the system

The time taken for the system pressure to reduce from atmospheric pressure to the ultra high vacuum region is known as the "pump down cycle". This time does not exclusively depend on the pump's capacity. Equally important is the type of material used to make the system and how clean it is. Materials such as stainless steel, copper, bronze and aluminium have low vapour pressures and are good ultra high vacuum construction materials [27]. Figure 3.6 illustrates the time taken to pump down the CFEL. It can be seen that the rotary pump reaches its target pressure of about 10^{-2} mBar (almost zero in RHS scale) in about 6 minutes and as soon as the turbo molecular pump is engaged the pressure falls extremely rapidly to 10^{-5} mBar (see left hand scale). Then it takes approximately 3 hours to reach the ultra high vacuum region at pressures levels of about 10^{-8} mBar. This curve represents the pumping cycle for a "clean" system. Pumping times could of course be much larger for a system just built.

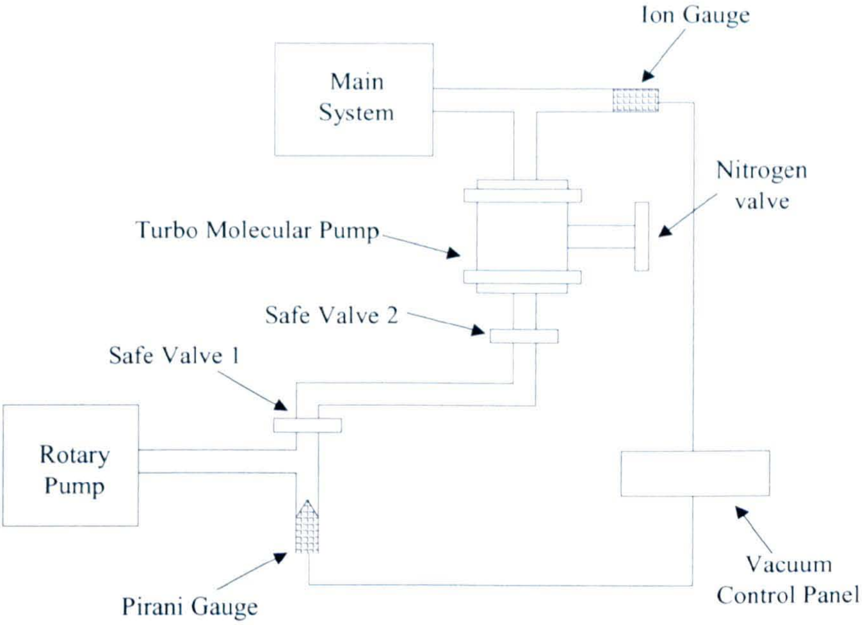

Figure 3.5. The vacuum system block diagram.

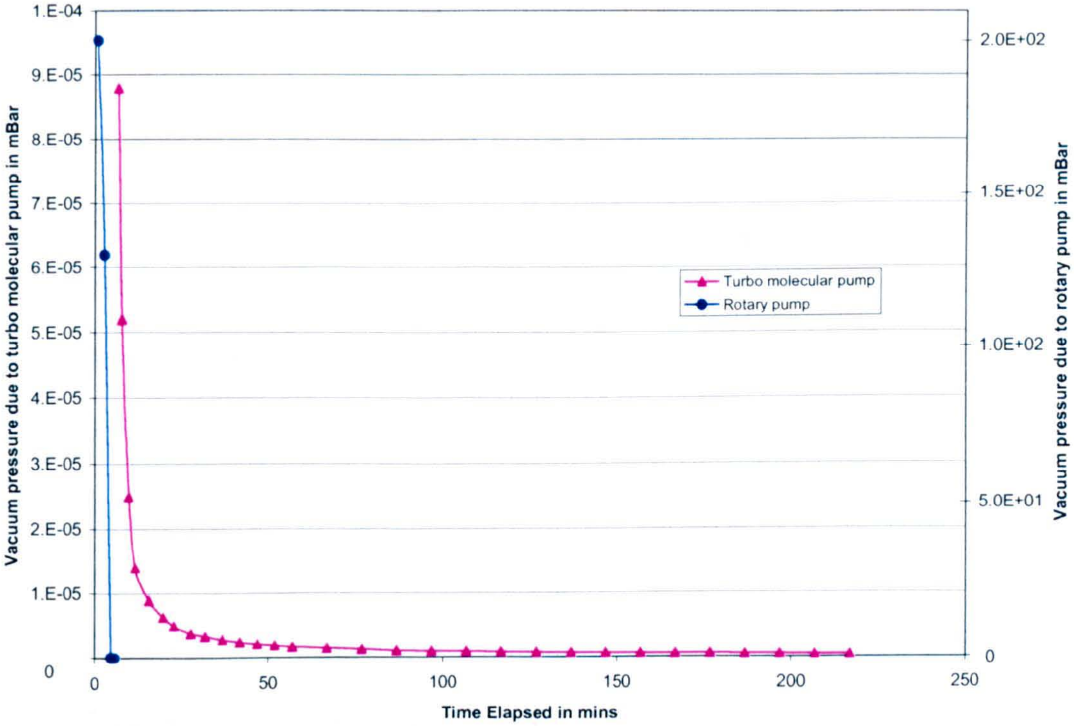

Figure 3.6. The vacuum pump down cycle.

Chapter 4

Microwave Waveguides and their Characteristics

4.1. Introduction

Transmission lines and coaxial cables are common structures used to transfer e-m energy from one point (a source) to the other (a load). These structures are ideal for low frequencies. However, in the microwave frequency range (from 3 to 300 GHz) these two transmission structures become lossy and consequently inefficient. In transmission lines, some energy escapes by radiation, as the fields are not confined in all directions, as shown in Figure 4.1. In the coaxial cable case, although the metal outer confines the fields, dielectric losses become significant as the frequency increases (Figure 4.2).

A waveguide is an alternative method of transporting e-m energy more efficiently than transmission lines or coaxial cables at high frequencies. Although waveguides can take many shapes, the most common waveguides are either rectangular (Figure 4.3) or circular (Figure 4.4) and consist basically of hollow metal tubes of uniform cross section.

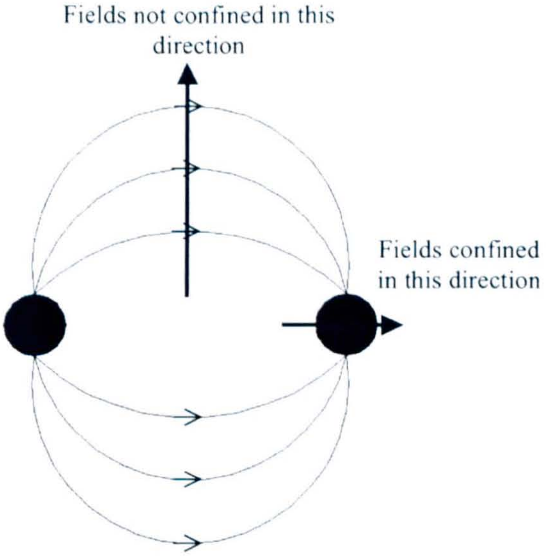

Figure 4.1. End view of a transmission line.

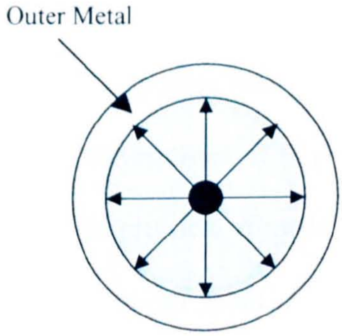

Figure 4.2. End view of a coaxial cable

(fields confined in all directions).

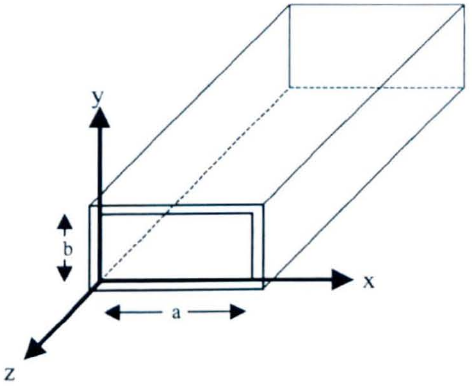

Figure 4.3. The rectangular waveguide structure.

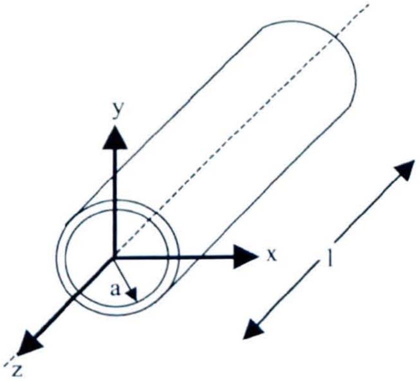

Figure 4.4. The circular waveguide structure.

The electric and magnetic fields associated with the electromagnetic wave are then confined to the space within the guides and consequently no power is lost due to radiation leakage. Since the guides are normally filled with air or can be evacuated, dielectric losses are also negligible. However, there is some I^2R power lost to heat in the walls of the guides, but this loss is usually very small. In waveguides, it is possible to propagate different "modes" or patterns of e-m waves. The physical dimensions of a waveguide determine what is known as the cutoff frequency for each mode. If the frequency of the signal is above this cutoff frequency for a given mode, the electromagnetic energy can be transmitted through the guide for that particular mode with minimal attenuation. On the other hand, if the electromagnetic energy has a frequency below cutoff for that particular mode, the electromagnetic wave will not propagate down the waveguide and is completely reflected.

4.2. Modes in a waveguide

As stated above, it is possible to propagate several modes of electromagnetic waves down a guide. Each of these modes corresponds to different solutions of Maxwell's equations for each particular waveguide each having its own frequency. The mode with the lowest cut off frequency is called the dominant mode.

The two most common categories of modes inside a waveguide are,

1. Transverse Magnetic (TM) mode: this mode is characterized by the existence of an electric field component in the direction of the wave propagation with zero magnetic

field in the same direction. Consequently the magnetic field lies entirely in the plane transverse to the direction of propagation of the wave.

2. Transverse Electric (TE) mode: This is similar to the TM mode but with the electric field now being purely transverse.

The Table 4.1 below explains the subscripts used for the identification of each mode ($TM_{m,n}$ and $TE_{m,n}$), in rectangular and circular waveguides.

Waveguide	**Subscript**	
	m	n
Rectangular	Number of half wave patterns across the wider (a) dimension of the waveguide	Number of half wave patterns across the shorter (b) dimension of the waveguide
Circular	Number of full wave patterns existing around the circumference of the waveguide	Number of half wave patterns existing across the diameter of the waveguide

Table 4.1. Identification of mode subscripts.

4.3. The rectangular waveguide

A rectangular waveguide is basically a metallic hollow tube that has a rectangular cross section (as shown in Figure 4.3). The walls of the waveguide, which are made of highly conductive metal, such as copper or brass, confine the electromagnetic field and guide the electromagnetic wave. Transverse Electric and Transverse Magnetic modes can propagate. An allocation of the TE and TM modes in the microwave frequency spectrum can be seen in Figure 4.5.

4.3.1. TE modes in the rectangular waveguide

The $TE_{m,n}$ modes in the rectangular waveguides have the electric field component in the direction of propagation equal to zero, i.e. $E_z=0$, but with a finite magnetic field component, H_z. Using Maxwell's equations, it is possible to derive the $TE_{m,n}$ field equations [28]. The final form of the field equations for each electric and magnetic field component is given below [29],

$$E_x = E_{0x}\cos\left(\frac{m\pi x}{a}\right)\sin\left(\frac{n\pi y}{b}\right)e^{-j\beta z} \qquad 4.1$$

$$E_y = E_{0y}\sin\left(\frac{m\pi x}{a}\right)\cos\left(\frac{n\pi y}{b}\right)e^{-j\beta z} \qquad 4.2$$

$$E_z = 0 \qquad 4.3$$

$$H_x = H_{0x}\sin\left(\frac{m\pi x}{a}\right)\cos\left(\frac{n\pi y}{b}\right)e^{-j\beta z} \qquad 4.4$$

$$H_y = H_{0y}\cos\left(\frac{m\pi x}{a}\right)\sin\left(\frac{n\pi y}{b}\right)e^{-j\beta z} \qquad 4.5$$

$$H_z = H_{0z}\cos\left(\frac{m\pi x}{a}\right)\cos\left(\frac{n\pi y}{b}\right)e^{-j\beta z} \qquad 4.6$$

where β_g is the guide wavenumber, m, n=0,1,2,... and the guide's dimensions are given by a and b. Note that in these expressions and to the following ones, a time dependence of the form $e^{j\omega t}$ has been assumed, where ω is the angular frequency of the wave.

The cut off frequency of the waveguide is given by,

$$f_c = \frac{1}{2\sqrt{\mu\varepsilon}}\sqrt{\left(\frac{m}{a}\right)^2 + \left(\frac{n}{b}\right)^2} \qquad 4.7$$

where $\mu = \mu_r\mu_0$, with μ_r the relative permeability of the medium and the permeability of free space μ_0=4πx10^{-7} H/m, and $\varepsilon = \varepsilon_r\varepsilon_0$, with ε_r the relative permitivity of the medium and the permitivity of free space ε_0=8.854x10^{-12} F/m.

The mode with the lowest cut off frequency in any rectangular waveguide is called the dominant mode. For a>b, the dominant mode is the TE_{10} mode.

In chapter 2 it was shown that the relationship between the wavenumber β and the angular frequency ω is given by the dispersion relationship (see equation 2.2) which in terms of guide wavelength λ_g and frequency fcan be written as,

$$\lambda_g = \frac{\lambda}{\sqrt{1 - \left(\frac{f_c}{f}\right)^2}} \qquad 4.8$$

where $\lambda = \frac{c}{f}$ is the free space wavelength.

4.3.2. TM modes in the rectangular waveguide

The $TM_{m,n}$ modes in rectangular waveguides have zero magnetic field component in the direction of propagation, i.e. H_z=0, but a finite E_z. Using Maxwell's equations again, it is possible to derive the $TM_{m,n}$ field equations. The final form of the field equations for each electric and magnetic field component is given below,

$$E_x = E_{0x} \cos\left(\frac{m\pi x}{a}\right)\sin\left(\frac{n\pi y}{b}\right)e^{-j\beta z} \qquad 4.9$$

$$E_y = E_{0y} \sin\left(\frac{m\pi x}{a}\right)\cos\left(\frac{n\pi y}{b}\right)e^{-j\beta z} \qquad 4.10$$

$$E_z = E_{0z} \sin\left(\frac{m\pi x}{a}\right)\sin\left(\frac{n\pi y}{b}\right)e^{-j\beta z} \qquad 4.11$$

$$H_x = H_{0x} \sin\left(\frac{m\pi x}{a}\right)\cos\left(\frac{n\pi y}{b}\right)e^{-j\beta z} \qquad 4.12$$

$$H_y = H_{0y} \cos\left(\frac{m\pi x}{a}\right)\sin\left(\frac{n\pi y}{b}\right)e^{-j\beta z} \qquad 4.13$$

$$H_z = 0 \qquad 4.14$$

where m, n=0,1,2,... and the guide's dimensions are given by a and b.

The cut off frequency for TM modes is exactly the same as for TE modes i.e. is given by Equation 4.7. Similarly, Equation 4.8 gives the waveguide wavelength in terms of frequency.

4.4. The circular waveguide

The circular waveguide is a hollow tube or pipe. The geometry is shown in Figure 4.4. The modes that can propagate are again TE and TM modes. Figure 4.6 shows an allocation of these modes in the microwave frequency spectrum.

4.4.1. TE modes in the circular waveguide

$TE_{n,m}$ modes in a circular waveguide have a purely transverse electric field. As in the case of the rectangular waveguide, it is possible to solve Maxwell's equations and derive the $TE_{m,n}$ field equations. The solution using cylindrical coordinates however now requires the use of Bessel Functions, $J_m(x)$. The field equations for the $TE_{m,n}$ mode, in their final form, are given below,

$$E_r = E_{0r} J_m\left(\frac{X'_{mn} r}{a}\right) \sin(m\phi) e^{-j\beta z} \tag{4.15}$$

$$E_\phi = E_{0\phi} J'_m\left(\frac{X'_{mn} r}{a}\right) \cos(m\phi) e^{-j\beta z} \tag{4.16}$$

$$E_z = 0 \tag{4.17}$$

$$H_r = -\frac{E_{0\phi}}{Z_g} J_m\left(\frac{X'_{mn} r}{a}\right) \cos(m\phi) e^{-j\beta z} \tag{4.18}$$

$$H_\phi = \frac{E_{0r}}{Z_g} J_m\left(\frac{X'_{mn} r}{a}\right) \sin(m\phi) e^{-j\beta z} \tag{4.19}$$

$$H_z = H_{0z} J_m\left(\frac{X'_{mn} r}{a}\right) \cos(m\phi) e^{-j\beta z} \tag{4.20}$$

where m=1,2,3,... and n=0,1,2,3,...

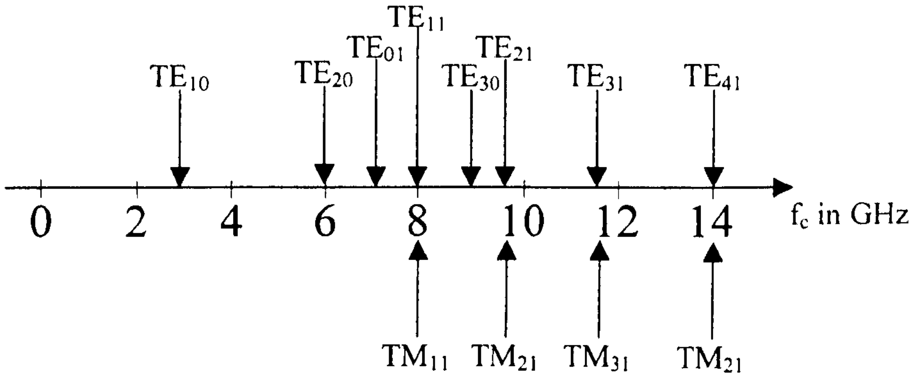

Figure 4.5. Cut off frequencies of rectangular waveguide with a=2.5b.

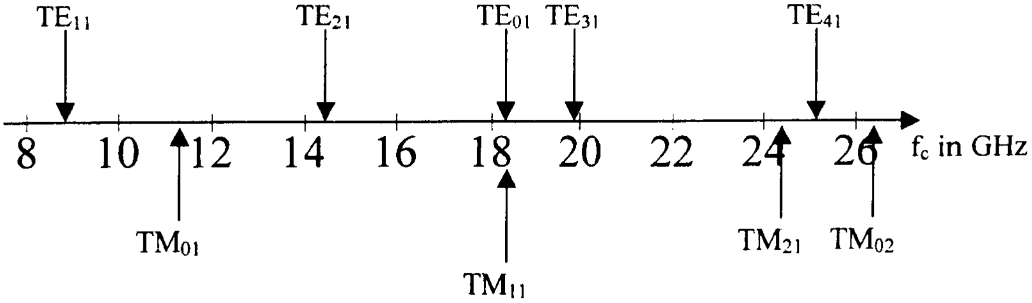

Figure 4.6. Cut off frequencies of circular waveguide with r=10 mm.

Note that X'_{mn} are the solutions of the equation $J_m(x)=0$ which are given in tables. Values for the first few roots are reproduced in the following list,

m n	0	1	2	3	4	5
1	3.832	1.841	3.054	4.201	5.317	6.416
2	7.016	5.331	6.706	8.015	9.282	10.520
3	10.173	8.536	9.969	11.346	12.682	13.987
4	13.324	11.706	13.170			

Table 4.2. Roots of $J_m(x)$ for the $TE_{m,n}$ modes.

The cut off frequency for the $TE_{m,n}$ mode of an empty guide is given by,

$$f_c = \frac{X'_{mn} c}{2\pi a} \qquad 4.21$$

The dominant mode in a circular guide is the TE_{11} mode.

The wavelength of the wave in the waveguide is given by an identical expression to that for a rectangular guide, that is,

$$\lambda_g = \frac{\lambda}{\sqrt{1 - \left(\frac{f_c}{f}\right)^2}} \qquad 4.22$$

where λ is the free space wavelength.

4.4.2. TM modes in the circular waveguide

Using the fact that the magnetic field is purely transverse allows Maxwell's equations to be solved to give the $TM_{m,n}$ field equations. The final form of the field components is given below,

$$E_r = E_{0r} J'_m\left(\frac{X_{mn} r}{a}\right)\cos(m\phi)e^{-j\beta z} \tag{4.23}$$

$$E_\phi = E_{0\phi} J'_m\left(\frac{X'_{mn} r}{a}\right)\cos(m\phi)e^{-j\beta z} \tag{4.24}$$

$$E_z = E_{0z} J_m\left(\frac{X_{mn} r}{a}\right)\cos(m\phi)e^{-j\beta z} \tag{4.25}$$

$$H_r = \frac{E_{0\phi}}{Z_g} J_m\left(\frac{X_{mn} r}{a}\right)\sin(m\phi)e^{-j\beta z} \tag{4.26}$$

$$H_\phi = \frac{E_{0r}}{Z_g} J'_m\left(\frac{X_{mn} r}{a}\right)\cos(m\phi)e^{-j\beta z} \tag{4.27}$$

$$H_z = 0 \tag{4.28}$$

where m and n are integers and X_{mn} are now the solutions of the equation $J'_m(x) = 0$ where $J'_m = \frac{dJ}{dx}$. Values for the first few roots of this equation are given in Table 4.3 below.

The cut off frequencies of the TM modes are then given by a similar expression to that for the TE mode, that is

$$f_c = \frac{X_{mn} c}{2\pi a} \tag{4.29}$$

and the wavelength of the wave in the waveguide is again given by,

$$\lambda_g = \frac{\lambda}{\sqrt{1 - \left(\frac{f_c}{f}\right)^2}} \tag{4.30}$$

n \ m	0	1	2	3	4	5
1	2.405	3.832	5.136	6.380	7.588	8.771
2	5.520	7.106	8.417	9.761	11.065	12.339
3	8.645	10.173	11.620	13.015	14.372	
4	11.792	13.324	14.796			

Table 4.3. Roots of $J'_m(x)$ for the $TM_{m,n}$ modes.

Chapter 5

The CONCERTO Software for Electromagnetic Design

5.1. Introduction

"CONCERTO" produced by VectorFields [30] is a user-friendly electromagnetic simulator based on the Finite Difference Time Domain (FDTD) method [31]. It has the ability to simulate a large range of user defined models and media interfaces. The software can be applied to a variety of microwave problems [32], for example to accurately estimate the S-parameters (Appendix A) of a cavity and the dispersion relations of an empty or loaded waveguide.

CONCERTO consists of two main functional blocks,

1. The CONCERTO Editor which allows the graphical definition of 3D structures, mesh generation and the specification of various simulation parameters, such as frequency range, operational frequency, appropriate mode selection and selection of excitation waveform. All these can be easily adjusted using well-defined dialogue boxes.

2. The CONCERTO Simulator which performs the FDTD calculations, checks the state of the model and displays all the computed fields and results in 2D and 3D views.

5.2. Modelling errors

As with all numerical methods, the FDTD method has its limits of accuracy for given computer resources. In this software, there are two basic sources of errors:

1. *Error due to finite discretisation of space (finite cell size):* The subdivision of the device into cells, called meshing in the editor environment, is performed in the CONCERTO Editor automatically. However, the user has the power to control it as desired. The basic cell size determines the accuracy of the simulation and at the same time the computer time and memory requirements. The best way to analyse circuit errors is to use different cell size and compare the results. In CONCERTO, reducing the cell size by half normally brings the space discretisation errors down by a factor of the order between 2 and 4. At the same time however, the computer calculation time will rise almost 16 times and the memory request will be increased by a factor of 8. Consequently there is always a trade off between accuracy and computing time.
2. *Error due to finite computing time used for wave simulation:* This error results from the simulation when the calculation of the Fourier Transform of the input and output signals is restricted to a very limited number of iterations. This means that the energy injected into the device has not completely been dissipated in the input and output terminations and the internal losses of the system. Generally speaking, there are two main criteria for bringing a simulation to an end,

- Firstly, during the simulation, the field distribution has to be watched in order to find out when the field amplitudes have been reduced to negligible values
- Secondly, the S-parameter curve shapes will not vary significantly.

5.3. The CONCERTO graphical editor

The CONCERTO Editor in the software plays the double role of the graphical editor that will allow the user to define graphically the problem and the mesh generator, which automatically performs the meshing process. Figure 5.1 shows the CONCERTO Editor environment.

In the editor the user has the power to build the structure using the tools provided. The most common and easily made components are cylindrical and rectangular shapes. To make these structures, the user has to set the height and give the length of each side or the radius of the circle. However, in cases of more complicated structures, like tapers or coaxial models, an object generator is available. The object generator is an interpreter for source programs prepared by the user in a specifically developed User Defined Object (UDO) language. The UDO language is simple and yet gives the user the possibility to create his own arbitrarily complicated parametric objects.

After the construction of the model, the user has to enter input and output ports. The ports can be defined as Source or Load. Declaring the port as Source means that it will serve as the input port matched at the frequency specified by the user. Setting the port as Load means that at the specified frequency, the port will act as a matched load. Figure 5.2 shows the dialogue box of the port settings. In this dialogue box, the user can select the required mode. CONCERTO provides by default the most common modes in circular and rectangular waveguides and also has a user defined mode called "Arbitrary". The "Arbitrary" mode can be used in the cases where the waveguide is loaded with dielectric and the user has to provide extra information to perform the simulation. By selecting the required mode and having set the matching frequency, CONCERTO will automatically set the effective permitivity. However, in the "Arbitrary" case, the user has to calculate the effective permitivity manually. In order to do so, the dispersion relation of the loaded cavity has to be known and the wavenumber at the required frequency has to be calculated. Having this information, the effective permitivity can be found using the following equation,

$$\beta = \frac{2\pi f \sqrt{\varepsilon_{eff}}}{c} \qquad 5.1$$

where β is the wavenumber in mm^{-1}, f is the matching frequency in GHz and c is the speed of light in mm/sec.

The last thing that remains to be defined by the user is the waveform excitation. The user has a choice of several waveforms and the selection depends on the problem that needs to be solved. For typical S-parameter calculations the limited spectrum $f<f_2$ or $f_1<f<f_2$ close to the limits of the frequency band of interest in the applications is recommended. However, if the user is interested in observing the way the wave propagates and how it behaves inside the cavity, then the sinusoidal waveform can be chosen.

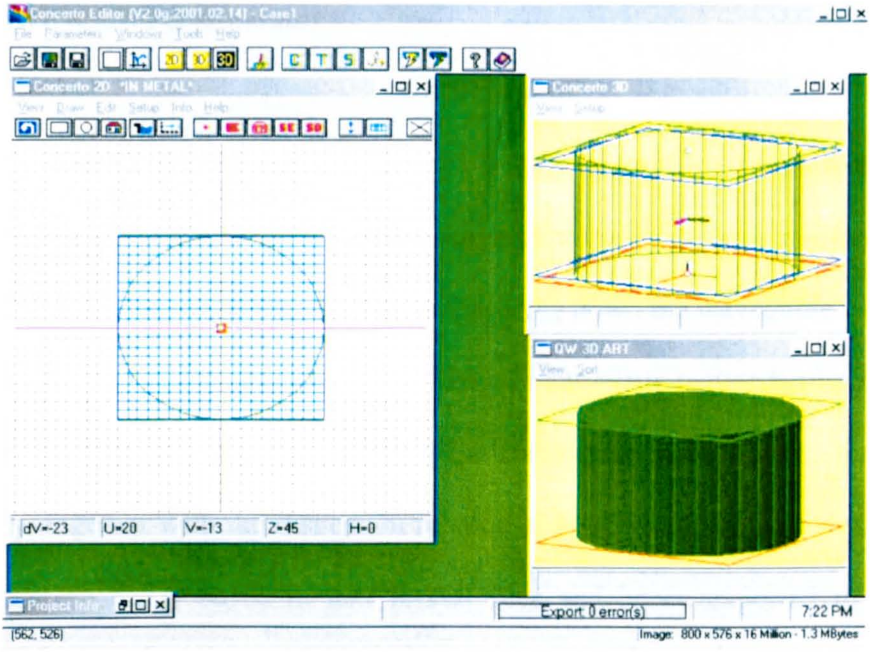

Figure 5.1. The CONCERTO editor environment.

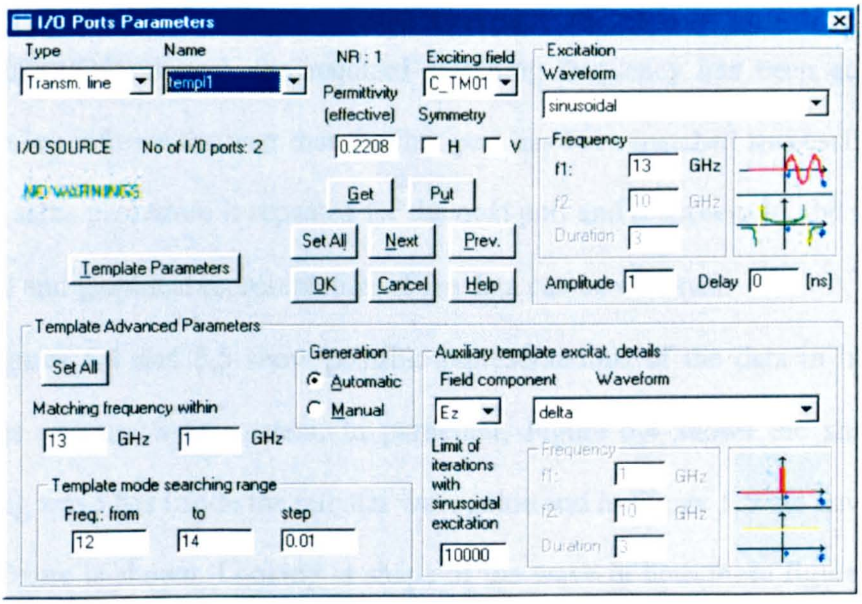

Type: Transm. line
Name: templ1
NR : 1
Exciting field: C_TM01
Permittivity (effective): 0.2208
Symmetry: ☐ H ☐ V
I/O SOURCE
No of I/O ports: 2
NO WARNINGS

Excitation
Waveform: sinusoidal
Frequency
f1: 13 GHz
f2: 10 GHz
Duration: 3
Amplitude: 1
Delay: 0 [ns]

Template Advanced Parameters
Set All
Matching frequency within: 13 GHz 1 GHz
Template mode searching range
Freq.: from 12 to 14 step 0.01
Generation: ● Automatic ○ Manual
Auxiliary template excitat. details
Field component: Ez
Waveform: delta
Limit of iterations with sinusoidal excitation: 10000
Frequency
f1: 1 GHz
f2: 10 GHz
Duration: 3

Figure 5.2. The port settings.

5.4. The CONCERTO simulator

The CONCERTO Simulator utilizes FDTD algorithms to perform the wave analysis and is capable of offering many ways of visualizing the simulated fields and calculated circuit characteristics. A wave propagating down the waveguide can be viewed in 3 dimensional graphics or in envelope shapes in any plane perpendicular to any of the coordinate axes. At the same time, all the S parameters can be easily seen numerically or graphically, together with the dispersion relation and the phase of the wave. Finally, all the data can be easily saved in text format files and hence exported to spreadsheet packages for further analysis if necessary.

As soon as the Simulator starts, a simulation log sheet appears, as shown in Figure 5.3. The first two lines describe the start of the simulation and then a line indicates that at the first Input/Output port, the required matching frequency has been achieved. The simulation log informs the user that the first port has been matched successfully at 13.04 GHz. The same procedure is repeated for the next port and if successful, the simulation is terminated and graphical representation of the data can be obtained.

Figures 5.4 and 5,5 show possible representations of the data in both 2 and 3 dimensions and the S-parameters. In particular, Figure 5.4 shows the shape that the propagating wave has inside the circular waveguide and in Figure 5.5 the envelope of the previous figure is shown. Looking at shape of the wave in both these figures, it is clear that the mode used was the TM_{01}. In Figure 5.6 the S-parameter window can combine more than one graphs at the same time. In this case, the data shown is for the $|S_{11}|$ parameter (wave reflected), $|S_{21}|$ parameter (wave transmitted) and the dispersion relation.

It can be seen that due to the matched load at the end of the guide, $|S_{11}|$ is zero, as no power is being reflected, while $|S_{21}|$ is 1 as 100% of the power is being transmitted above the cut off frequency (which is at around 11.47 GHz).

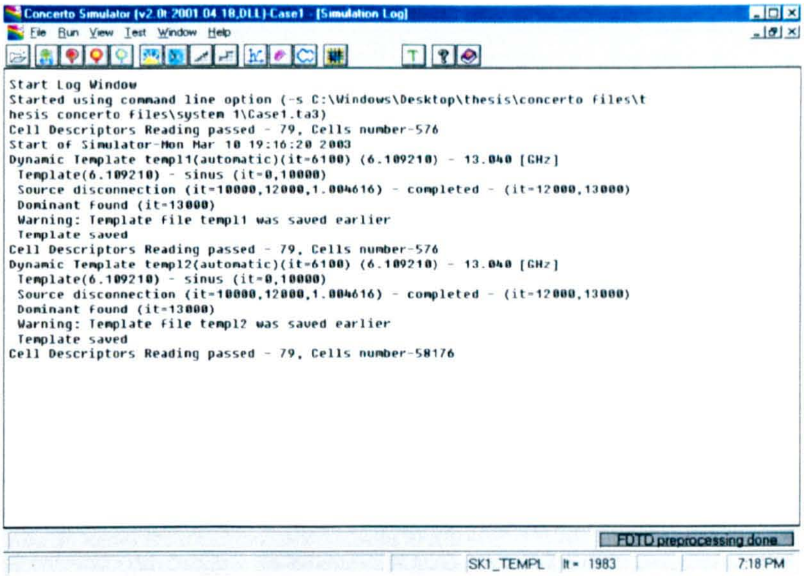

```
Start Log Window
Started using command line option (-s C:\Windows\Desktop\thesis\concerto files\t
hesis concerto files\system 1\Case1.ta3)
Cell Descriptors Reading passed - 79, Cells number-576
Start of Simulator-Mon Mar 10 19:16:20 2003
Dynamic Template templ1(automatic)(it=6100) (6.109210) - 13.040 [GHz]
 Template(6.109210) - sinus (it=0,10000)
 Source disconnection (it=10000,12000,1.004616) - completed - (it=12000,13000)
 Dominant found (it=13000)
 Warning: Template file templ1 was saved earlier
 Template saved
Cell Descriptors Reading passed - 79, Cells number-576
Dynamic Template templ2(automatic)(it=6100) (6.109210) - 13.040 [GHz]
 Template(6.109210) - sinus (it=0,10000)
 Source disconnection (it=10000,12000,1.004616) - completed - (it=12000,13000)
 Dominant found (it=13000)
 Warning: Template file templ2 was saved earlier
 Template saved
Cell Descriptors Reading passed - 79, Cells number-58176
```

FDTD preprocessing done

SK1_TEMPL It = 1983 7:18 PM

Figure 5.3. The simulation log sheet.

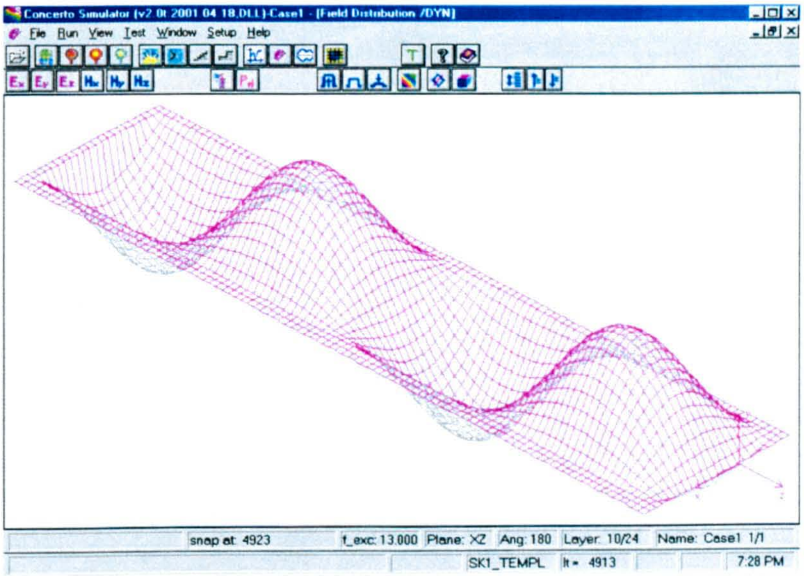

snap at 4923 f_exc: 13.000 Plane: XZ Ang: 180 Layer: 10/24 Name: Case1 1/1

SK1_TEMPL It = 4913 7:28 PM

Figure 5.4. The 3 dimensional propagation of the wave.

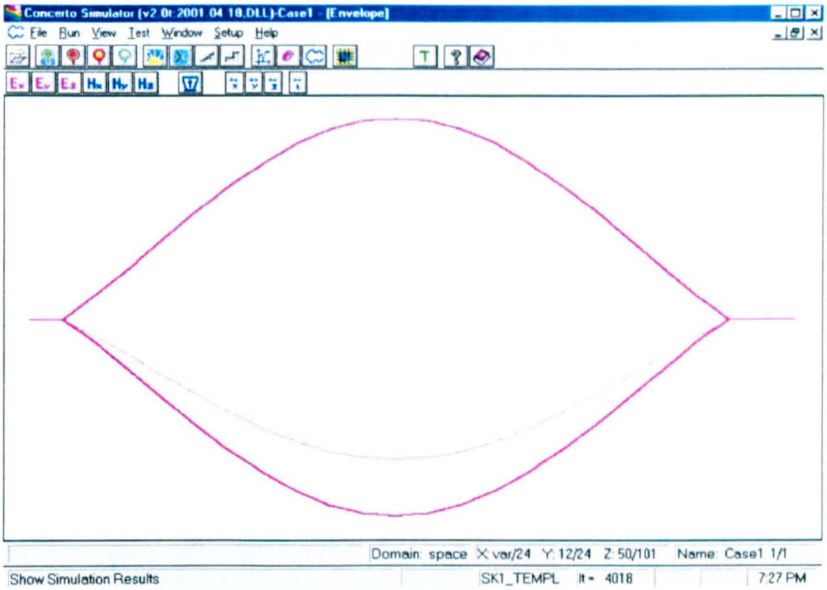

Figure 5.5. The envelope of the propagating wave.

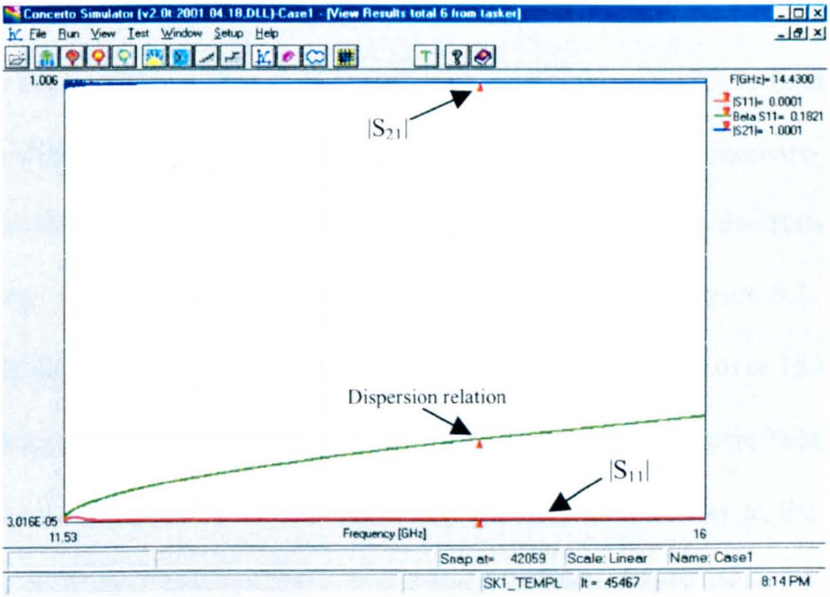

Figure 5.6. The S parameters and the dispersion relation of the system.

Chapter 6

The Electron Beam Focusing Device

6.1. Introduction

If a high-energy collimated electron beam (60kV – 70kV) is injected into field free space, then the diameter of the electron beam will rapidly increase with distance from the electron gun due to space charge repulsion between the electrons. For a cavity 600 mm long, this expansion can be very serious as shown in Figure 6.1. At 60kV, the radius of the electron beam increases from 1 mm at the entrance to over 18 mm at the exit of the loaded cylinder used in the Cerenkov device when the electron beam current is at its maximum of 250mA. Having in mind that the internal diameter of the alumina liner could be as small as 6 mm, it is clear that a beam current of only about 15 mA is all that can be transported safely through the whole length of the loaded cylinder without serious interception problems. This is far too small to provide enough electronic gain, and consequently, it is clear that for high gain and high power output, some sort of focusing device is required to assist in the transport of a higher beam current.

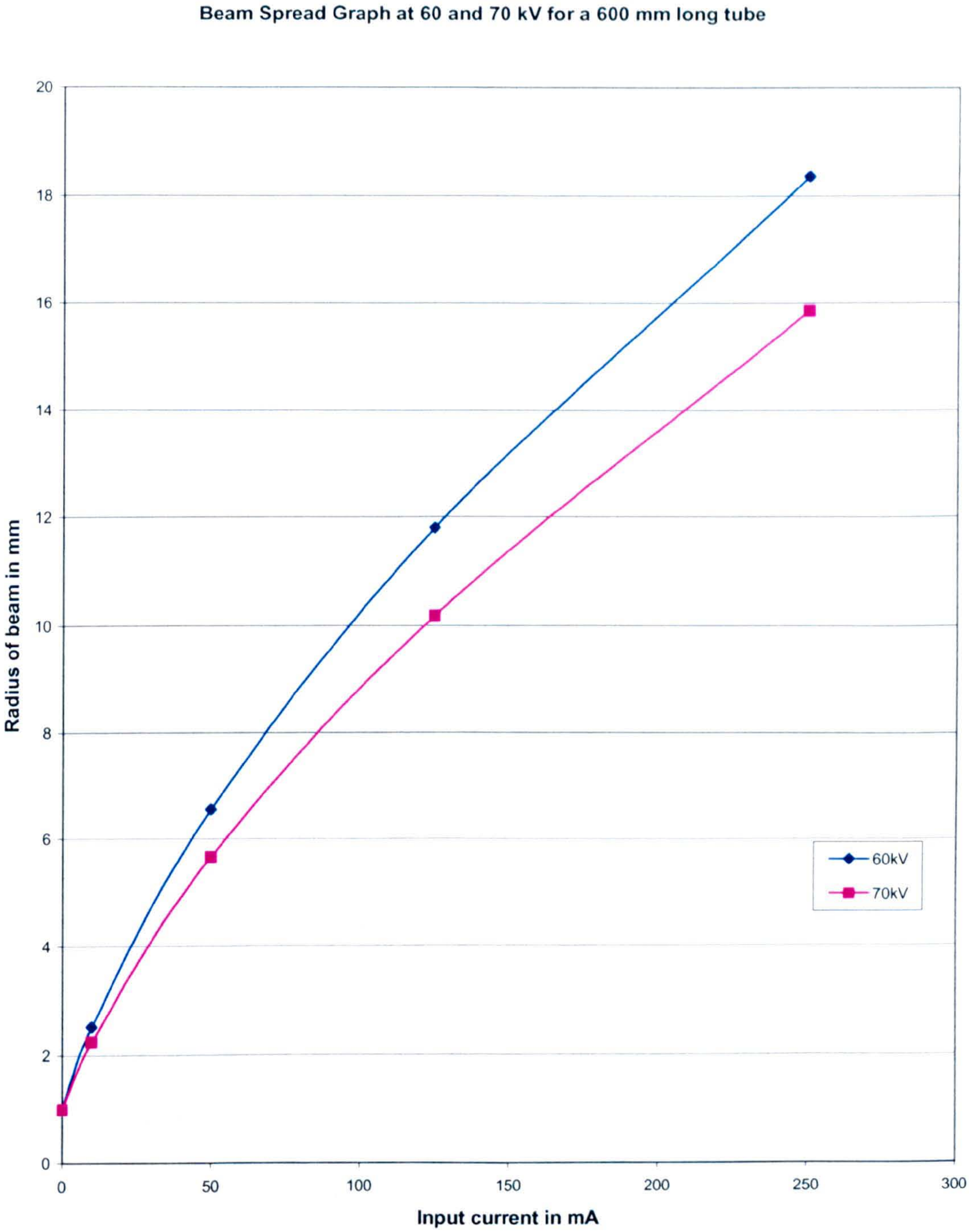

Figure 6.1. Graph that illustrates the need for a focusing device at high currents. The graph shows how the radius of an electron beam at the exit of a 600mm cavity varies with beam current. The initial beam radius was 1mm.

6.2. Focusing with a longitudinal magnetic field

A common method for confining the electron beam is to use a longitudinal magnetic field (i.e. parallel to the direction of the beam). The minimum magnetic field required is called the "Brillouin" field [33] and is given by,

$$B_{min} = 8.32 \cdot 10^{-4} \frac{I_0^{1/2}}{r_0 V_0^{1/4}} \qquad 6.1$$

where I_0 is the input electron beam current, V_0 is the accelerating voltage and r_0 is the minimum beam radius.

For an input current of 120 mA, an accelerating voltage of 70 kV and a beam radius of 1 mm, the minimum magnetic field required is B_{min}= 177 Gauss. Gittins [34], in his analysis of Brillouin flow, suggests that the actual magnetic field required is 2 to 3 times this minimum amount.

6.3. Ways to control the electron beam

In order to design a suitable system that will adequately control the electron beam flow, two different options were considered. The first was to use permanent magnets in the shape of rings, placed at specific points along the length of the tube, which would periodically focus the electron beam [35]. The second option was to make a solenoid that would cover the whole length of the tube and hence provide a uniform axial magnetic field along the cavity. It was decided to consider the permanent magnet structure first, as this seemed to provide a simpler solution especially since the whole focussing system had to operate when raised to a 70kV potential.

6.3.1. Permanent ring magnets

The principle of periodic magnetic focusing can be summarized by considering Figure 6.2. The magnets can be seen to act lenses, periodically re-focussing the beam, which is expanding under space charge forces.

The Universal Beam Spread (UBS) curve can be used to calculate the points where the permanent magnets should be placed. The UBS curve relates the change of radius of the electron beam to the distance along the length of the cavity. For our Cerenkov FEL design, the UBS curve can be seen in Figure 6.3. This curve is for a total cavity length of 600mm, an input electron beam current of around 120mA and an accelerating voltage of 70kV. Since the radius of the dielectric tube of the second design was 3 mm, the electron beam can only be allowed to expand up to around 2 mm in radius. Therefore ring permanent magnets have to be placed at 150 mm and 450 mm along the cavity to enable electron beam transmission to be achieved.

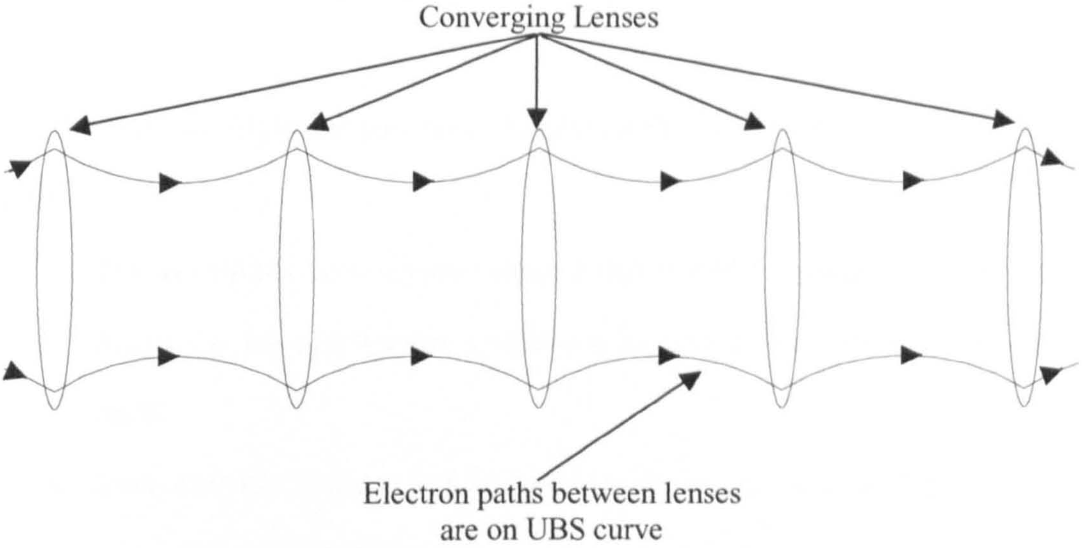

Figure 6.2. The principal of magnetic periodic focusing.

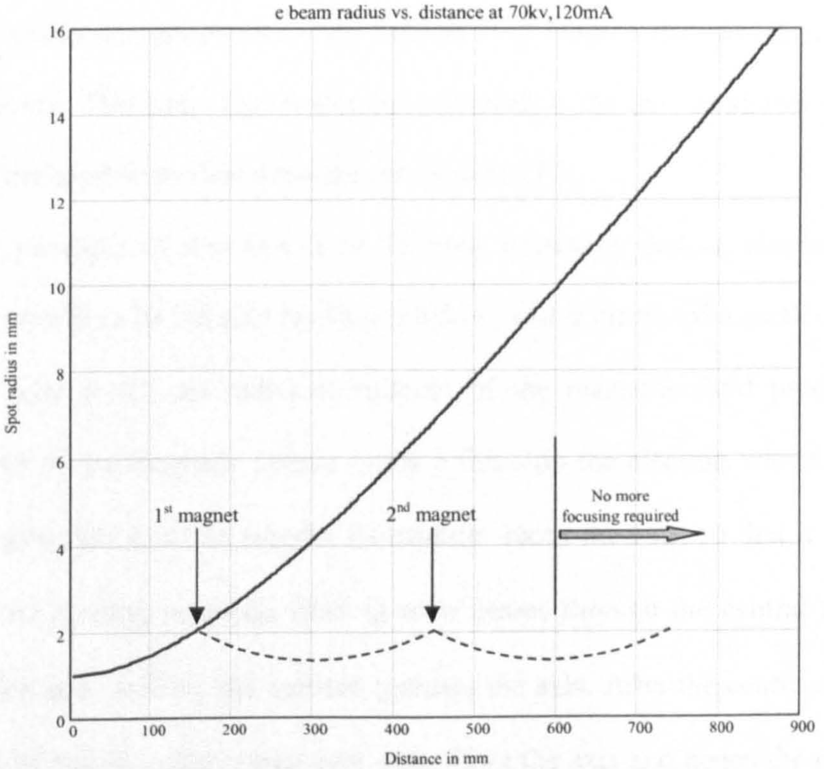

Figure 6.3. The universal beam spread curve and the possible positions of the ring magnets along the length of the cavity.

6.3.1.1. Design of the focusing permanent magnet device

The two most important factors controlling the design of each focusing magnet device were:

a) The availability of a suitable magnet that would fit around the first Cerenkov design, i.e. the ring magnet would need to have an inner diameter of 22 mm or more.

b) Stuart [36] has calculated that in order to provide the correct focusing effect for magnetic lenses spaced 150 mm apart, an on axis field of approximately 400 Gauss would be required.

Figure 6.4 shows the geometry of the NdFeB ring magnet that was available for the focusing device. This ring magnet was incorporated in the lens as shown in Figure 6.5 which is reproduced from Gewartowski and Watson [37].

The principle of this lens is as follows. Assuming that an electron enters the focusing device from its left side (as shown below) and is displaced a small distance from the central axis A-A', the radial component of the magnetic field produced by the fringing field of the magnetic circuit exerts a force on the electron which is out of the page. This gives the electron angular momentum about the axis, so that it crosses the z component of fringing magnetic field $\underline{B}$ as it passes through the central region of the device, which now deflects the electron towards the axis. After the centre of the device, the lines of $\underline{B}$ have a radial component away from the axis and hence the electron loses its angular velocity. The electron therefore leaves the focusing device with a radial component of velocity, which is directed towards the axis and no angular velocity.

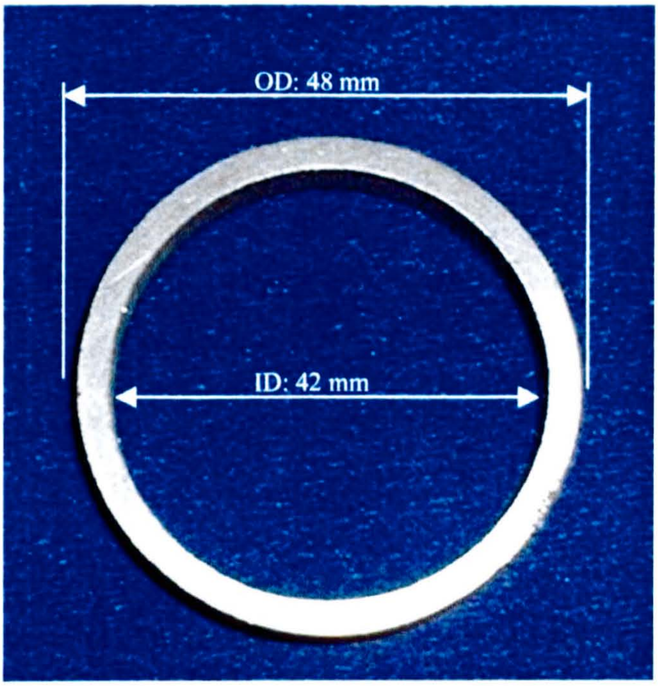

Figure 6.4. Geometry of the ring magnet.

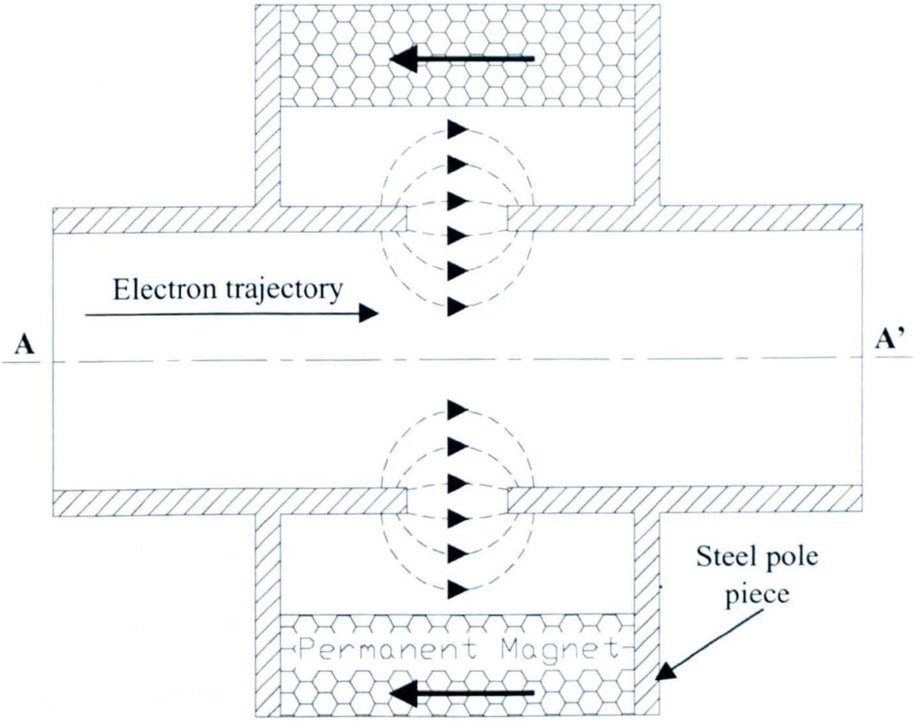

Figure 6.5. The ring magnet focusing design.

To produce a detailed design for a magnetic lens, the PE2D simulation package [38,39] was used. PE2D is able to solve 2D problems in magnetostatic, electrostatic and electromagnetic situations, using the finite element method. The PE2D editor allows the user to draw in 2 dimensions the model to be simulated and then perform a numerical analysis. Because of the large amount of data required for finite element analysis and the limited number of mesh points, the role of symmetry is very important in simplifying the design. Figure 6.6 illustrates the use of symmetry to simplify the simulation process in this case.

The point A on the PE2D model is the point of interest, i.e. where the magnetic field must have a value of about 400 gauss in order to provide the required focussing action. Using PE2D, values of the magnetic field at point A, for various Gap sizes were tabulated (Table 6.1) assuming NdFeB permanent magnet material having remanent magnetisation Br=10000 gauss (1 tesla).

Gap size (mm)	B_A (gauss)
0	2.92241
2	1754.79
4	2296.97
6	2537.54
8	2633.26
10	2643.67

Table 6.1. Variation of the magnetic field at point A depending on the gap size.

From Table 6.1, it is clear that the variation of the focussing field with gap size is very rapid in the vicinity of the required 400gauss, which would make mechanical construction of an accurate focussing device difficult. The problem was that the NdFeB magnet was too strong. A possible remedy was to prevent a large amount of flux going through the gap by using a shunt.

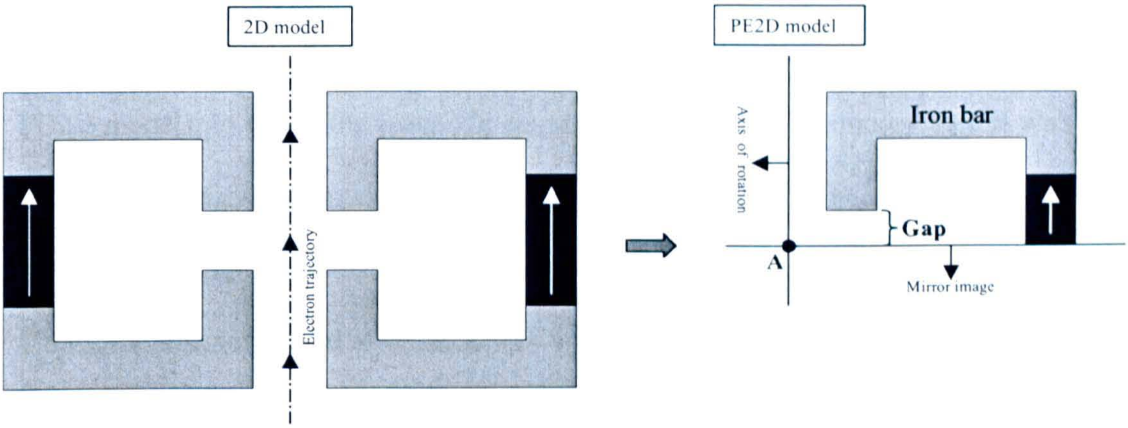

Figure 6.6. Initial simulation model for the magnet focusing device.

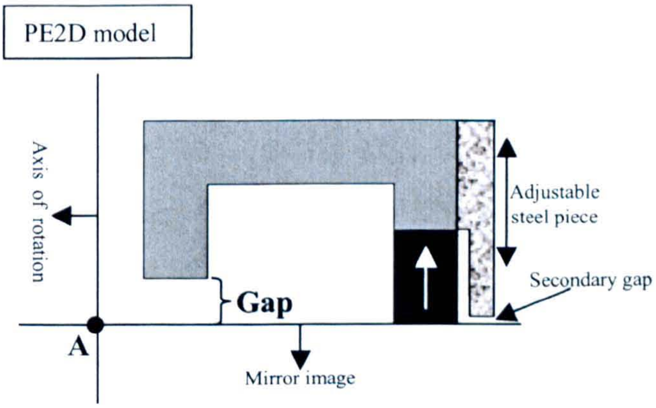

Figure 6.7. Revised simulation model for the magnet focusing device.

Figure 6.8. Picture of the magnet focusing device.

A thin ring of steel was placed around the magnet as shown in Figure 6.7 (for the PE2D model), to act as the magnetic shunt. By altering the secondary gap, it was hoped to be able to adjust the on axis field strength with more sensitivity.

Simulations showed that when the secondary gap was 2 mm and a primary gap of 4 mm, the magnetic field at point A was 440gauss. This value of the magnetic field was considered as acceptably close to the required 400gauss and hence 3 focusing devices were manufactured. A picture of a finished device can be seen in Figure 6.8.

6.3.1.2. Testing of the focusing permanent magnet device

An experimental hollow copper tube of 22 mm outer diameter and 500 mm long was made to investigate the focusing ability of these devices. One end of this tube was sealed with a small glass dome, previously coated with phosphorescent powder on the inside to allow the quality of the electron beam passing along the axis of the tube to be observed. Figure 6.9 shows this test device and the focusing device in position.

By placing the magnet at different heights along the copper tube, it was possible to change the beam focusing and hence the appearance of the spot on the phosphorescent screen. For low electron beam currents, up to 50 mA, the focusing of the beam was satisfactory (see Figure 6.10). However, when the input current was raised to 65 mA, the quality of the electron beam was seriously affected.

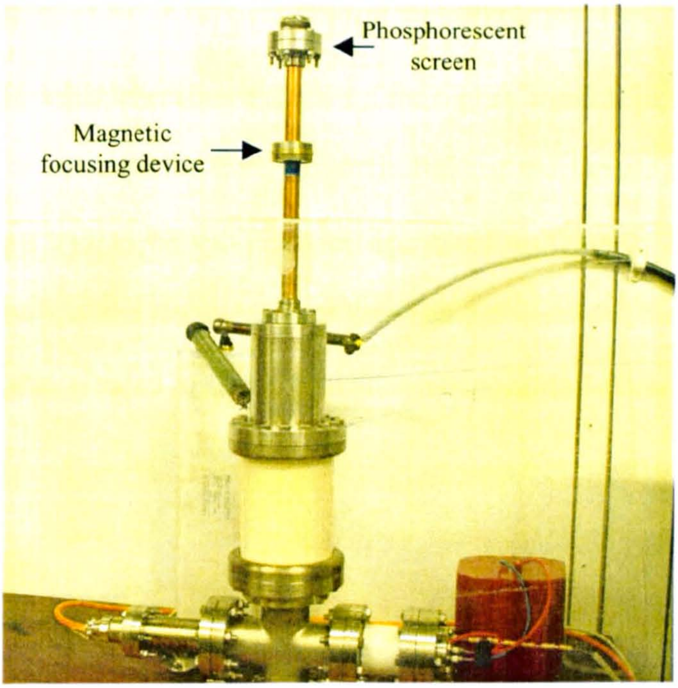

st. steel chamber (welded)

Figure 6.9. Testing the permanent magnet focusing device.

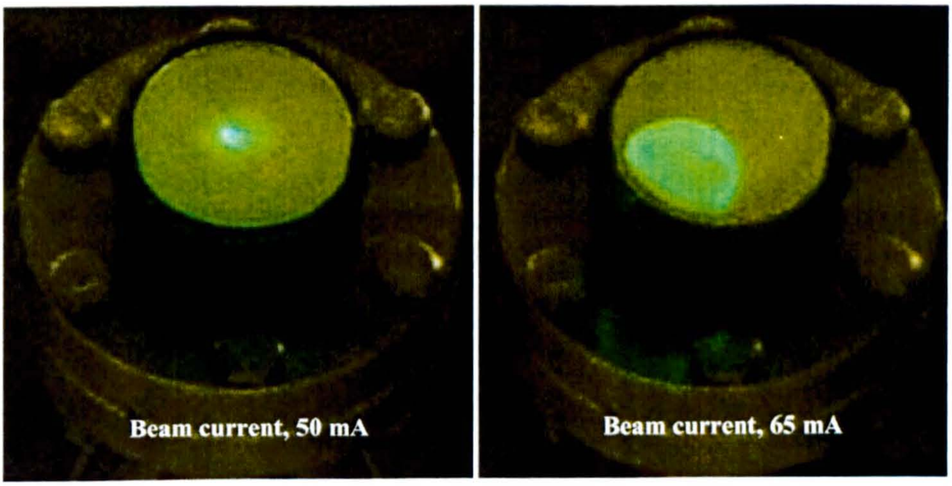

Figure 6.10. The effect that the increase of the input beam current has on the electron beam spot size. The screen was approximately 50mm in diameter.

In order to achieve adequate focusing for higher currents, it was important to be able to increase or decrease the axial magnetic field of the focusing device. To do this, the secondary gap had to be increased or decreased accurately. This proved to be a difficult task because of the attractive force between the shunt and the permanent magnet. Consequently, it was decided to seek for an alternative method of controlling the electron beam.

6.3.2. The electromagnet

An electromagnet in the form of a solenoid has the advantage of creating a constant magnetic field along the majority of the length of the cavity. Another key factor in its favour is that the magnetic field can be accurately controlled by varying the current through it. In spite of these advantages, this solution was initially resisted because the solenoid required around 7000 turns to achieve the necessary on axis magnetic field of about 400 gauss and power to supply the solenoid would have to be held at 70kV.

6.3.2.1. Design of the electromagnet

Since the outer diameter of the copper waveguide for the first system was 22 mm it was decided to build the coil on a copper tube with internal diameter of nearly 24 mm so that it would fit neatly over the waveguide. The outer diameter of the tube was 25.4 mm. The length of the coil was chosen to be 540 mm.

Following the solenoid theory described in [40], it is possible to find the coil requirements in order to achieve a magnetic field at the centre of about 400 gauss. Assuming that the length of the solenoid is much greater than its radius (length=540 mm, radius=12.7 mm) then the magnetic field at the centre of the coil reduces to Equation 6.2,

$$B = \frac{\mu_0 N I}{l} \qquad 6.2$$

where μ_0 is the permeability in free space, N is the number of turns, I is the current through the solenoid, l is the total length and B is the magnetic field.

If the magnetic field strength required is 440 gauss or 0.044 tesla, then with $l = 0.54$m, I=3A and $\mu_0 = 4\pi 10^{-7}\,\mathrm{Hm^{-1}}$, the total number of turns needed was 6302 according to Equation 6.2. It was decided to use enamelled copper wire with diameter of 1.25mm, so in all, 16 layers of wire were required.

A jig and motor as shown in Figure 6.11 were employed to carry out the winding. Figure 6.12 shows the completed solenoid connected to a voltage source, in this case two 12V YUASA batteries each having a capacity of 12Ah [41]. This means of driving current through the solenoid was chosen because of the simplicity of raising the batteries up to 70kV.

The problem with a simple solenoid design like that shown in Figure 6.12 is that all the flux passing through the centre of the solenoid has to leak from one end back to the other. This leakage flux could well interfere with the satisfactory operation of the electron gun and consequently it was decided to construct a magnetic flux return path in the form of a steel cylindrical housing surrounding the coil. Although this idea does not alter the magnitude of the magnetic field within the solenoid, its effect in the external field is difficult to predict without trusting some form of software package. Again PE2D was used to simulate the design.

First of all a model of the solenoid without a steel housing was simulated. Figure 6.13 shows the results of the simulation. Again symmetry was used to simplify the process. The yellow rectangle then represents a part of the coil. The model has an identical rectangle mirrored over the R- axis and this whole shape is rotated around the Z-axis. This way a complete model of the solenoid is simulated. Note however the very large difference in the scales of these axes. On the Figure, the magnetic field lines occupy a vast region around the coil, and it was clear unwanted magnetic field would affect the performance of the electron gun. In Figure 6.14, rectangles representing the steel tube and steel flanges are in place surrounding the outer sides of the solenoid. The effect of the steel housing is clear. Now the returning field lines are confined within the steel housing region, greatly reducing the external magnetic field. There is a major concentration of field lines at the end of the solenoid however, where they pass through the steel flange. A check measurement of the amplitude of the magnetic field in the flange was performed with PE2D and a maximum value of around 1600gauss was found close to point A (Figure 6.14). Since the steel saturates magnetically at about 20000gauss, the fact that PE2D used a constant value of permeability was not a problem.

After building the solenoid and before placing the steel housing around it, it was decided to measure the magnetic field along the length of the coil experimentally. A search coil of 100 turns was built (with an internal radius of 6.4 mm and outer radius of 9.5 mm) and used for this purpose. For comparison purposes, the variation of the magnetic field inside a solenoid with axial position was calculated theoretically using Equation 6.3,

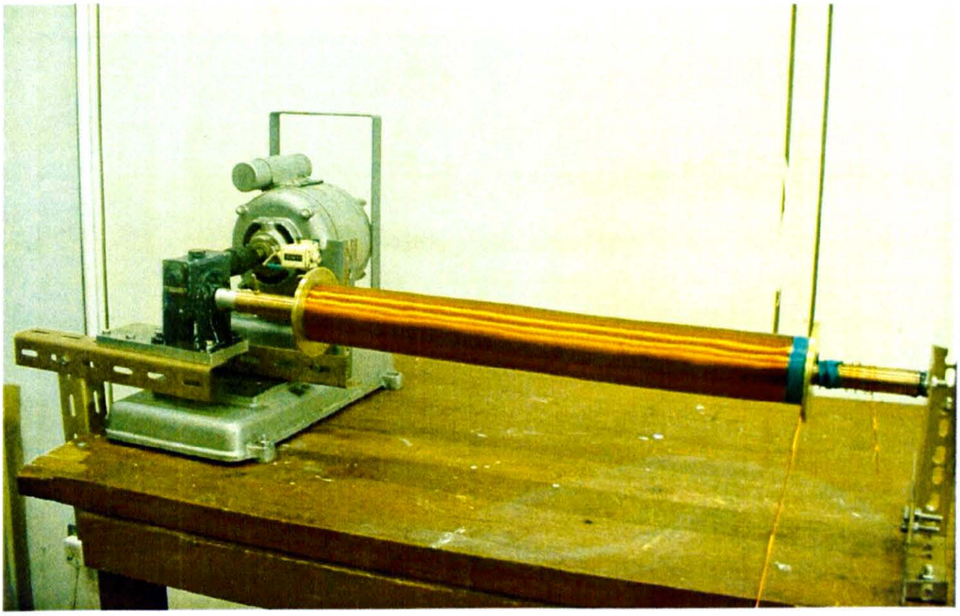

Figure 6.11. The solenoid winding set-up.

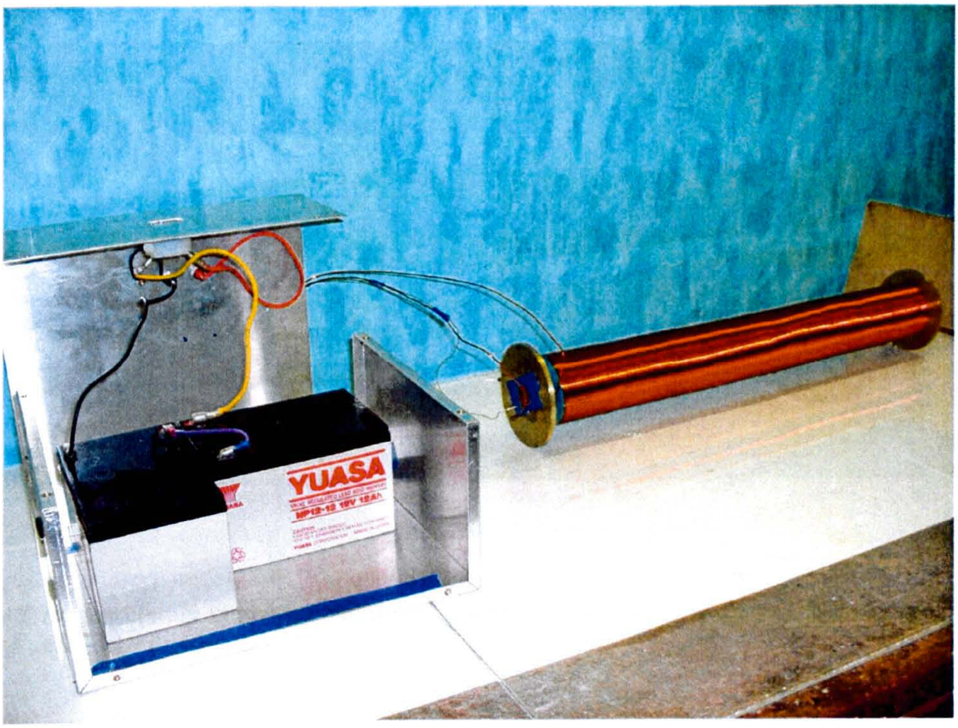

Figure 6.12. The completed solenoid and its power provider.

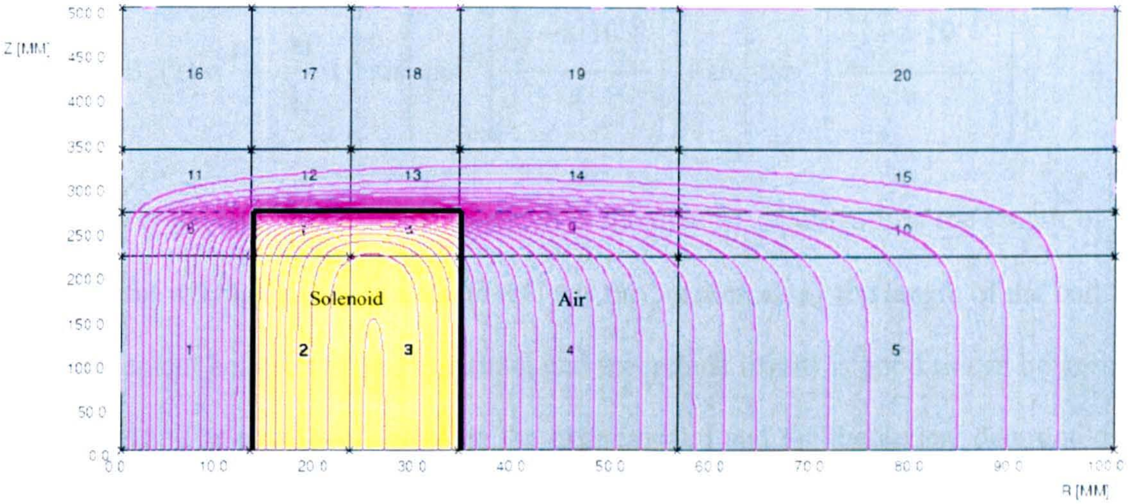

Figure 6.13. Simulation model for the solenoid without any steel housing (Note the differences in the vertical and horizontal scales).

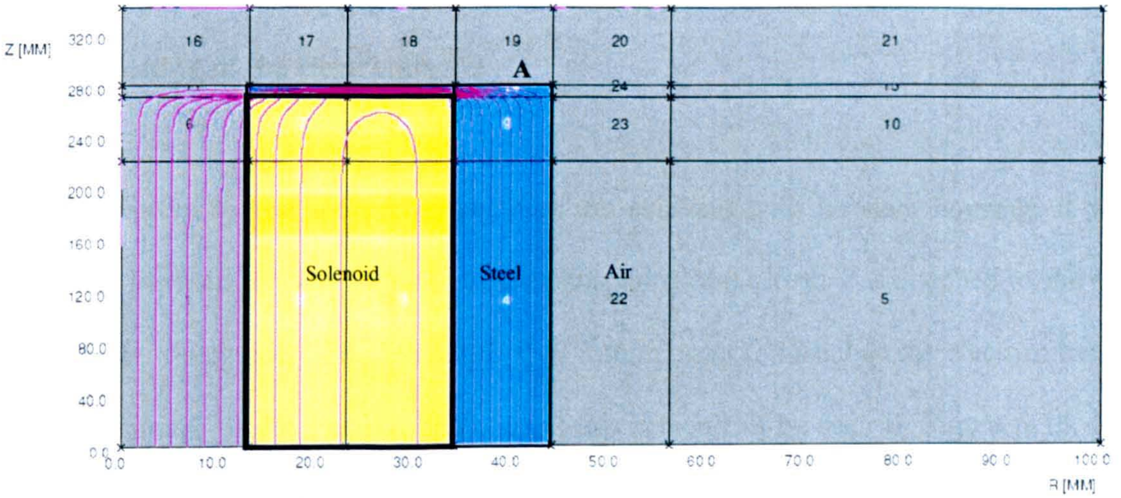

Figure 6.14. Simulation model for the solenoid with the steel housing (Note the differences in the vertical and horizontal scales).

$$B_z(z)=\frac{\mu_0}{2}\cdot\frac{N}{L}\cdot I\cdot\left(\sin\left(\tan^{-1}\left(\frac{\frac{L}{2}-z\cdot10^{-3}}{a}\right)\right)+\sin\left(\tan^{-1}\left(\frac{\frac{L}{2}+z\cdot10^{-3}}{a}\right)\right)\right) \qquad 6.3$$

where μ_0 is the free space permeability, N is the number of turns, L is the length of the coil, a is the average radius of the coil and z is the position along the length of the coil. The agreement between the experimental and theoretical results is good as can be seen in Figure 6.15. The small shift between the experimental and the theoretical data could be due to the finite length of the search coil (2cm) and the difficulty in finding the centre of the solenoid. As desired, the magnetic field along the length of the solenoid was approximately 440gauss.

6.3.2.2. Testing of the electromagnet

In order to test the performance of the solenoid with its steel housing, it was placed on the main system. Again, a small phosphorescent screen was attached to the end of a copper waveguide tube of length L=540 mm in order to visualise the electron beam. A typical image of the electron beam using this screen can be seen in Figure 6.16. For this case, the electron beam current was about 40mA and the spot diameter was very small and well defined. Its diameter was measured to be just over 0.5mm. Very satisfactorily, even when the beam current was increased up to 150mA, the spot did not change in shape and size. It was clear that a sufficiently large proportion of the electron beam could be transported down the whole length of a loaded cavity using this solenoid.

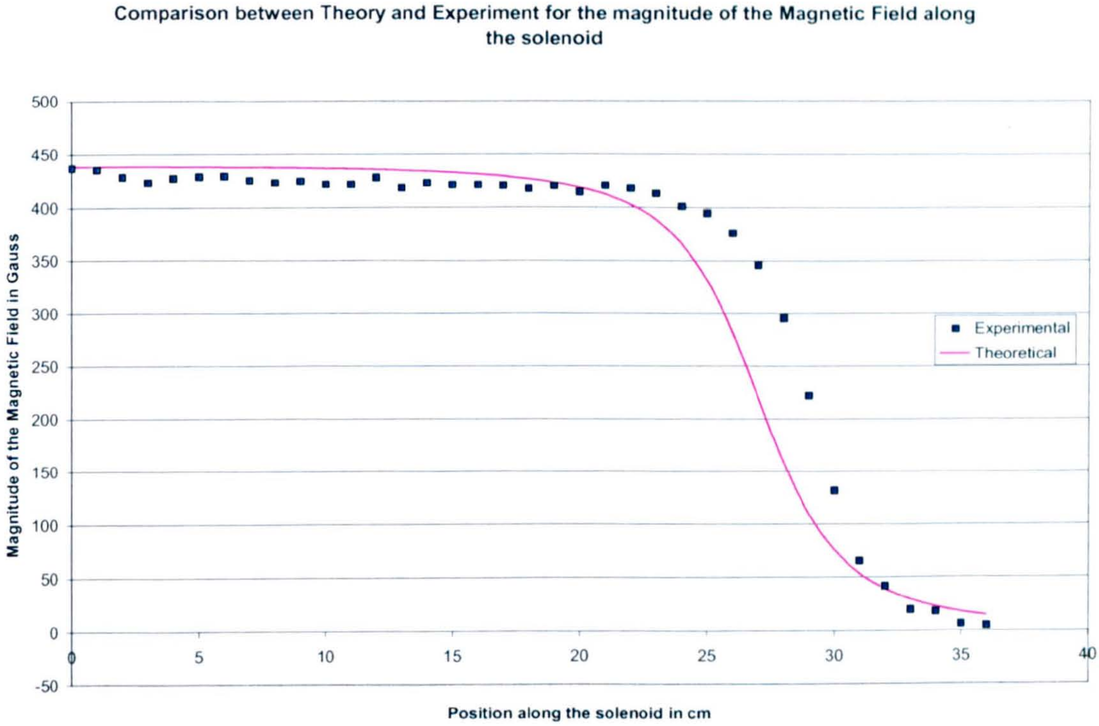

Figure 6.15. Graph showing the experimental and theoretical magnetic field amplitude.

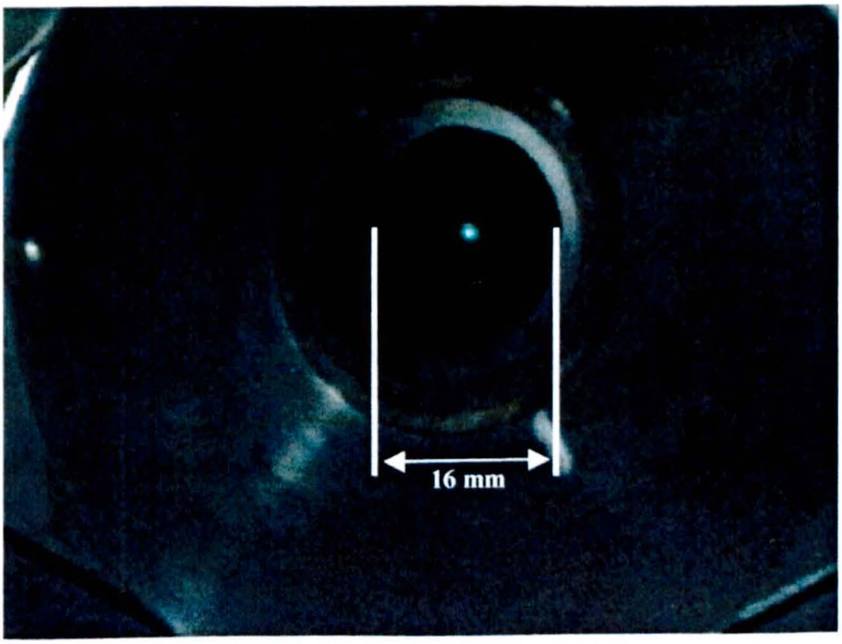

Figure 6.16. Trace of the electron beam at the End of the loaded cavity after being focused by the solenoid.

Chapter 7

Analysis and Design of the First System

7.1. Introduction

In all free electron lasers it is necessary to couple out a sample of the power circulating within the cavity when the device is oscillating. For the first Cerenkov design, it was decided to couple this power from the cylindrical cavity into a rectangular waveguide via a small hole in the side of the cylindrical guide. Standard 22 mm outer diameter copper tube was available, and hence all the calculations were done having this dimension for the cylindrical waveguide in mind. Various dielectric tube manufacturers were contacted in order to obtain a suitably sized alumina liner to partially fill this waveguide and eventually Alfa Aesar Materials [42] were chosen. Alfa was capable of supplying us with a dielectric tube with an outer diameter of 20mm, which fitted nicely into the copper circular waveguide. According to the company's catalogue, the only value for the dielectric constant quoted for their material was 9.2 at 10 MHz. The standard value of the dielectric constant of alumina at 10GHz is 9.9 [43], for the purity quoted by

Alfa. Due to the fact that it was hoped to operate the Cerenkov system at roughly 10 GHz, it was decided to use a value for the dielectric constant of 10 for simulation purposes, for simplicity.

The amount of power coupled out from the cylindrical waveguide cavity depends critically on the size of the coupling hole. If the hole is too large, the additional loss could cause the FEL to stop oscillating. On the other hand, too small a hole would mean that very little power would be coupled out, perhaps too small a power to be detectable. The size of this hole linking the main loaded cavity with the rectangular guide would be found by simulating the whole system using CONCERTO.

7.2. Theoretical design of the first system

The very first step in the design process was to actually calculate the dispersion relation of the system. MathCAD software was used to numerically analyse the first design which had the dimensions shown in Figure 7.1.

From the resulting dispersion diagram (Figure 7.2.) it can be seen that synchronism which occurs at the intersection of the electron beam line (drawn for 70kV) and the dispersion curve is at a frequency of 12.4GHz. This is then close to the expected operating frequency of the FEL. Knowing the operational frequency and the corresponding wavenumber (0.547 mm^{-1}), it was possible to start the design of the coupler using CONCERTO.

A step-by-step approach was followed so that a detailed pictured of all the parts that make up the system would be available. The design process was split into 4 parts as follows,

1. The empty circular cavity
2. The loaded circular cavity
3. The coupling hole
4. The coupler

7.2.1. The empty circular cavity

This first part of the design process investigated the way a TM_{01} mode wave propagates in an empty circular waveguide. The main reason for this was to check the output of CONCERTO for a configuration capable of an analytical solution.

For a 20 mm diameter circular waveguide, the theoretical cut off frequency is 11.47GHz for the TM_{01} mode. When driven by a source at 12.4GHz, the expected wavelength in the guide was 64mm. For simulation purposes, an empty guide 100mm long was closed at one end by a short circuit and driven by a matched source of 12GHz at the other. Figure 7.3 illustrates the standing wave pattern developed by the simulation and shows excellent agreement with the predicted wavelength. Figure 7.4 shows the transverse profile of the electric field. This also shows excellent agreement with the Bessel function variation, $J_0\left(2.405\frac{r}{a}\right)$, as expected.

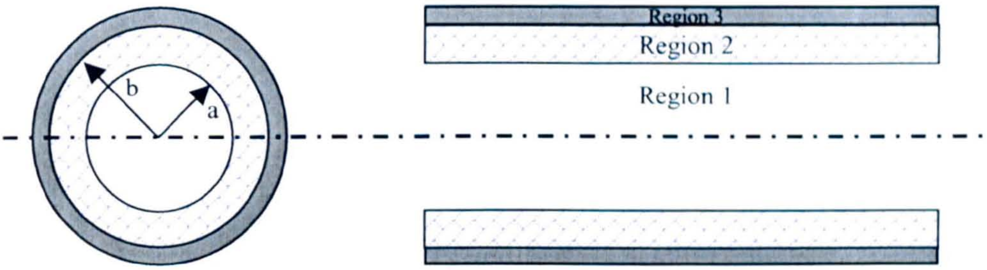

Figure 7.1. Schematic drawing of the dielectrically loaded circular waveguide. Region 1 is the vacuum, Region 2 is the alumina dielectric (with a=7.5 mm and b=10 mm) and Region 3 is the copper waveguide.

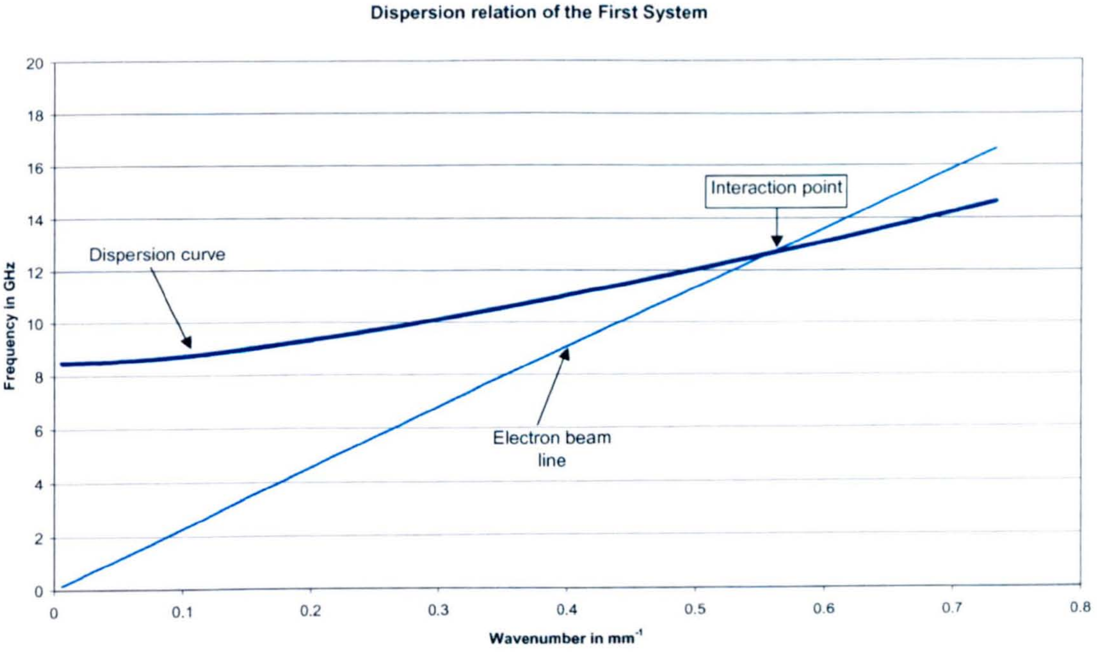

Figure 7.2. Dispersion relation for the first system for an alumina tube with id=15mm, od=20mm and er=10. The electron beam line is for an accelerating voltge of 70kV.

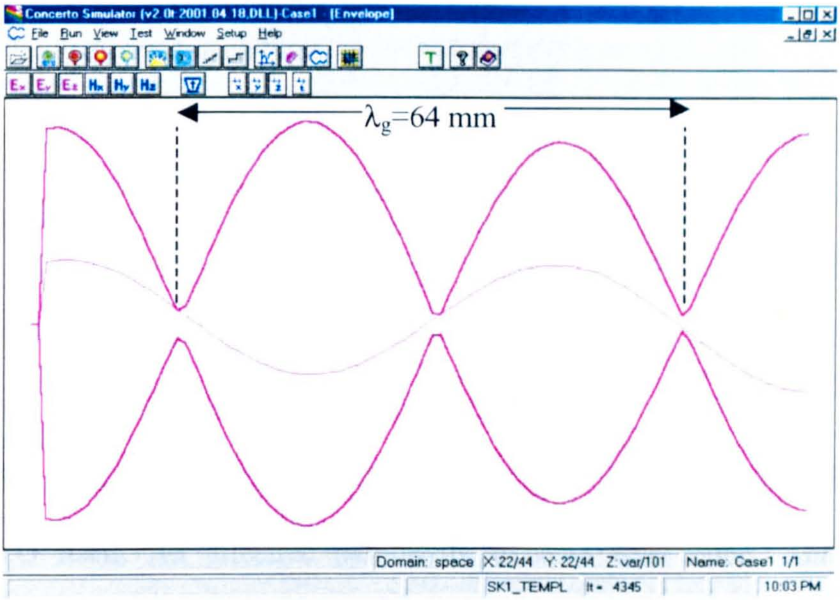

Figure 7.3. Standing wave inside an empty circular waveguide.

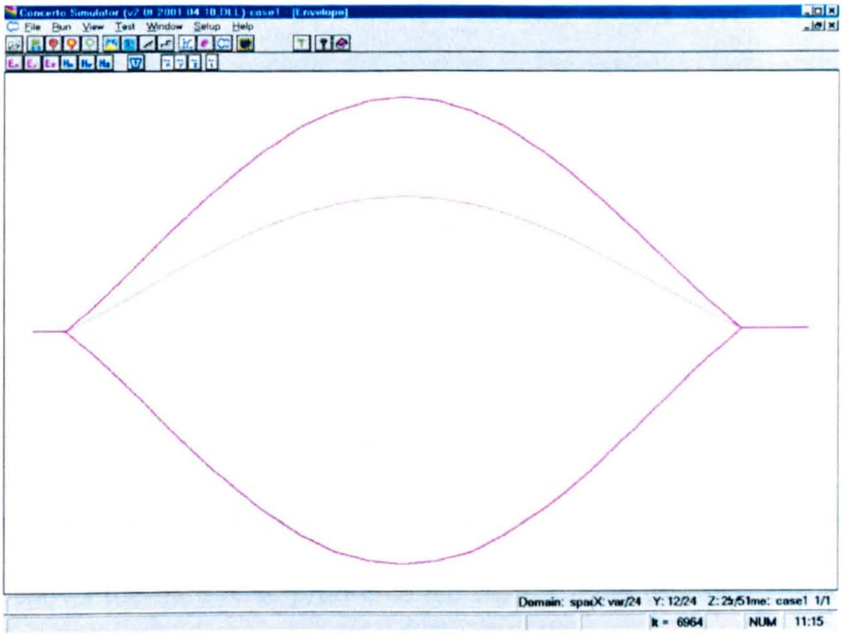

Figure 7.4. Electric field profile inside an empty circular waveguide.

7.2.2. The loaded circular cavity

In this part of the design process, a dielectric tube was added to the model described in the section above. For simulation purposes, this tube was assumed to have an inside diameter of 15 mm, an outside diameter of 20 mm and a dielectric constant of 10. Because the waveguide was now partially loaded, the calculation of the effective permitivity required by CONCERTO had to be found "manually" using a sub-routine in CONCERTO itself. An effective permitivity of 4.43 was found. Analytically, the wavelength at 12.4 GHz was found to be 0.547 mm^{-1} corresponding to a guide wavelength of 11.5 mm. The results obtained from CONCERTO (Figure 7.5) indicated a wavelength of 12mm. As can be seen the accuracy would have been improved by reducing the mesh size but at the cost of increased computing time.

Comparing Figure 7.3 with Figure 7.5, it is obvious what a difference the insertion of the dielectric has made to the wavelength of the em wave (each plot was made at the same frequency of 12.4 GHz). The wavelength in the loaded cavity has been significantly decreased (by a factor of about 5.5) which implies that the wavenumber has increased by the same factor. This indicates a reduction in the phase velocity of the propagating wave ($u_{ph} = \omega/\beta$) as expected because of the effect of the dielectric liner. Figure 7.6 shows the transverse profile of the electric field in a partially loaded cavity. This plot of E_Z as a function of radial position z clearly shows the discontinuous change in slope E_Z suffers at the vacuum dielectric boundary, and the dip in the field strength towards the axis. This dip is due to the fact that the synchronous frequency is some distance away from the intersection of the light line and the dispersion curve.

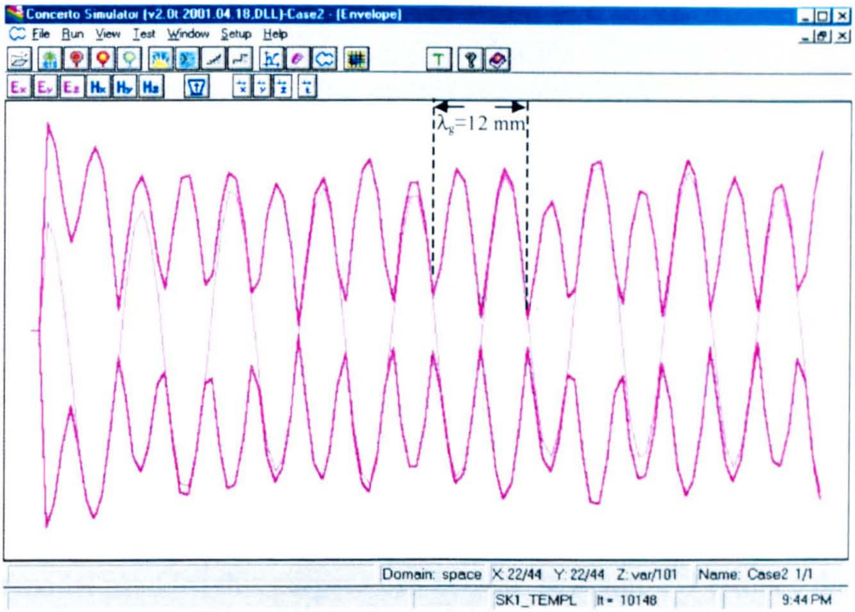

Figure 7.5. Standing wave inside a partially loaded cavity.

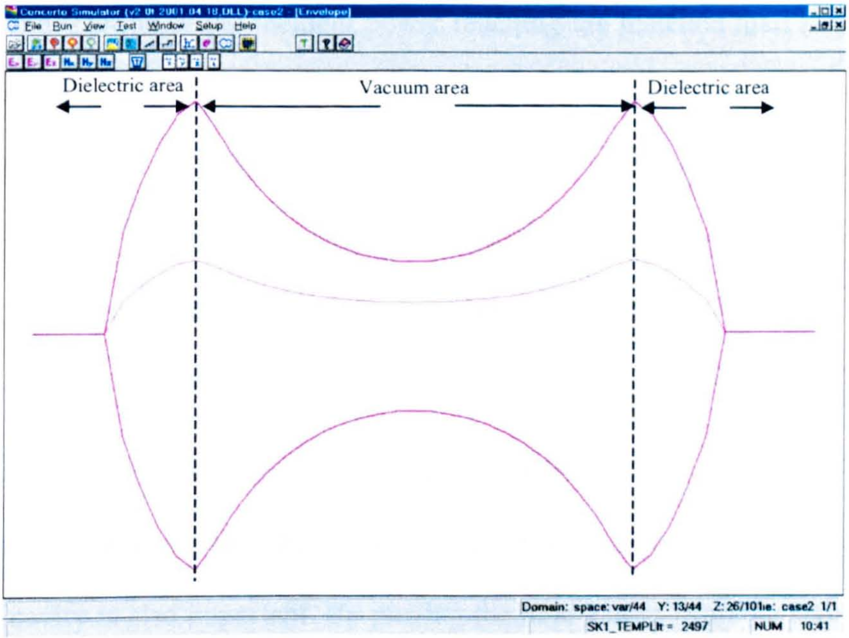

Figure 7.6. Electric field profile inside a partially loaded circular waveguide.

7.2.3. The coupling hole

An important factor in the design of the first system was to find a way to couple out a small fraction of the power from inside the partially loaded cavity. The simplest method was by means of a small hole in the side of the circular waveguide, leading to a rectangular WR75 guide. The choice of the size of the hole was significant, as it was vital not to couple out a large amount of the power inside the cavity. Using CONCERTO, the effects of altering the hole diameter on the amount of coupling was investigated. The simulation model used for this purpose can be seen in Figure 7.7 (Notice that the relative size of the arrows indicates the power of the wave propagated or reflected inside the system). Figure 7.8 shows the variation of $|S21|$ versus the size of the hole.$|S21|^2$ represents the fraction of the incident power reaching the matched load at the end of the rectangular guide. From previous experience, it was estimated that the circulating of microwave power level in the guide when the FEL was operating in saturation would be about 100 Watts. The microwave detection system requires power levels of the order of milliwatts so it was necessary to couple out about 10^{-5} of the power in the cavity. This gives $|S_{21}|$ equal to $\sqrt{10^{-5}}$, i.e. about 3×10^{-3}. It can be seen that (Figure 7.8) a suitable size of coupling hole is then approximately 2 mm in diameter.

It should be noted that the position of the hole relative to the short circuit at the end of the cavity is also important. By placing the hole 23mm from the short circuit end, that is at a magnetic field antinode, it was possible to maximise the magnetic coupling through the hole. As a result, it was possible to minimise errors due to mechanical accuracy and to allow the coupler to operate with a constant coefficient over a reasonable bandwidth close to synchronism.

7.2.4. The coupler

Having completed the design of the individual sections of the coupler, the whole design was simulated with CONCERTO and the scattering parameters found. Due to the complexity of the model, it was decided to use a 0.5mm mesh size in the x and y direction, in order to achieve a detailed and accurate result. A complete simulation then required 16 hours running time.

As can be seen in Figure 7.9, the power reflected from the short circuit at the end of the cavity is practically 100%, as the power coupled out by the circular hole is so small, and losses in the guide walls and the dielectric liner could not be modelled by CONCERTO. In Figure 7.10 where the |S21| parameter is calculated, the coupling coefficient depends on frequency. This is because as the frequency is altered, the positions of the magnetic antinodes move. From this Figure, it can be seen that at the required frequency of 12.4 GHz, the coupling coefficient is a maximum with a value now of 2.5×10^{-3} and a bandwidth of 0.8GHz.

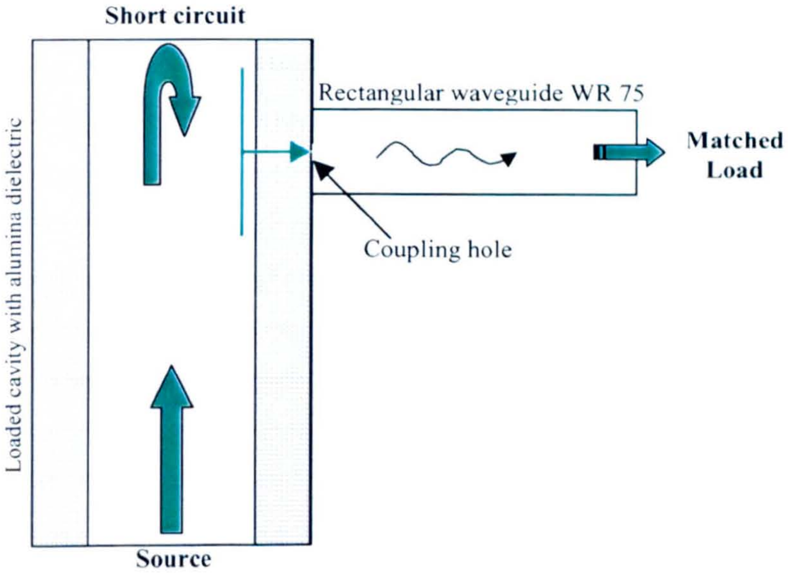

Figure 7.7. Representation of the simulated model for choosing the right hole diameter.

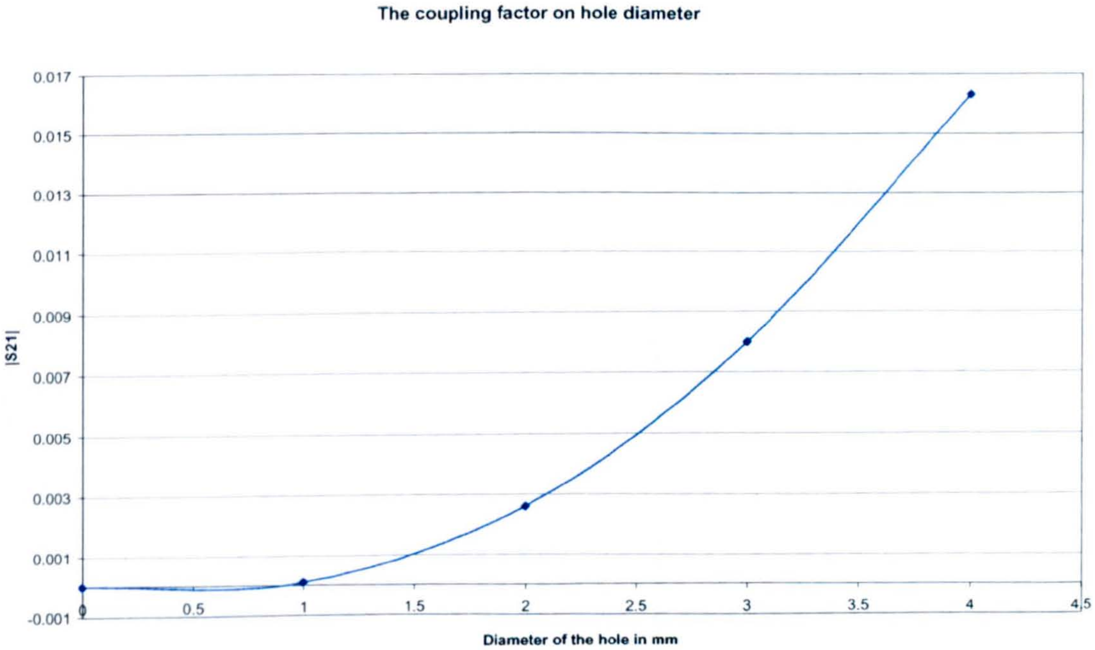

Figure 7.8. Coupling variation with respect to the diameter of the coupling hole diameter.

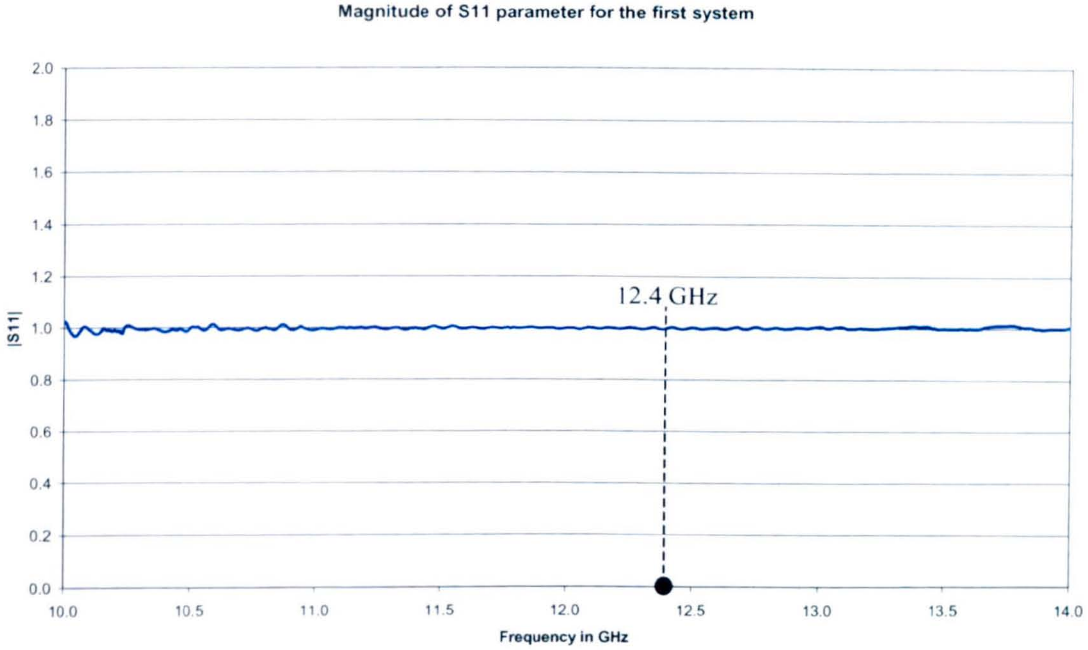

Figure 7.9. Graph showing the amount of power trapped inside the partially loaded cavity.

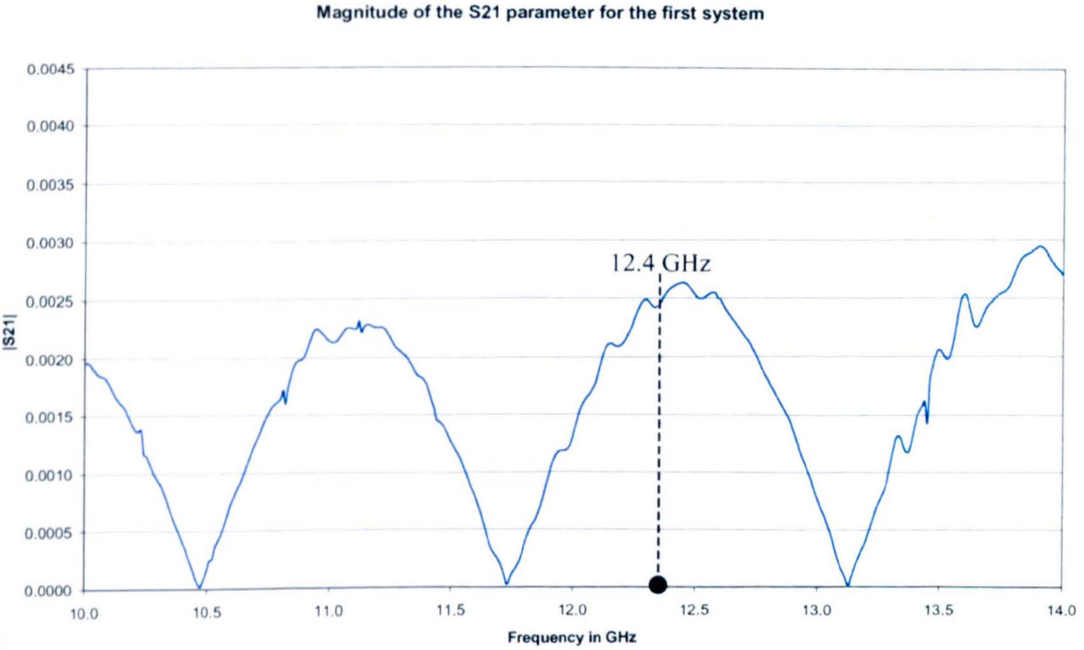

Figure 7.10. Graph showing the simulated variation of the coupling coefficient |S21| as a function of frequency, for a 2mm diameter hole at 23mm from the short circuited end of the cavity.

7.3. The system gain

For the design of the system shown in the earlier sections of this chapter, it was assumed that the outer diameter of the dielectric tube was 20 mm and the inner diameter was 15 mm. It was also assumed that the dielectric constant of the alumina tube was 10. The tube ordered from Alfa had a total length of 600 mm. All this information regarding the characteristics of the alumina tube were taken into account in order to estimate the small signal gain of the system at 12.4GHz. This was calculated using a MathCAD program file [44]. In this program, the input beam current was taken to be 120 mA while the accelerating voltage was varied in the vicinity of 70 kV. Figure 7.11 shows a graph of the gain as a percentage against the accelerating voltage. It can be seen that for this system the maximum gain was 30% at about 72 kV, while at 70 kV, the synchronous voltage, the gain is zero.

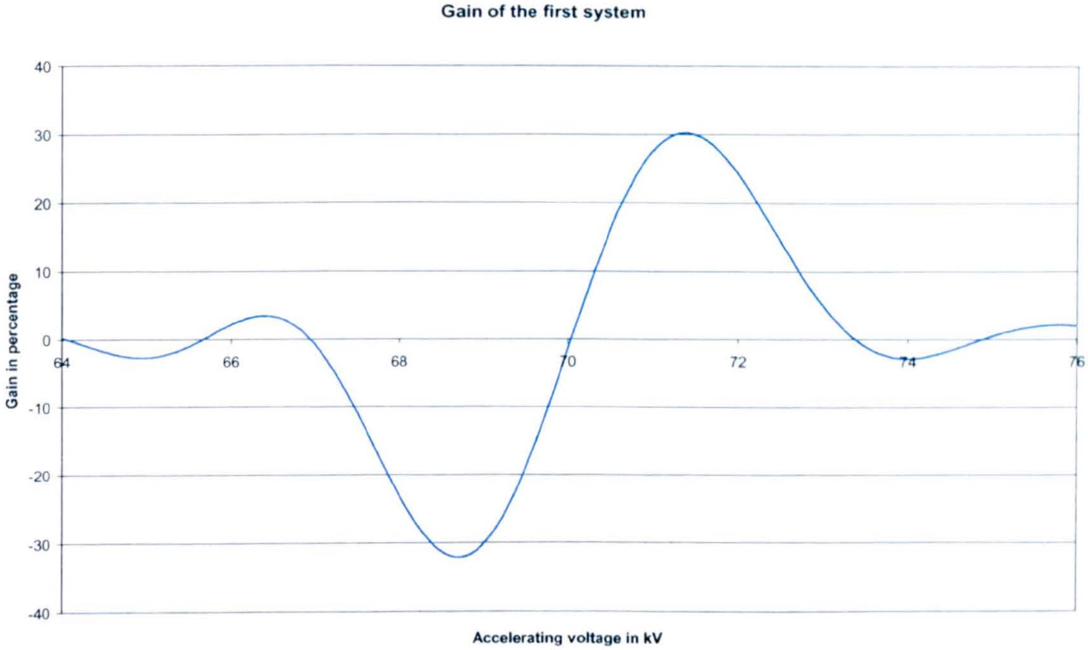

Figure 7.11. Gain of the first system.

Chapter 8

Results of the First System

8.1. Introduction

The theoretical design having been completed, the next stage was to produce mechanical drawings for the laser. It was very early decided to align the loaded cavity vertically as this would not only minimise the space required but, also more importantly, would reduce the frequency of breakdowns that might occur between the high voltage components and the working bench. This orientation allowed the distance between the bench and the first high voltage component to be more than 100 mm so that breakdowns were expected to be very unlikely. The turbo-molecular pump suspended at the lower end of the system was sufficiently heavy to ensure the stability of the system. It was also decided to position the coupling branch towards the lower end of the cavity to allow the focusing solenoid to slide up and down the main length of the cavity. Furthermore, instead of resting the whole weight of the coil on the vacuum components, a simple supporting tripod was built. The internal diameter of the solenoid was just over 22 mm so that it could be fitted over the circular waveguide (external diameter of 22 mm) with only a little room to spare. This meant that radial adjustments of the solenoid relative to the waveguide were not possible and hence the movement of the coil to improve the quality of the beam focusing was restricted to the axial direction. If the solenoid had to be removed for any reason, it was thought that this restriction of movement would allow it to be replaced accurately. Finally, the problem of measuring the total current reaching the end of the cavity (using the HP Versatile Link Transmitter described in Chapter 3), without taking into account any stray currents was overcome by placing a thin glass ring (about 5 mm high) at the top of the system, separating the main circular waveguide from the current collector. A drawing showing the whole system assembled can be seen in Figure 8.1.

8.2. The electron beam through the loaded cavity

In order to achieve sufficient electron beam transport through the whole length of the loaded cavity, the electromagnet described in Chapter 6, had to be in place. However, it was not known how much current should be passed through the coil in order to achieve the maximum possible electron beam transportation. It was decided to first supply the coil with one 12 V battery then add another in series and so on and observe the effects on the collected electron beam current. Figure 8.2 shows the current collected as a function of the gun cathode voltage for one, two and three batteries in series. Also shown for comparison is the current emitted by the cathode, which represents the maximum current that could be achieved. At low cathode voltages, practically all the available current is collected and little variation is observed as the number of batteries is changed. At higher cathode voltages, the collected current saturates as a value lying between 70 and 90 mA depending on the current through the electromagnet coil.

This output current saturation was believed to be due to the fact that there may have been a small misalignment between the beam and the cylindrical cavity. As mentioned earlier, the only adjustment that could be made to the coil, apart from varying its magnetic field strength by changing the number of batteries across its terminals, was to move the coil axially along the length of the cavity. However, this movement did not increase the output current. The only other possible alternative was to use external permanent magnets at key positions to attempt to eliminate the initial beam angle. The existence of a weak magnetic field between the electron gun and the cavity could force the electron beam back in line and improve the alignment between the cavity and the beam. In order to achieve this it was decided to place a set of 4 permanent magnets in a square configuration on the flange connecting the main circular cavity to the basic system. The 4 permanent magnet configuration is shown in Figure 8.3. From the figure it can be seen that the magnets are placed in such a position that their magnetic fields are directed radially and away from the centre of the device. This configuration was simulated using PE2D and a two dimensional contour of the magnetic field pattern can be seen in Figure 8.4. The 4 permanent magnets are represented by the blue rectangles. This arrangement of the four magnets allowed one magnet to compensate the magnetic field of the other and therefore to produce a very weak field in the centre of the configuration.

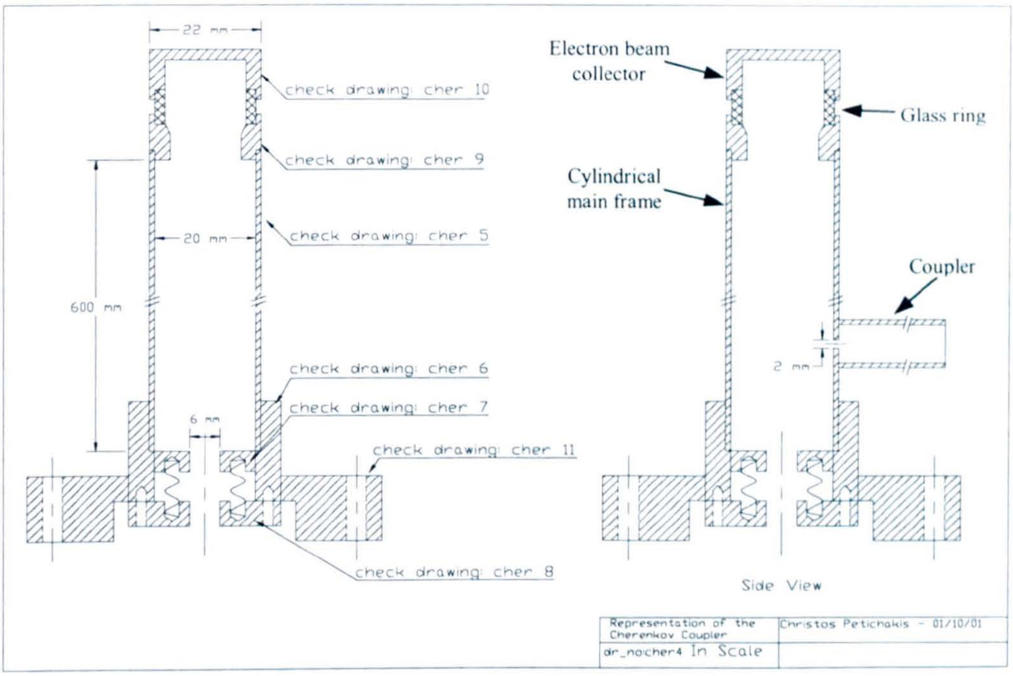

Figure 8.1. Technical drawing of the first Cerenkov Free Electron Laser.

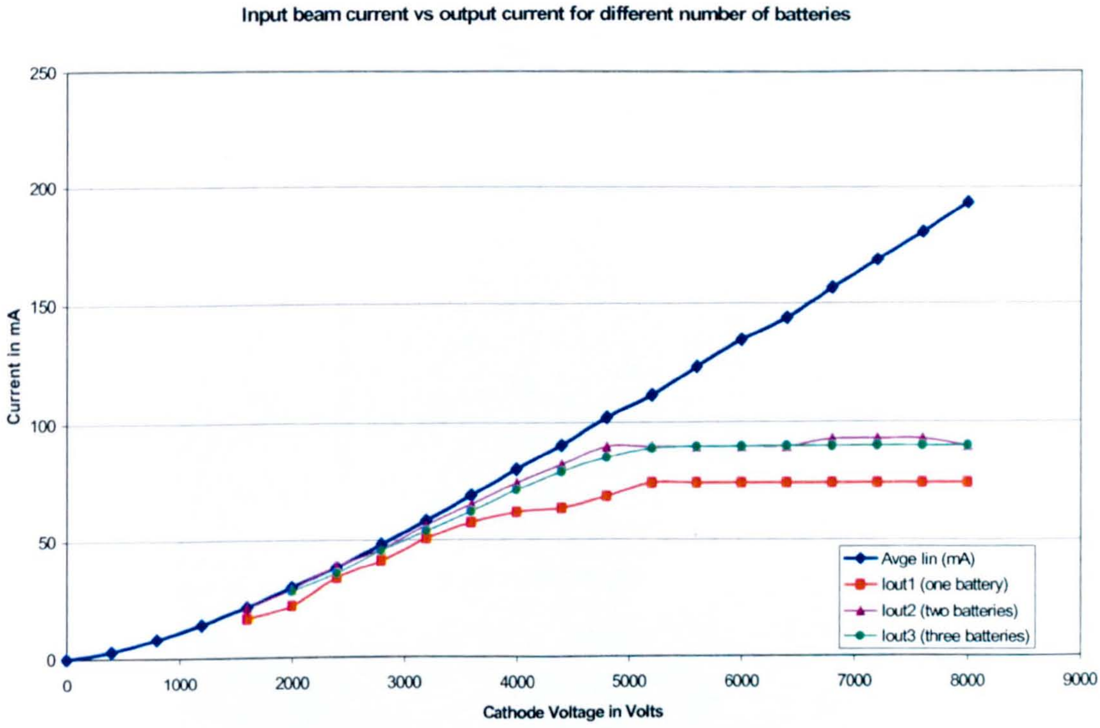

Figure 8.2. Graph showing the variation of the output current on the gun cathode voltage applied. across the coil.

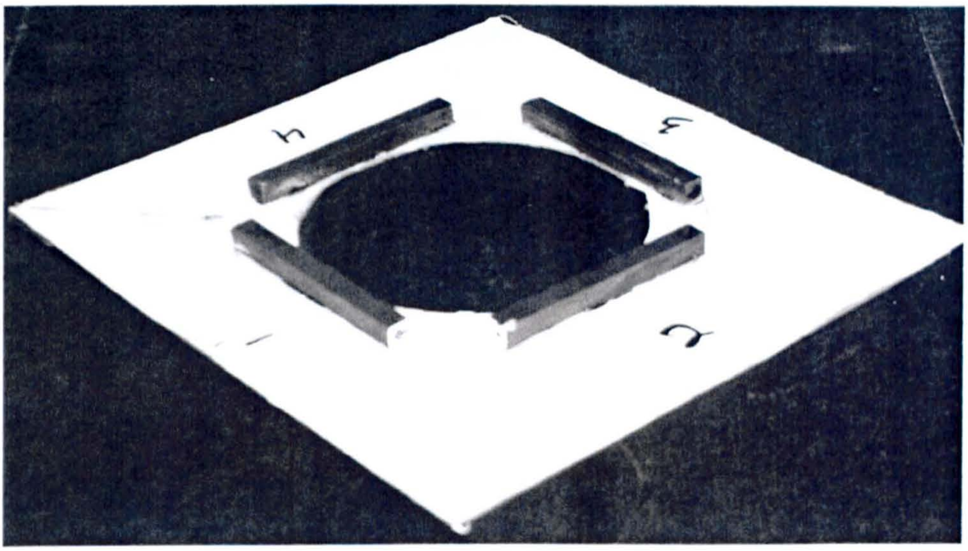

Figure 8.3. Pre coil beam focusing permanent magnet configuration.

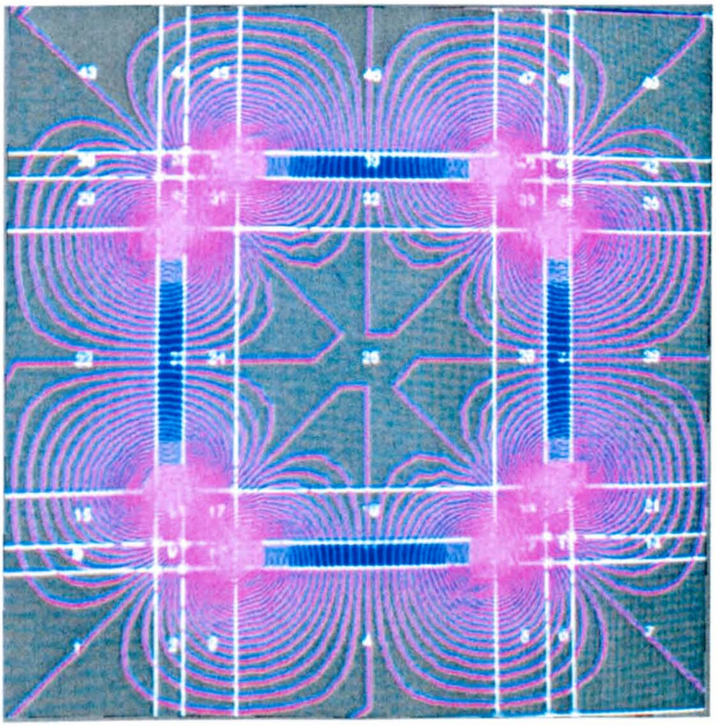

Figure 8.4. Contour view of the magnetic field lines of the permanent magnets configuration.

It was then a matter of experimenting with the position of these permanent magnets in order to achieve the optimum result. Evidence for the successful operation of this device can be seen in Figure 8.5.Now, the output current followed the input current closely, indicating that nearly the whole electron beam was able to travel along the length of the loaded circular waveguide with little interception. Above about 4kV cathode voltage, the collected electron beam current was of the order of 95% of the available cathode current. This result was achieved using three 12 Volt batteries connected in series with the solenoid terminals.

After these experiments were completed, the apparatus was disassembled and the electron beam collector was examined (Figure 8.6). A region close to the centre of the collector was clearly damaged by the impact of the high energy electrons which further indicates the high efficiency of electron beam transport through the cavity.

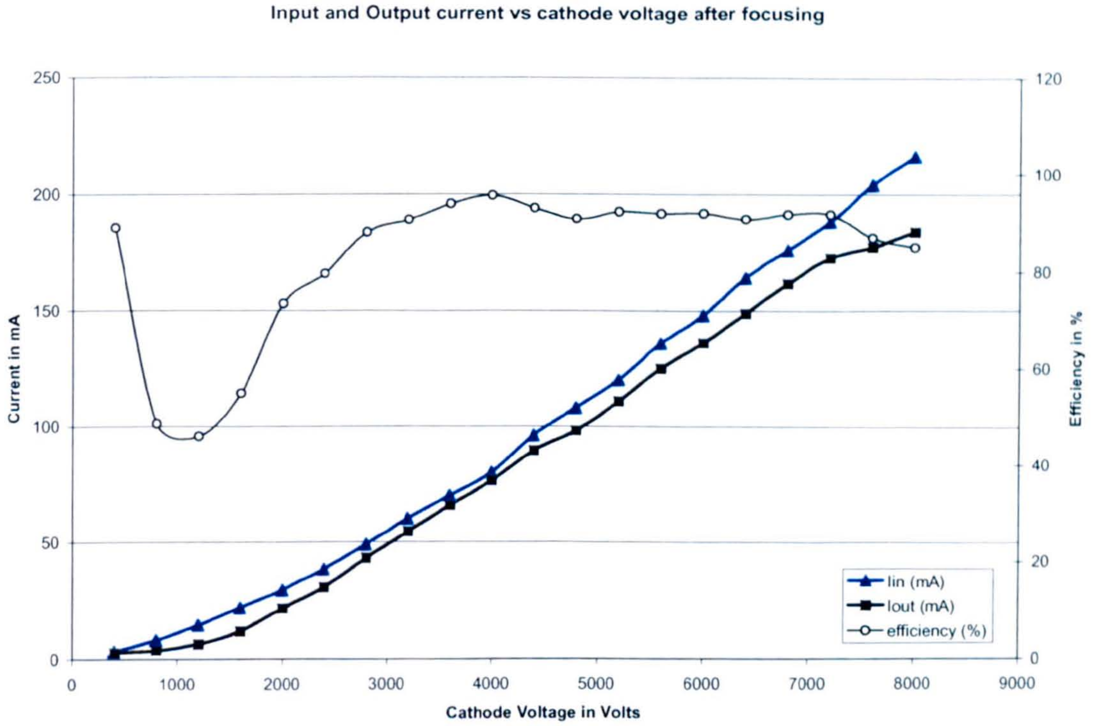

Figure 8.5. Efficiency of the electron beam traveling the whole length of the cavity.

Figure 8.6. Beam burn mark.

8.3. First system results and conclusions

As described in the previous chapter, the small signal gain calculated for this system was around 30% at 120mA electron beam current. A satisfyingly high transmission of the electron beam through the whole length of the loaded cavity had been achieved and hence it was time to check for microwaves. A microwave horn was connected to the end of the rectangular waveguide that was coupled to the cavity, and another horn was placed opposite to it and connected to a microwave detector diode (as shown in Figure 8.7). The microwave detector was then connected to the oscilloscope.

Unfortunately, no observable microwave output could be detected even with a maximum electron beam current of 120mA pulsed for 25μs.

One possible explanation for this lack of output was that the losses in the waveguide walls and in the alumina dielectric were together greater than 30% so that net gain was not achievable even at the highest beam current level. Consequently, it was decided to redesign the system to give a higher gain, which it was hoped would be greater than the losses.

Although no microwaves were achieved at this stage, the achievement of high electron beam transport using a solenoid was significant and encouraged the construction of the next system. In addition the very limited number of high voltage breakdowns occurring while running the first system, showed that the layout of the apparatus was sensible.

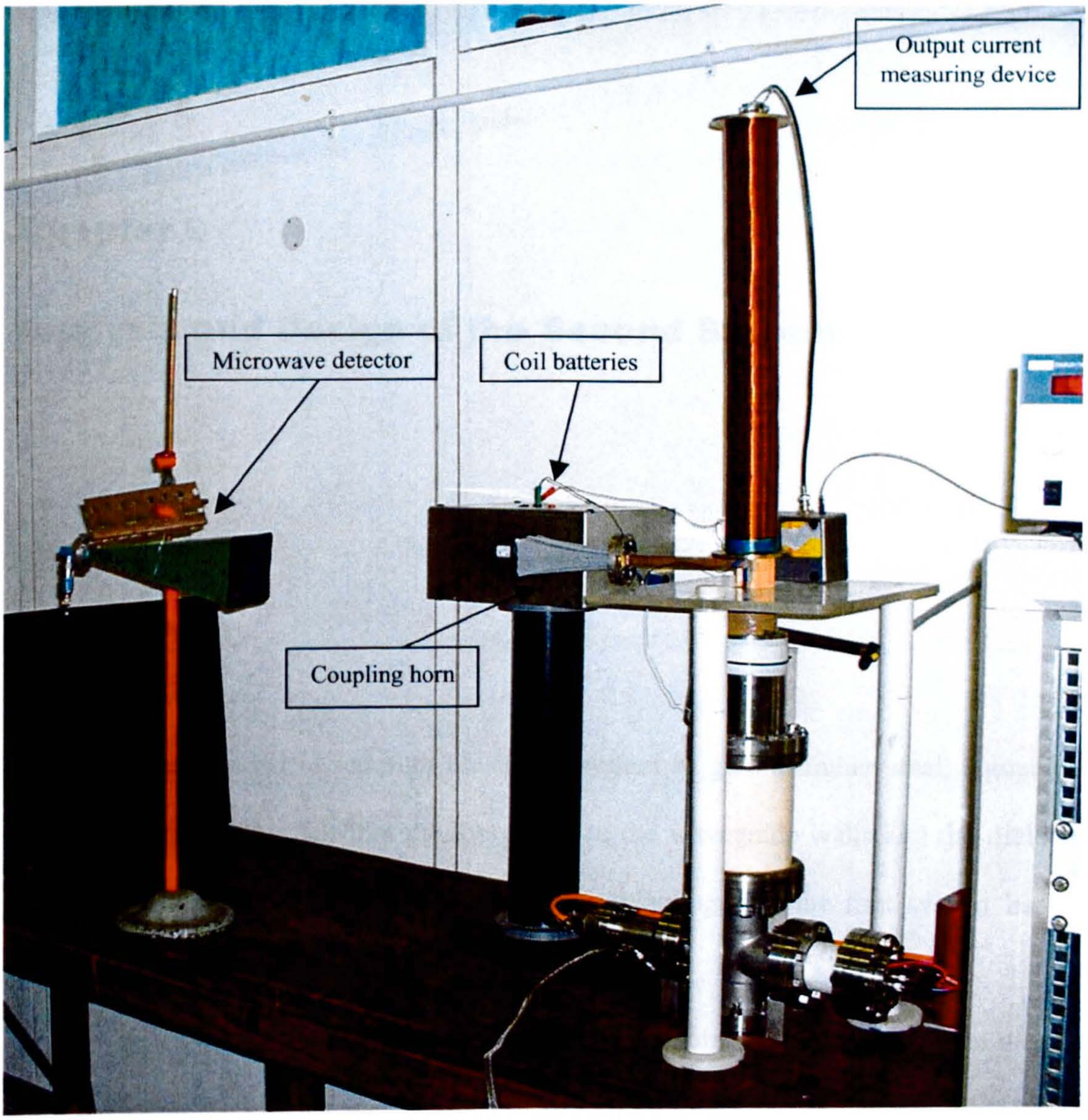

Figure 8.7. The first system.

Chapter 9

Analysis and Design of the Second System

9.1. Introduction

It was decided to redesign the initial system to give a higher small signal gain than 30% since it was felt that the losses due to the waveguide walls and the dielectric liner could possible be of this order, thereby explaining why the first system had not produced any microwave output.

The main principle of the new system was the same as before. Again an alumina liner loaded into a circular waveguide would be used to achieve the interaction between the electromagnetic wave and the electron beam. The dimensions of the new copper circular waveguide, after some trial and error, and taking into account the sizes of the available dielectric liners were 10.4 mm outer diameter and 10 mm for the inner diameter. The outer diameter of the alumina liner was 10 mm while the inner was 6 mm. Once again the alumina tube was to be supplied by Alfa.

For the mechanical design of the second system, CONCERTO software was again used, simulating each part of the design separately in order to have a complete view and a thorough understanding of state of the electromagnetic wave inside the new system.

9.2. Theoretical design of the second system

As before, the very first step was to calculate the dispersion relation that describes this new system. Figure 9.1 shows the dispersion diagram of the dielectrically loaded circular waveguide with the dimensions given above. Also shown for comparison are the light line, the electron beam line and the dielectric line. This time the interaction point has moved to the higher frequency of 16.92 GHz with a wavenumber of 0.755 mm^{-1}. With this information, it was possible to start developing the simulation models to be used in CONCERTO and these included:

1. The coupling section
2. The probe
3. The top end,

as illustrated in Figure 9.2. The operation of each of these three sections is reported in the next pages of this chapter.

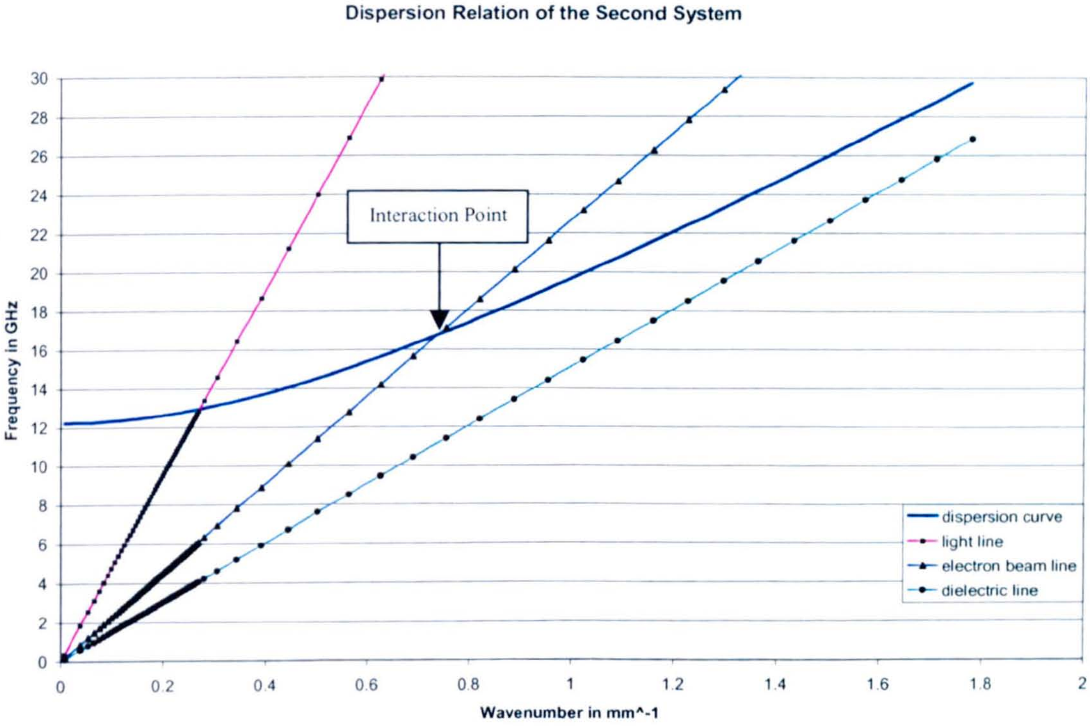

Figure 9.1. Dispersion relation of the second system for an alumina tube with id=6mm, od=10mm and er=10.

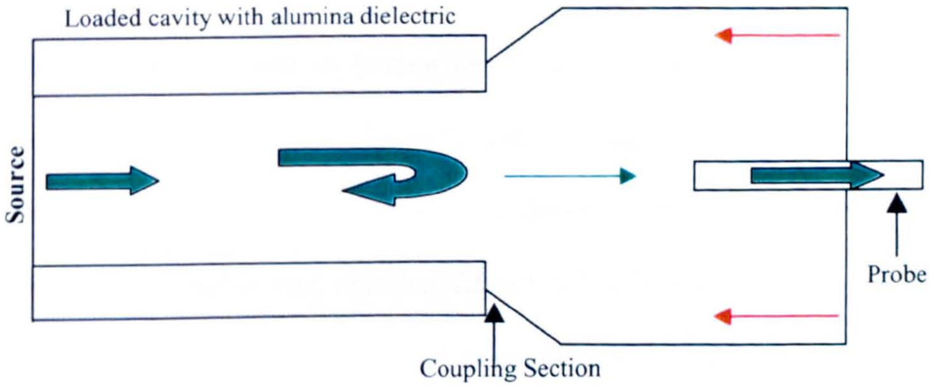

Figure 9.2. Schematic diagram of the second system showing the three components that have to be simulated using CONCERTO. (Note that the green arrows indicate the propagating power while the red the reflected, also the size of the arrow indicates the amount of power transmitted or reflected).

9.2.1. The coupling section

The model to be simulated consisted of a circular waveguide with inner diameter of 10 mm, loaded with an alumina tube (ε_r=10) of 10 mm outer diameter and 6 mm inner diameter. To couple power out of the main loaded cavity, it was initially decided to add a short piece of circular waveguide after the dielectrically loaded cavity, as shown in Figure 9.3. However, this unloaded circular waveguide section has a cut off frequency of nearly 23 GHz, far above the expected operating frequency close to 16.9GHz. As a result, a wave propagating inside the loaded cavity towards this end would become evanescent, and if the cylindrical section is long enough, 100% of the incident power is reflected back.

In order to let a known fraction of the wave couple out, it was decided to place a circular guide with larger diameter after the loaded cavity in order to make sure that the wave leaving the loaded section of the cavity would continue to propagate inside the newly added guide. A section having an internal diameter of 16 mm and a cut off frequency of 14.3 GHz was therefore added (Figure 9.4). After simulating this configuration, two main conclusions were drawn. The first was that the coupling coefficient was far higher than required. In fact 35% of the total power was coupled out, which meant that the net gain of the system could be seriously jeopardised. This problem can be solved by adding a small iris at the junction between the end of the liner and the unloaded waveguide section (Figure 9.7a). The coupled out power can be reduced to any suitable value by correct choice of the iris aperture diameter. A number of simulations were performed on this system so that the size of the iris piece could be found. The results from these simulations can be seen in Figure 9.8. From this graph, it can be seen that for a 1mm wide iris, the transmitted power is approximately 7% of the incident microwave power.

The second problem identified was that the TM_{01} mode incident on the junction from the cavity suffers partial mode conversion into higher modes. Figure 9.5 shows the transverse envelope of the longitudinal electric field of this propagating wave produced by the simulation. Figure 9.6 shows the theoretical profiles of the longitudinal electric field for the TM_{01} and TM_{02} modes. Clearly, the mode propagating through the guide is some Fourier combination of mainly TM_{01} and TM_{02} modes.

In order to deal with this mode conversion problem (which would make the CONCERTO calculations of the coupling efficiency unreliable), it was decided to add a small tapered section at the end of the loaded cavity, to make the transition from unloaded to unloaded guide less sudden. This tapered section had to be kept reasonably short so that the propagating wave would not be too severely attenuated in the regions where it is cut off. Because of the step discontinuity between the main loaded cavity and the empty taper, which functioned as an iris (Figure 9.7b), it was expected that the majority of the microwave power would be reflected back and only a small amount would be transmitted through the taper to the output coupling probe as required.

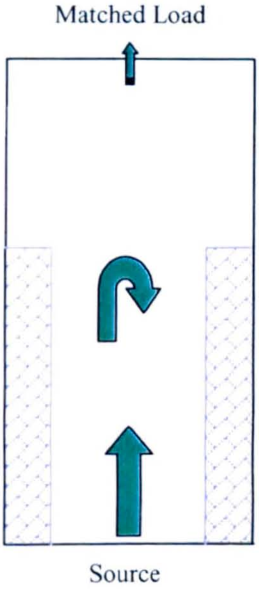

Figure 9.3. Schematic diagram of the initial coupling system.

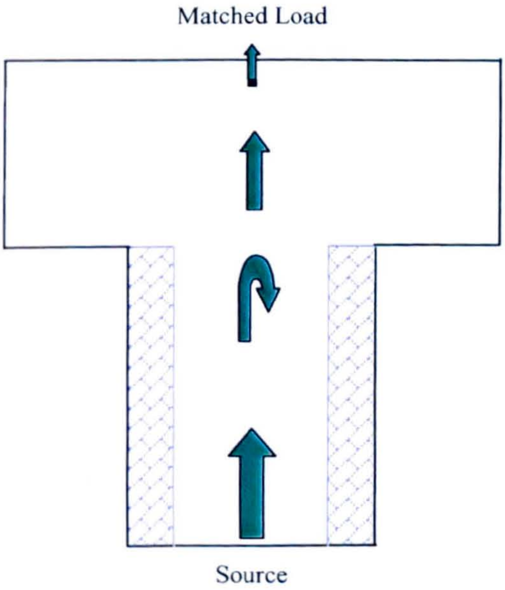

Figure 9.4. New schematic diagram of the coupling section.

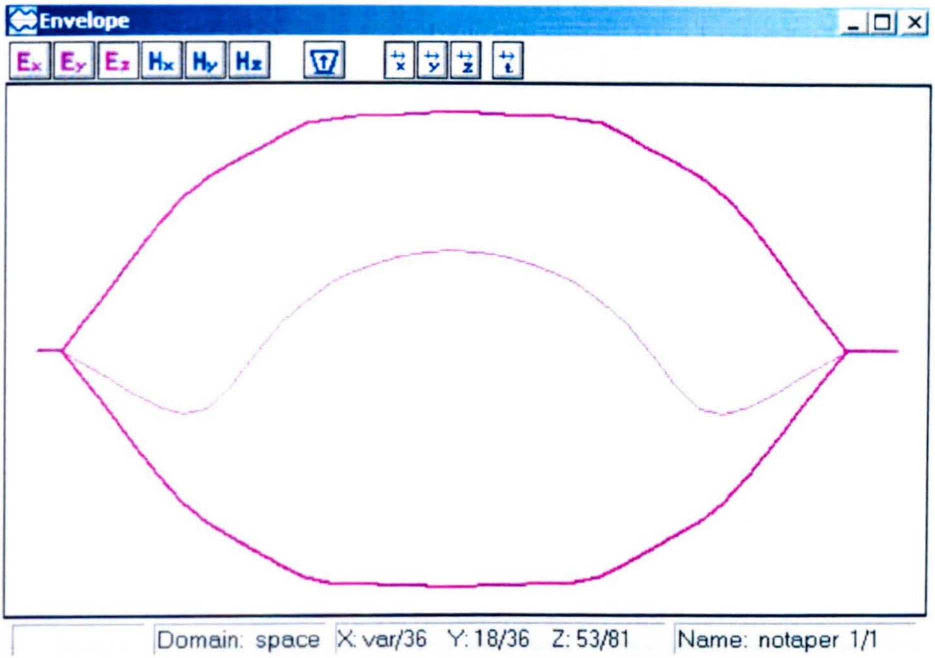

Domain: space X: var/36 Y: 18/36 Z: 53/81 Name: notaper 1/1

Figure 9.5. Envelope of the resulting mode in the enlarged and extended waveguide.

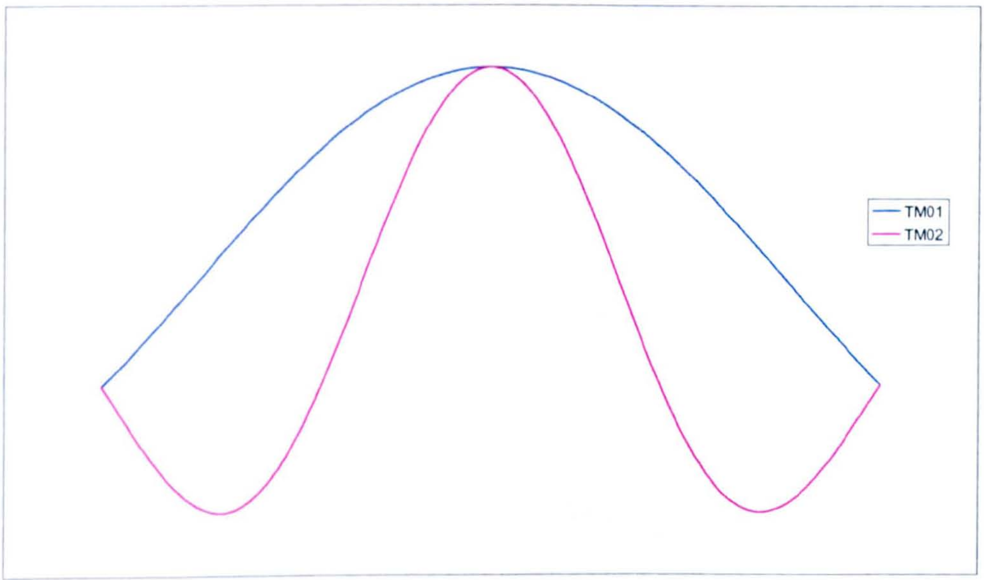

Figure 9.6. Axial profile of the electric field for the TM_{01} and TM_{02} modes.

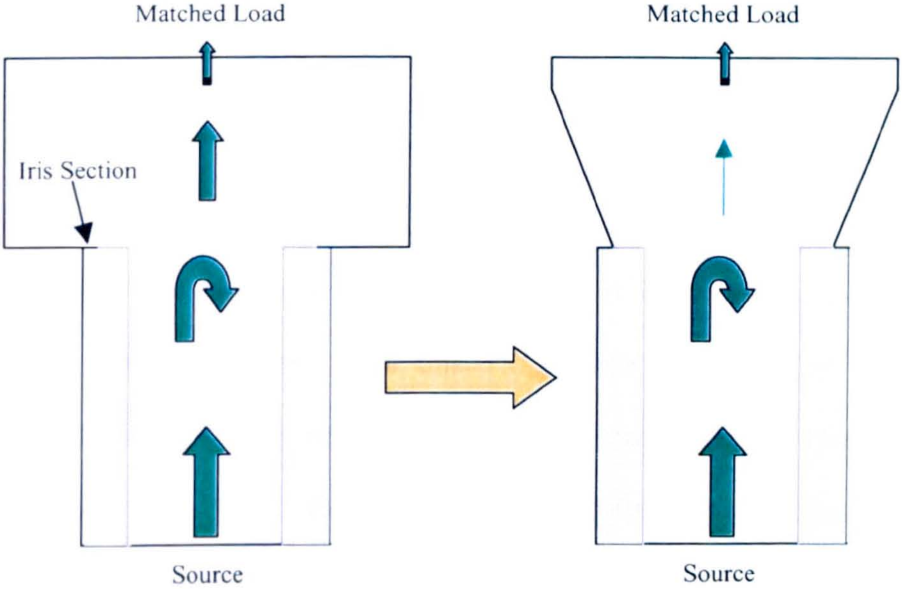

Figure 9.7. This picture illustrates the effect in the power coupled out by using or not a tapered section at the end of the loaded cavity.

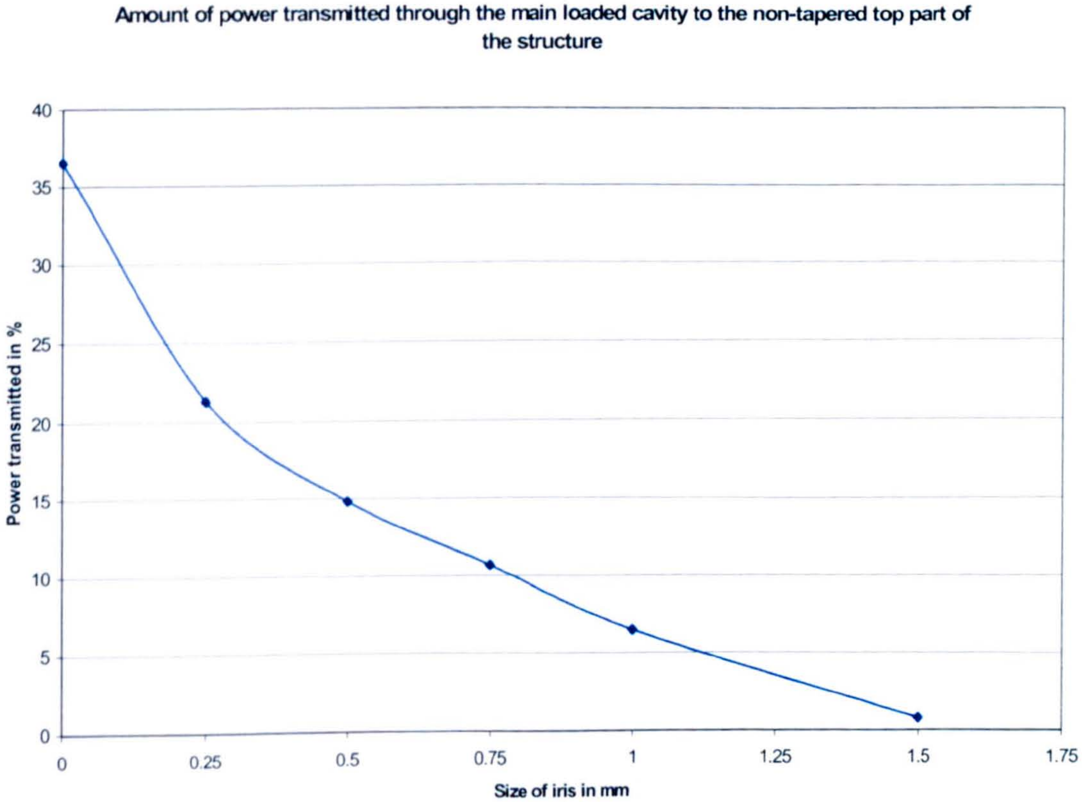

Figure 9.8. Graph illustrating the dependence of the power transmitted from the loaded to the tapered section of guide as a function of the iris width w.

With this tapered section added to the end of the loaded cavity the magnitude of the |S21| factor was found to be 0.1514 at 16.92 GHz, which translates to 2.3% of the incident power coupled out, while the remainder, 97.7%, being reflected back into the cavity. This result can be seen in Figure 9.9.

Even with this tapered transition, a small part of the TM_{01} mode was still converted into TM_{02}. However, since this TM_{02} mode is cut off in the unloaded cylindrical guide, it is gradually reflected back into the loaded section. This is illustrated in Figure 9.10 there are two envelopes of the wave showing the axial electric field as a function of the radius just after the taper and near the end of the empty circular waveguide 60mm away. Clearly, the mode is now very nearly pure TM_{01} mode.

Having completed this part of the design, the next stage was the conversion of the TM_{01} mode into a TEM coaxial cable mode at the upper connector.

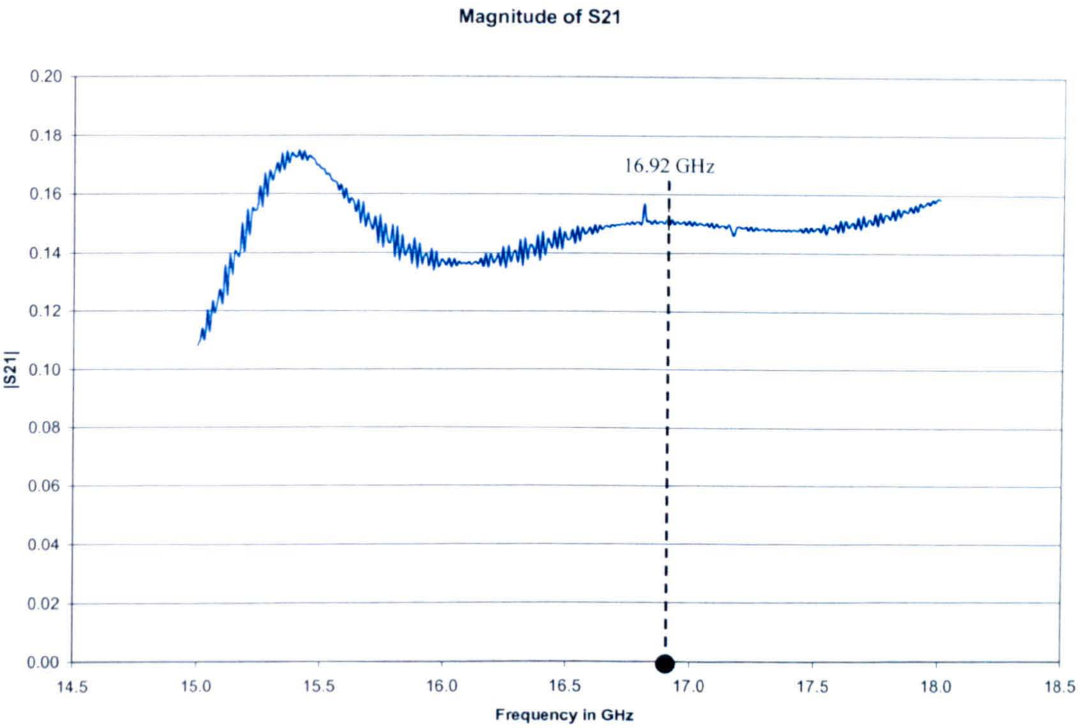

Figure 9.9. Magnitude of the wave propagated from the loaded cavity into the tapered section.

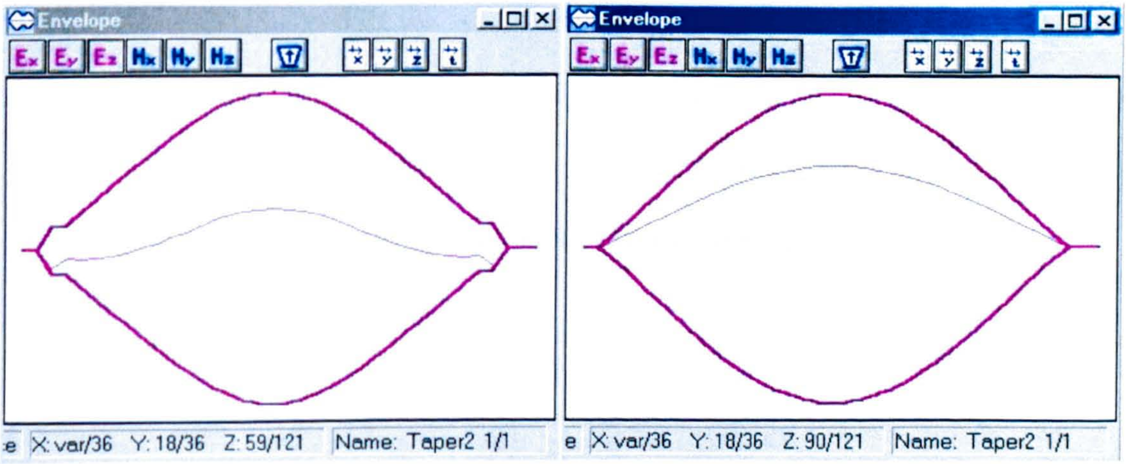

X: var/36 Y: 18/36 Z: 59/121 Name: Taper2 1/1

X: var/36 Y: 18/36 Z: 90/121 Name: Taper2 1/1

Figure 9.10. The left part of the figure shows the state of the wave just after the taper, where the TM02 mode component is small but clearly visible. On the right, the TM02 mode can be seen to have been effectively removed leaving almost a pure TM01 mode component.

9.2.2. The probe

A probe that would transit most of the power coupled out of the loaded cavity and the tapered transition into a coaxial line had to be designed. A schematic diagram of the proposed design is shown in Figure 9.11. The probe was to be supported by a small perspex ring glued to the walls of the copper cylinder as shown.

By simulation, it was found that the values of the length and diameter of the probe and also the diameter of the coaxial section (d=12 mm) were crucial if efficient operation of this part of the system was to be achieved. After many trials with different probe dimensions, it was found that a probe with diameter of 2 mm and extending down for 7.5 mm within upper part of the tapered transition section could transmit 91% of the microwave power into the coaxial section. Note that the total length of the probe was 23 mm.

Figure 9.12 shows the variation of the |S21| parameter as a function of frequency for this probe length. As can be seen, the coupling coefficient was designed to have a maximum in the vicinity of 16.9GHz, so that the coupling would be broadband.

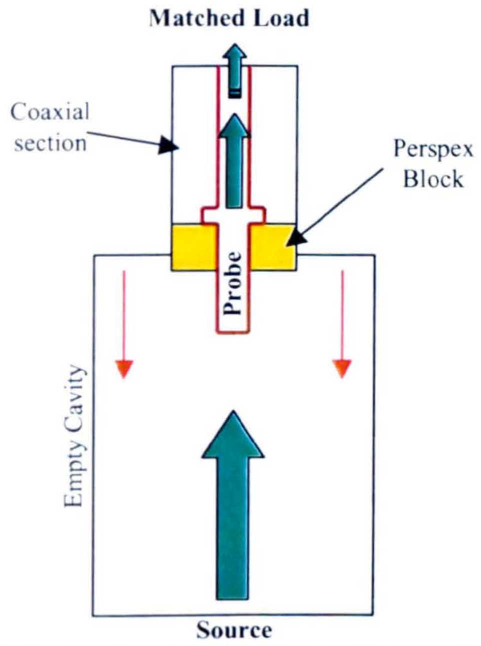

Figure 9.11. Schematic diagram of the probe analysis showing that most of the wave transmits through the probe to the top end of the system.

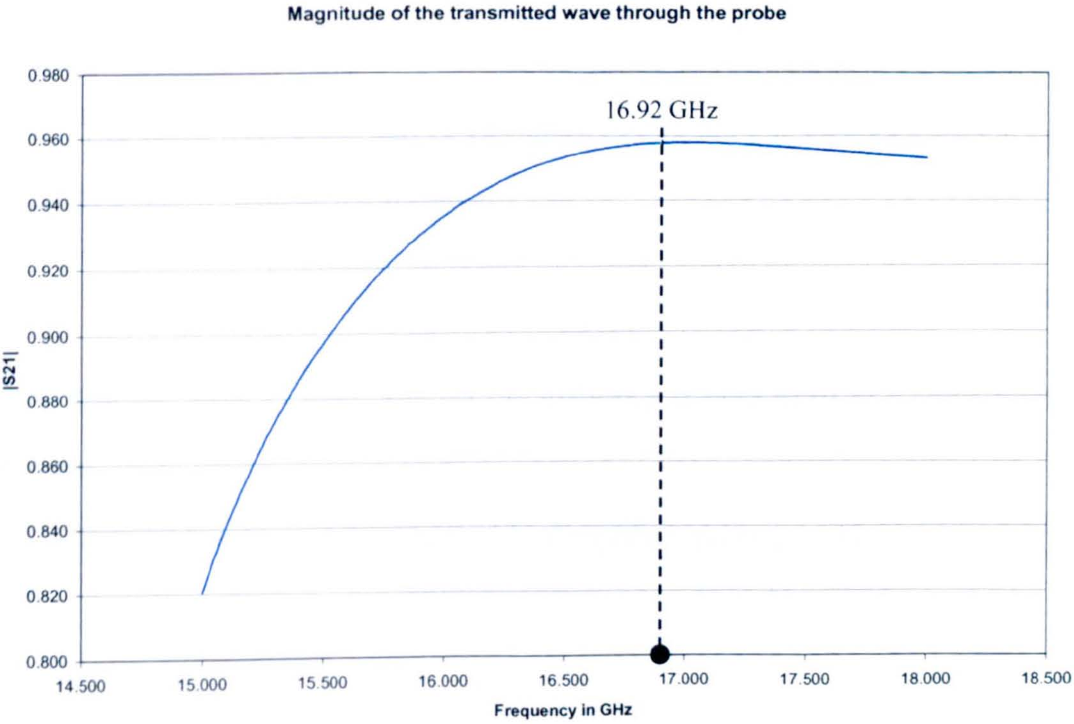

Figure 9.12. Magnitude of the transmitted wave through the probe at 16.92 GHz.

9.2.3. The top end

The final part of the design process was to model and simulate the transition between the coaxial section and a rectangular guide which was to transport the microwave power to a detector diode, as shown schematically in Figure 9.13. The CONCERTO drawing (Figure 9.13) is based on this idea. However, it was later decided to use a standard N-type connector and connect directly to a horn in order to simplify the construction of the system. This modification did not affect the results of the initial model, which will be presented below.

The aim here was to see how the probe transfers the available power to the rectangular waveguide. By placing the probe at a distance of a quarter of a rectangular guide wavelength, $\lambda_g/4$, from the short circuited end of the rectangular waveguide [45], it is possible to feed all the available power from the probe to the end of the guide.

The guide wavelength may be calculated as follows. For a rectangular waveguide, the guide's cut off frequency is given by

$$f_c = \frac{c}{2a} \qquad 9.1$$

where c is the speed of light. The cut off frequency is then equal to 9.366 GHz when a=16mm.

Using this value and the equation for the guide wavelength, (Equation 9.2),

$$\lambda_g = \frac{\frac{c}{f}}{\sqrt{1-\left(\frac{f_c}{f}\right)^2}} \qquad 9.2$$

gives λ_g = 21.3mm at the expected operation frequency of 16.92 GHz. Consequently, $\lambda_g/4$ = 5.3mm. Hence in order to achieve maximum transmission from the probe to the rectangular waveguide, the probe has to be inserted 5.3 mm from the short-circuited end of the rectangular guide and 4 mm high inside the guide. The result of the simulation with this value can be seen in Figure 9.14. At 16.92 GHz, |S21| is equal to 0.9956 which is means that 99.1% of the power flowing in the coaxial section is coupled into the rectangular guide.

Figure 9.15 summarizes the reflection and transmission values at each of the junctions modelled.

9.3. The system gain

The MathCAD package was used to estimate the gain available for a system having a 600 mm length alumina tube having a 10mm outer diameter, a 6mm inner diameter and a dielectric constant of 10 (Figure 9.16). With an input electron beam current of 120 mA the small signal system gain was found to be more than 1200% at about 71 kV at 16.9 GHz. It was considered very unlikely that the losses in the waveguide walls and the dielectric tube would even approach this figure.

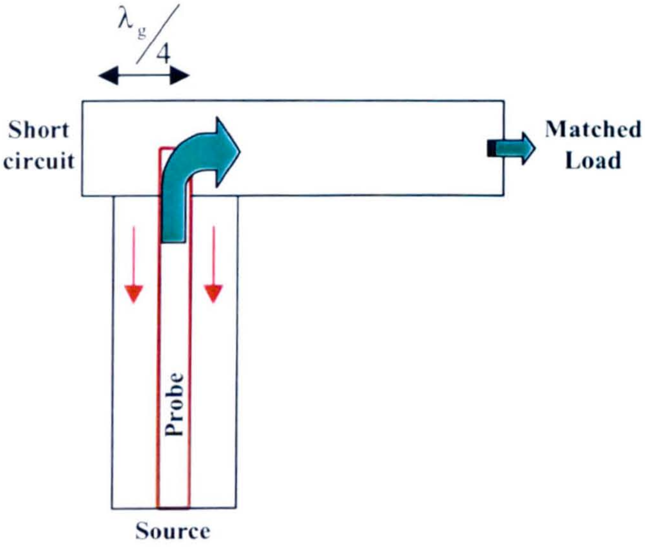

Figure 9.13. Schematic diagram of the top end of the system.

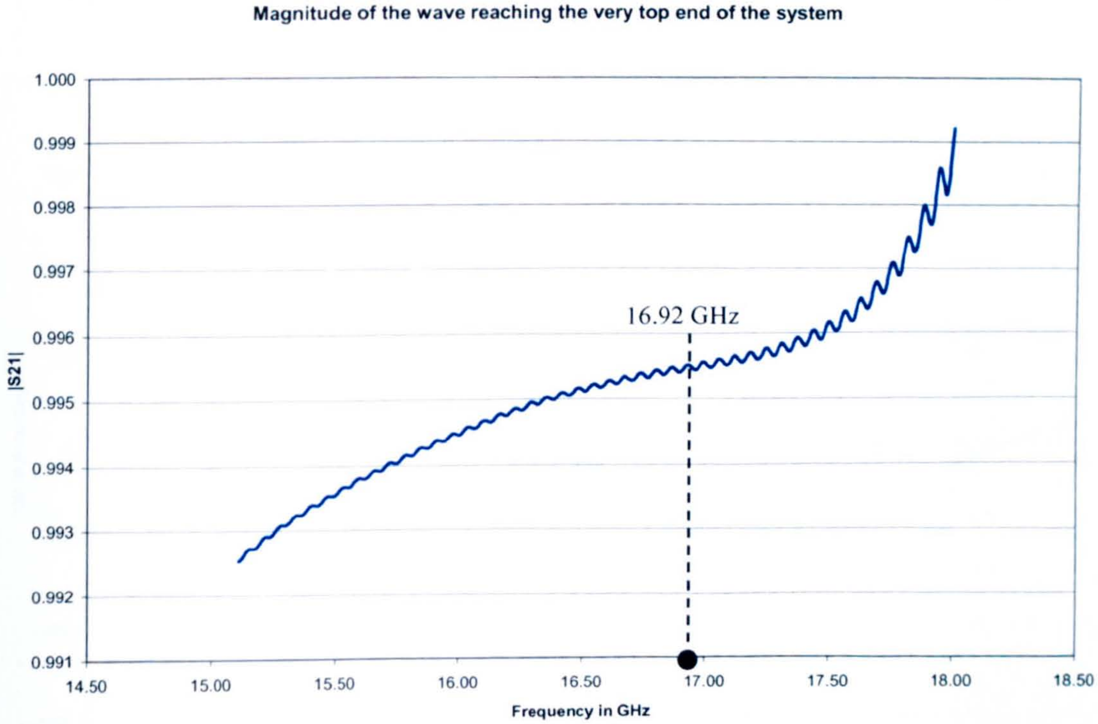

Figure 9.14. This graph shows the amount of the wave reaching the top end of the system.

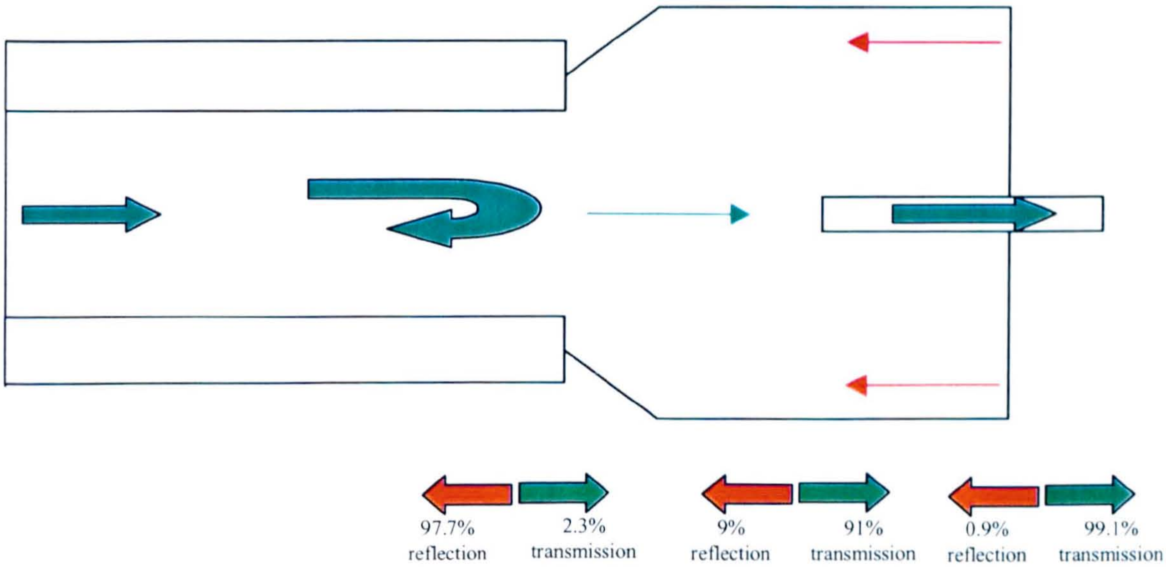

Figure 9.15. Illustration of the reflection and transmission of the wave inside the system.

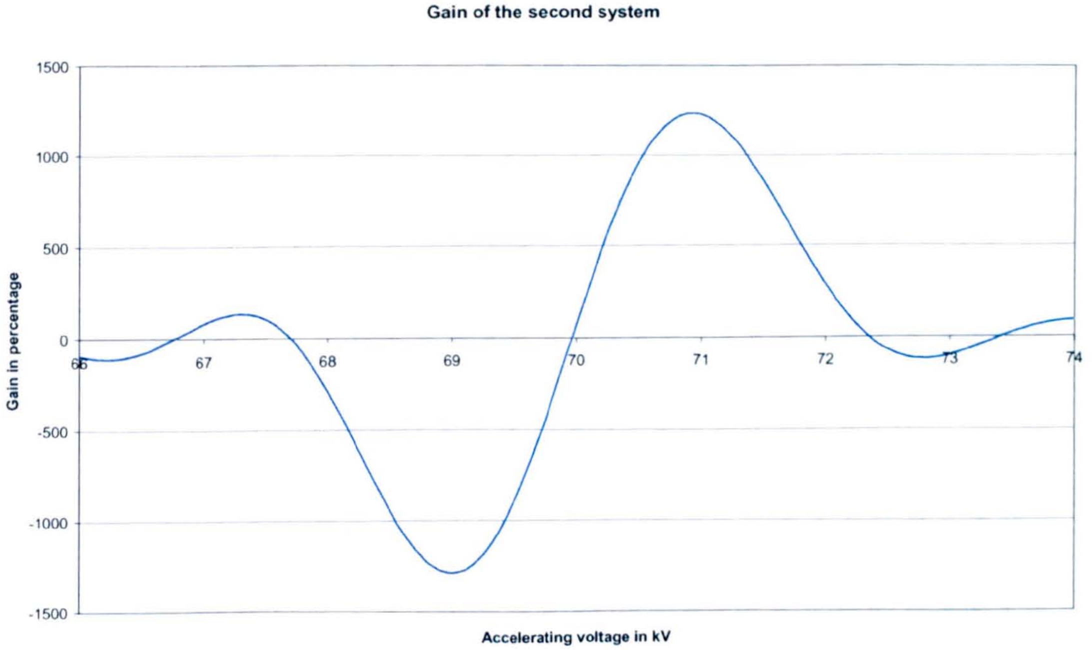

Figure 9.16. Gain of the second system at 16.9 GHz.

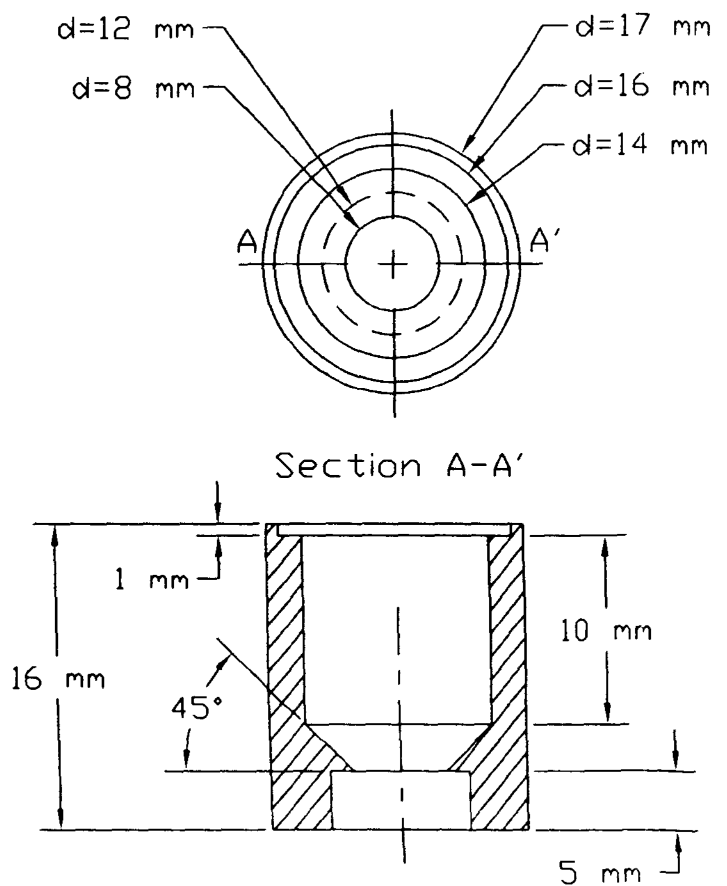

Glass Connector		Christos Petichakis - 27/2/02
dr_no:beam test no6	In Scale	Material: Copper

Chapter 10

Second System Results

10.1. Introduction

After simulating the whole system using CONCERTO, as in the case of the first system, the next stage was to produce the drawings in order to construct a second Cerenkov laser. Again, it was decided to build the system with the electron beam directed vertically as the main base and vacuum systems were already available and it was a simple procedure to install the new cavity. As before, a tripod was used to support the coil. The initial electron beam current measurements were performed using the solenoid to aid beam transport but without the steel housing. However, it was decided that in order to improve beam transmission, a solenoid housing was important as described in Chapter 6. The steel housing added a significant amount to the total weight of the solenoid and this made its vertical and sideways adjustment difficult. At the same time, the extra weight added extra pressure to the tripod. Therefore, at this stage, it was decided to change to a horizontal configuration. In order to minimise the possible breakdowns occurring between the high voltage components and the workbench, a rectangular piece of Perspex, 7 mm thick, was placed on the top of the bench. Next, two stands with adjustable heights were made in order to support the solenoid and these gave the user the ability to move the coil both along and transverse to the cavity axis with significant accuracy (fractions of a mm). Since the outer diameter of the cavity was 10 mm and the inner diameter of the coil nearly 22 mm, there was a sizeable gap between the two components which allowed a good deal of transverse adjustment of the solenoid's axis relative to that of the cavity.

For initial measurements, the set up shown in Figure 10.1 was constructed. The same current measurement system, as described earlier in Chapter 3 was used again to measure the electron beam current reaching the collector. The results were compared with the cavity input current so that the efficiency of the electron beam transmission could be estimated.

After some experiments, it was decided that the best transmission results could be achieved by using four 12 V batteries. This supply led to a solenoid current of nearly 3 Amps and a created magnetic field of around 500Gauss. The beam transmission through the cavity was then excellent with efficiency levels greater than 90% for cathode voltages above about 2kV. A graphical representation of the beam efficiency can be seen in Figure 10.2. Also, in Figure 10.3, the burn mark of the electron beam close to the centre of the collector verified the good beam transportation.

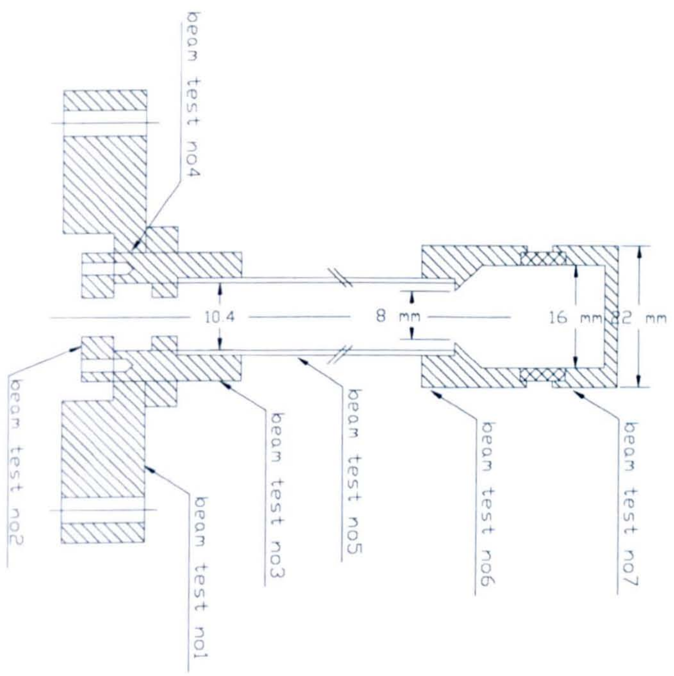

Figure 10.1. The electron beam test system.

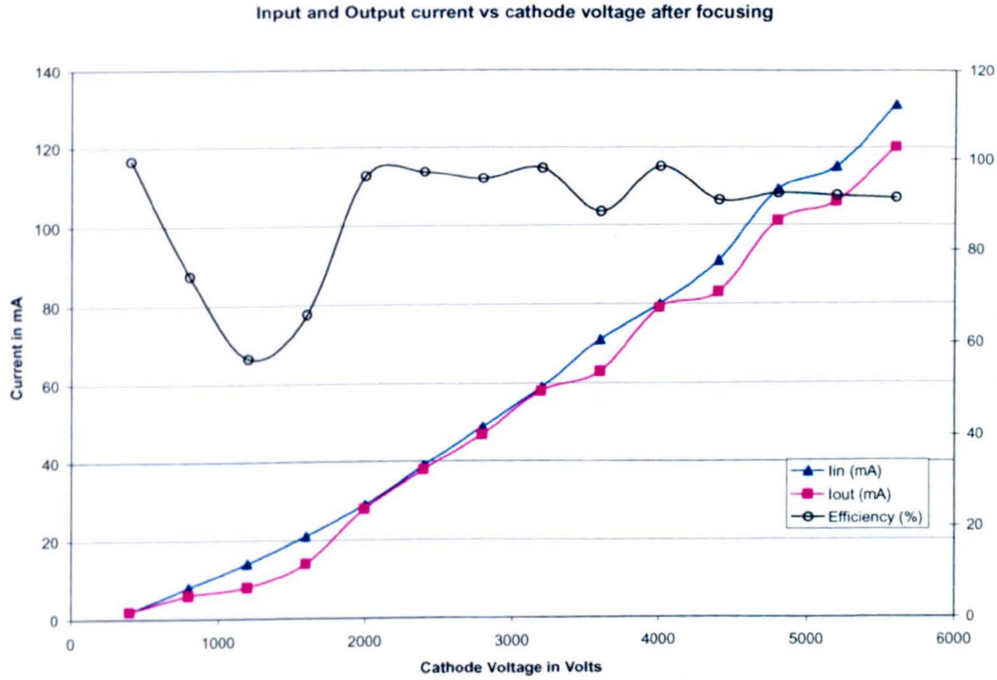

Figure 10.2. Efficiency of the electron beam traveling the whole length of the cavity.

Being satisfied with the efficiency of the electron beam transportation, the collector end of the cavity was desoldered and replaced with the probe section as shown in Figure 10.4. Because the probe was glued to a perspex block, it would be catastrophic to let the electron beam hit this small perspex surface. Therefore, an external deflecting magnet was placed just before the probe tip. Deflecting the electron beam here would have no effect on the system's performance but would save the perspex block from damage leading to a vacuum failure. Figure 10.5 shows this beam-deflecting device. It consists of a steel tube partially cut away fitted with two permanent magnets. The steel tube forms a path taking the flux round the magnetic circuit from one side of the gap to the other. This device was used to provide a magnetic field at right angles to the direction of propagation of the electrons, thereby providing a deflection of the beam. A picture showing all the major components of the second system can be seen in Figure 10.6.

10.2. Second system results and conclusions

Having achieved a nearly 94% average efficiency in electron beam transmission, and having calculated that the small system electronic gain should be more than 1000%, the system was confidently checked for microwave output. Again two horns were used, one at the end of the system connected by an N-type connector to the probe, while the other horn was connected to the microwave detector and then to the oscilloscope. Electron beam current pulses of 120mA lasting up to 25 µs were passed through the waveguide, but disappointingly, no microwave output was detected. This result was extremely puzzling in that all the microwave simulations carried out seemed to indicate a satisfactory design, and even if the "small signal" gain was not equal to 1250%, the simulation results indicated that the gain should have been sufficiently large to overcome any conceivable losses.

However, it was decided that the dielectric material composing the liner should be investigated. In view of the non-operation of the device, two questions had to be answered. Firstly, was its dielectric constant really 10, remembering that the manufacturer's data was only for 10MHz rather than 10GHz? If it was not, synchronism would be at an entirely different electron beam voltage and consequently there would be possibly be no microwave output to observe. Secondly, were the losses in the dielectric sufficiently high to kill the gain?

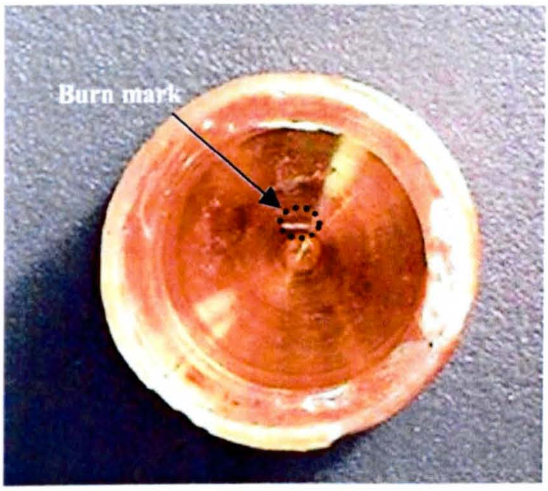

Figure 10.3. Beam burn mark.

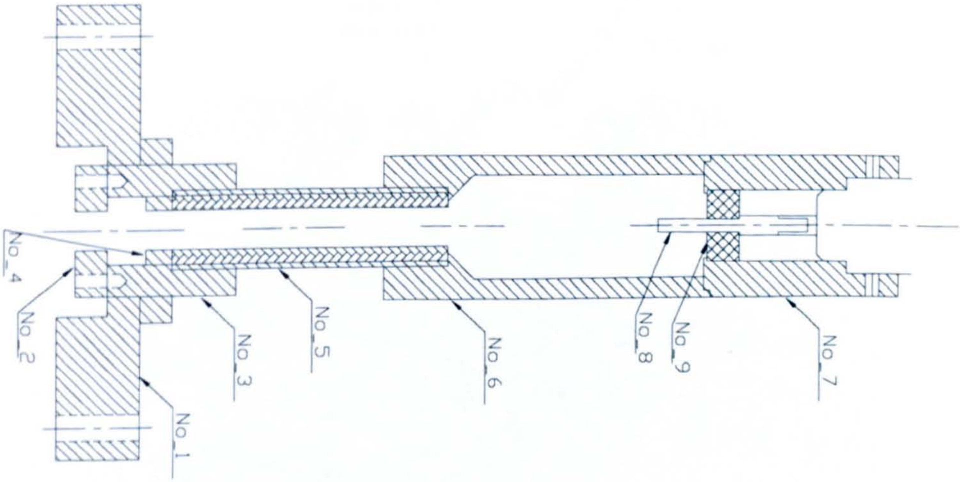

Figure 10.4. Technical drawing of the second Cerenkov Free Electron Laser.

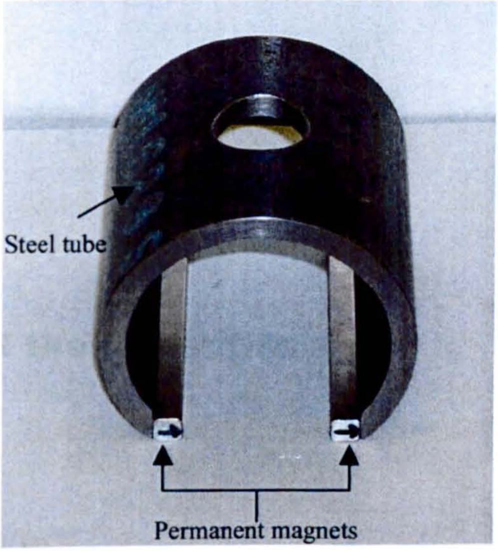

Figure 10.5. The beam deflecting magnet.

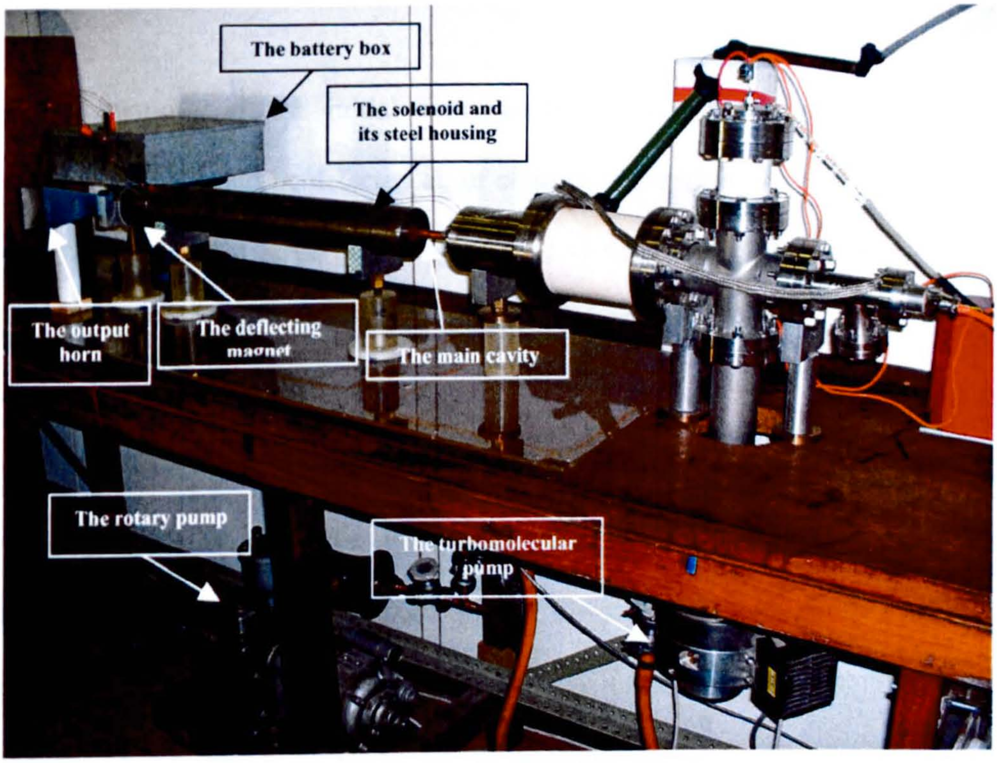

Figure 10.6. The second system.

Chapter 11

The Analysis of the Dielectric

11.1. Introduction

Up to now, all the initial experiments had proved disappointing, in that no microwave output could be detected at, or close to, the expected synchronous voltage, in spite of the fact that a large percentage of the electron beam was thought to be being transported through the dielectrically loaded cylindrical guide in both systems. Several possible reasons were investigated such as the coupling from the cavity to the external waveguide system. Another possibility was that the dispersion relation was affected by the thickness variation of the dielectric along the length of the liner [46]. However, when none of these possible solutions seemed to be the answer, it was decided to investigate the properties of the dielectric material itself. It was felt that an important first step would be to measure the dispersion curve for the dielectrically loaded system experimentally [47] and compare the results with the initial theoretical predictions. It was thought that this would give us an experimental handle on both the value of the dielectric constant and the loss tangent of the material.

11.2. The measurement of the dispersion curves

The resonance method was used to measure the dispersion curve of a dielectrically loaded tube [48]. In this technique a section of cylindrical guide is short-circuited at both ends to form a resonant cavity, and has a small probe close to one end to excite the cavity. A representation of the experimental set-up can be seen in Figure 11.1. By observing the power reflected by the cavity, it is possible to find a series of resonances. A typical example of such a series is shown in Figure 11.2.

Resonances occur at frequencies such that there is a whole number of half wavelengths in the length of the guide. If this is L, then this condition gives,

$$n \cdot \frac{\lambda_{g,n}}{2} = L \tag{11.1}$$

where $\lambda_{g,n}$ is the n^{th} resonant guide wavelength with n an integer from 1 upwards. The corresponding wavenumbers β_n are given by,

$$\beta_n = \frac{2\pi}{\lambda_{g,n}} = \frac{n\pi}{L} \tag{11.2}$$

which can be easily calculated.

Consequently, by measuring the resonant frequencies, f_n, and deducing β_n it is possible to draw the dispersion curve, f_n vs β_n. Note that it is sometimes difficult to detect the n=1 resonance because its closeness to cut off where guide attenuation is high and hence Q of the resonance is low. However, experience has shown that it is normally possible to find this resonance if sufficient care is taken and the dielectric is not too lossy. A second more difficult problem is that the TE_{11} mode has a lower cut off frequency than the TM_{01} mode. Even though the probe was specifically designed to excite TM_{01} resonances only (by correct choice of its shape), it was found that TE_{11} mode resonances were also easily observable and confused the detection of the TM_{01} resonances in the frequency range where they overlapped. Although it was possible to distinguish between the two types of mode resonances, since the TE_{11} type were found to be doublets due to the fact that the copper tube was not perfectly circular, a better solution was to cut 4 longitudinal slots in the guide at 90° to each other and then surround the guide with a layer of "Teledeltos" conducting paper. The TE_{11} mode radiates power out of these slots whereas the TM_{01} mode does not. As a result the TE_{11} mode is heavily attenuated and its resonances disappear, leaving only the desired TM_{01} to be measured.

11.3. Results

The measurements were performed on a copper tube of 20.2 mm internal diameter and 301 mm length, loaded with an alumina furnace tube having internal diameter 14.7 mm and external diameter 19.8 mm obtained from Alfa. The manufacturers quote the dielectric constant ε_r as being 9.2 at 10 MHz, 20 °C with a loss tangent of 2×10^{-4}. Most other observers [49,50] however quote ε_r as being 9.9 at GHz frequencies for their material. The sample tube used was stated to have 99.7% purity with an apparent density in the range of 3.7 to 3.95 g/cm^3, with a grain size of 10 μm and zero porosity.

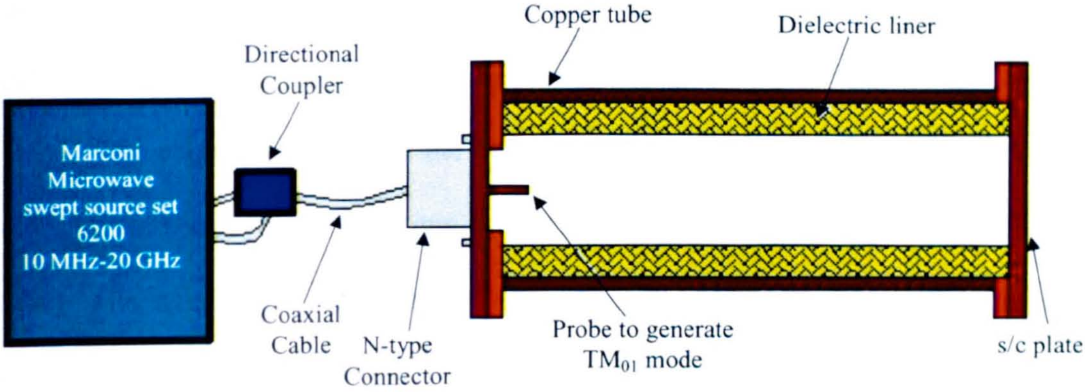

Figure 11.1. The resonant cavity and testing apparatus.

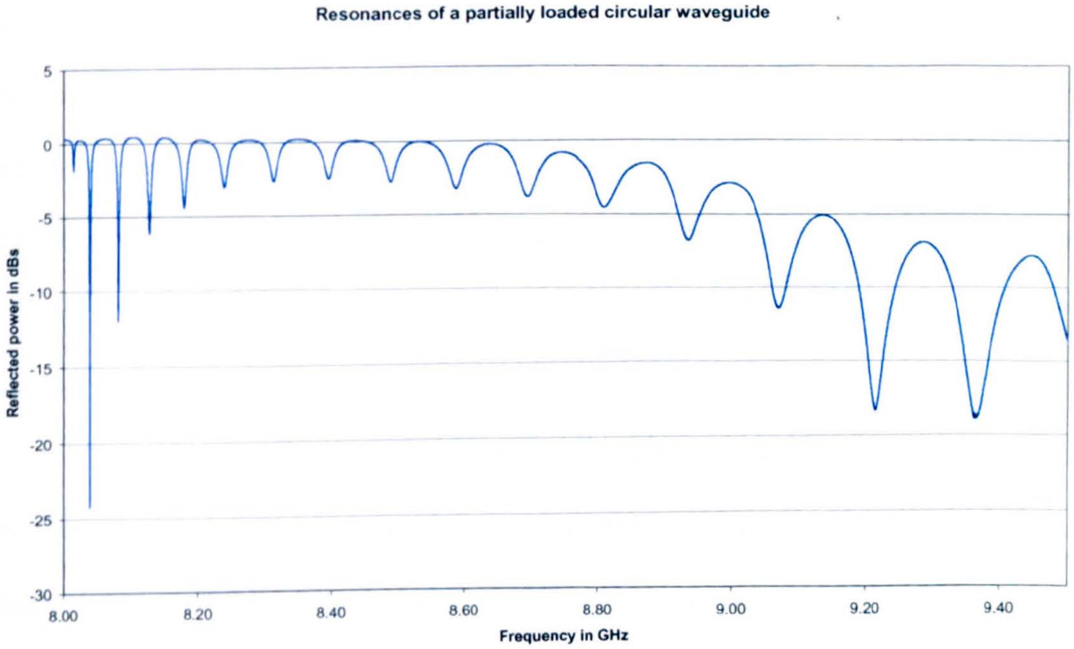

Figure 11.2. Typical example of the resonances appearance inside a partially loaded cavity.

The results of the measurement of the dispersion curve are shown in Figure 11.3 as the orange colour squares. Also shown are the results of various theoretical calculations of the dispersion curve.

The central solid line is the output of the software package CONCERTO with input parameters, $\varepsilon_r=10$, a=7.35 mm and b=10.0 mm (internal and external radii of Al_2O_3 tube). The small blue circles show the output of a MathCAD program based on a theoretical solution of Maxwell's equations for this system. The agreement between the Concerto simulation and the theoretical prediction of the MathCAD program is excellent. Also shown as the magenta coloured line is the output of the MathCAD program with $\varepsilon_r=9.0$ again but now with a=7.35 mm and b=10.0 mm, and the bottom line is the dispersion for $\varepsilon_r=10$, a=7.25 mm (0.1 mm smaller than the other two cases) and b=10.0 mm as before, to illustrate the effects of changing the dielectric constant, and changing the internal diameter of the tube. Note that changing the external diameter of the tube has a similar effect to changing its internal diameter since it is the ratio of b to a that controls the shape of the dispersion curve.

The experimental cut off appears to be approximately 7.9 GHz, which would indicate that the dielectric constant of the alumina is slightly greater than 10, or the internal diameter of the tube is slightly less than the value measured at its ends.

Alfa quote a tolerance of ±5% on diameter i.e. the internal radius should be a=7.50 ±0.38 mm but this is over a collection of tubes; over a single tube a deviation of ±0.1 mm along the length might be expected, so an internal radius of 7.35±0.10 mm is not unexpected with $\varepsilon_r=10$. Note that if ε_r was 9.2 as quoted by Alfa, then a would have to be 7.17 mm which is only just inside their tolerance range from 7.12 mm to 7.88 mm.

Thus the cut off frequency suggests that the dielectric constant of the material is 10.0 ± 0.1 in reasonable agreement with other observers.

However, the experimental dispersion curve (orange line) has a much greater slope than all the other theoretical curves and could not be matched by any sensible combination of tube dimension and dielectric constant. One possible explanation could be that the assignment of the resonant frequencies to n values has been done incorrectly because the first few resonances have been missed. If this were so, the experimental dispersion curve should be shifted to the right along the wavenumber axis. An attempt was made to obtain a match with the theoretical curves by shifting by 1, 2, 3, etc resonances, but since the slope of the experimental plot is so high, it is never possible to obtain a match. Another possibility is that the measured length of the cavity L could be different from its effective length due to the short circuits at the end of the cavity not being perfectly conducting. It is possible to obtain an excellent match by making the effective length of the cavity 250mm compared to its actual measured value of 301mm, but this is a much greater difference than could reasonably be expected. There is also the possibility that the small air gap between the alumina tube and the copper waveguide has a serious effect on the theoretical dispersion curves. However, in this case the gap was only 0.2 ± 0.1 mm and consequently was assumed to have little effect.

The large difference in the experimental dispersion relation in comparison with the theoretical models immediately suggested why it had not been possible to achieve synchronism in either of the Cerenkov experiments at the required frequency – because the slope of the dispersion curve was actually much steeper than expected and hence a much higher acceleration voltage would be needed to operate at any given frequency.

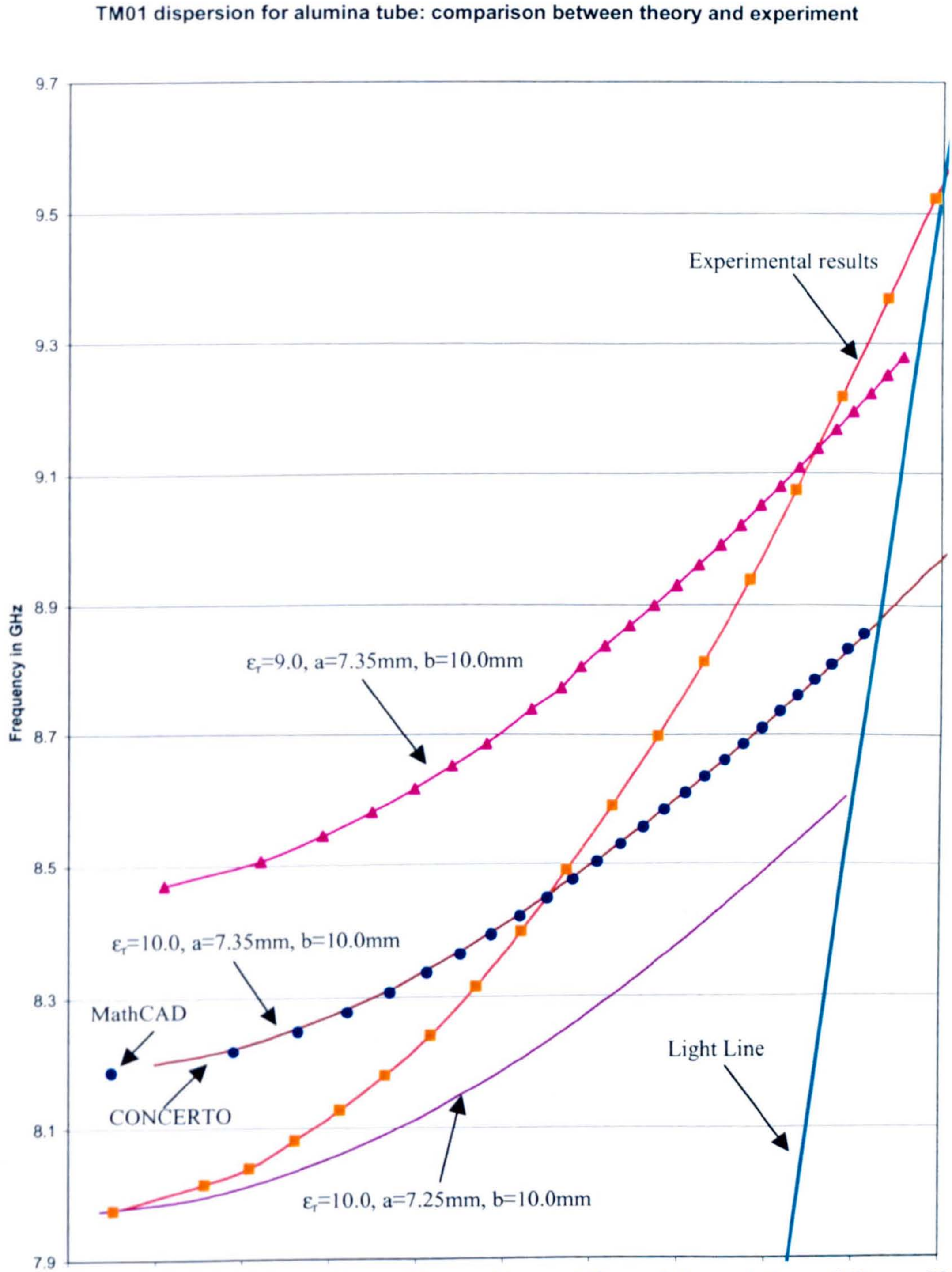

Figure 11.3. Theoretical and experimental dispersion curves for TM_{01} mode for an alumina tube.

It was clearly necessary to perform more experiments to try to understand why the experimental results were so different than the theoretical predictions.

11.4. Further experiments

In order to check to see if the experimental technique was satisfactory, the dispersion characteristics of an empty and fully loaded guide were measured. PTFE and nylon were chosen as suitable loading materials and therefore rods of the correct diameter, b, were manufactured. A solid rod of alumina was also generated consisting of one tube inserted into another and a central rod fitted to complete the solid structure. The results of the measurements are shown in Figure 11.4. The points represent experimentally measured TM_{01} resonances while the line represent the theoretical prediction, (which now is a standard analytical result),

$$\omega = \sqrt{\omega_{co}^2 + \left(\frac{c}{\sqrt{\varepsilon_r}}\beta\right)^2} \qquad 11.3$$

$$\text{i.e. } \omega = \sqrt{\left(\frac{2.405}{b}\cdot\frac{c}{\sqrt{\varepsilon_r}}\right)^2 + \left(\frac{c}{\sqrt{\varepsilon_r}}\beta\right)^2} \qquad 11.4$$

for TM_{01} modes in a totally loaded guide.

As can be seen there is a good agreement for the empty guide and the PTFE and nylon loaded cases. The dielectric constants used for the theoretical dispersion curves were normally accepted values: 2.05 for PTFE [51,52,53,54], and 2.95 [52,53] for nylon. These results suggest that the measurement technique was satisfactory. However, again there is a clear and serious discrepancy in the alumina case. To achieve a match at the cut off, a dielectric constant of 8.0 rather than 10 had to be used, but more importantly, the slope of the dispersion curve was again much greater than predicted theoretically. A much better fit could be obtained by assuming an unrealistically small value for the length of the composite rod as before, which has the effect of stretching the experimental dispersion curve along the wavenumber axis.

11.5. The anisotropy hypothesis

An examination of Equation 11.3 suggests that another possible explanation could be that the cut off frequency is controlled by one value of dielectric constant ε_{co}, while the wavenumber dependent term is controlled by another ε_β so that,

$$\omega = \sqrt{\left(\frac{2.405}{b}\cdot\frac{c}{\sqrt{\varepsilon_{co}}}\right)^2 + \left(\frac{c}{\sqrt{\varepsilon_\beta}}\beta\right)^2} \qquad 11.5$$

By setting $\varepsilon_{co}=8.0$ and $\varepsilon_\beta=4.7$, a good fit can be obtained between the experimental results as shown in Figure 11.5. This agreement strongly suggested that alumina in the form of tubes may be anisotropic as far as its dielectric constant is concerned. Anisotropic grain growth has been observed in alumina ceramics [55] but for plate shaped samples rather than tubes. A similar effect has been observed in Si_3N_4 ceramic where elongated grains were preferentially orientated parallel to the casting direction.

Maxwell's equations have been solved for a cylindrical metal waveguide totally filled with a dielectric material having dielectric constants $\varepsilon_{//}$ along the axis of the guide and $\varepsilon_\perp$ in the transverse plane.

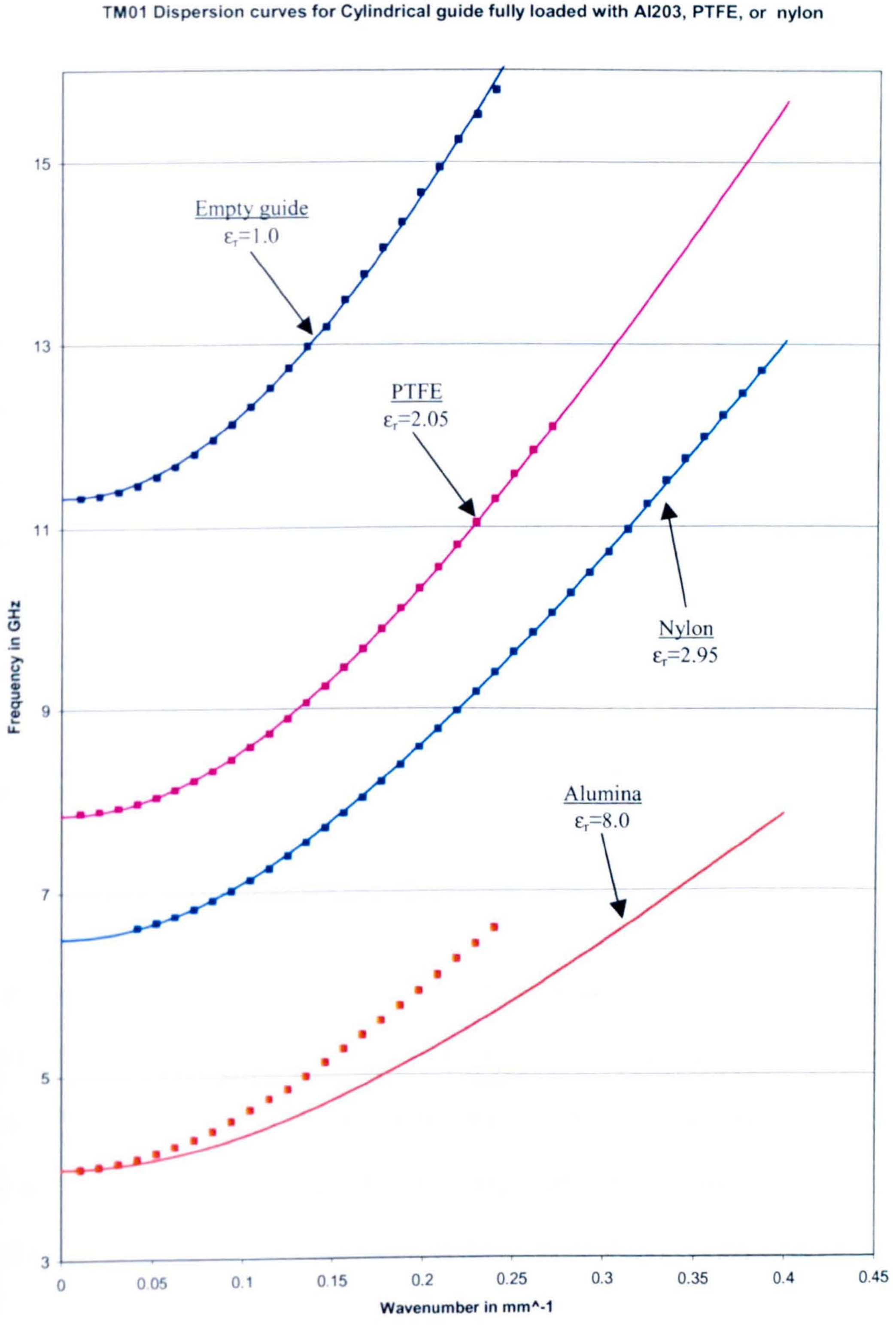

Figure 11.4. Theoretical and experimental TM_{01} dispersion curves for empty, alumina, PTFE and nylon mediums (fixed dielectric constant).

The results of this calculation for the TM_{01} mode give

$$\omega=\sqrt{\left(\frac{2.405}{b}\cdot\frac{c}{\sqrt{\varepsilon_{//}}}\right)^2+\left(\frac{c}{\sqrt{\varepsilon_{\perp}}}\beta\right)^2} \qquad 11.6$$

for the dispersion. This indicates that for the alumina tubing $\varepsilon_{//}=\varepsilon_{co}=8.0$ and $\varepsilon_{\perp}=\varepsilon_{\beta}=4.7$.

Figure 11.5 shows the application of this formula to not only the PTFE and nylon filled guides, but to the empty guide too. For the empty guide, the initially best fit was obtained for $\varepsilon_{co}=0.99$ and $\varepsilon_{\beta}=1.05$. These values indicate the magnitude of the errors involved in the method i.e. ± 5%. For PTFE, the values are $\varepsilon_{co}=2.07$ and $\varepsilon_{\beta}=1.98$, which in view of the empty guide results indicate that PTFE is essentially isotropic. There might appear to be some evidence of anisotropy in nylon with $\varepsilon_{co}=3.0$ and $\varepsilon_{\beta}=2.85$, but since $\varepsilon_{co}=\varepsilon_{\beta}=2.93 \pm 2\%$, the evidence is weak.

An analysis has also been carried out for the dispersion characteristics of the TE_{11} mode for an anisotropic dielectric loading. In this case, we find that

$$\omega=\sqrt{\left(\frac{1.841}{b}\cdot\frac{c}{\sqrt{\varepsilon_{\perp}}}\right)^2+\left(\frac{c}{\sqrt{\varepsilon_{\perp}}}\beta\right)^2} \qquad 11.7$$

i.e. since the electric field is transverse only the transverse dielectric constant is involved in the dispersion formula. Figure 11.6 gives the results of measurements made to examine the TE_{11} mode resonances. For an empty guide and the PTFE case, the values of ε_{co} and ε_{β} are equal to within the experimental accuracy of ± 5%. However, for alumina, the values of ε_{co} and ε_{β} are not equal as would be expected if the material was uniaxial (i.e.

having $\varepsilon_{//}$ and $\varepsilon_{\perp}$ only) and are seriously different as well with $\varepsilon_{co}=5.9$ and $\varepsilon_{\beta}=7.3$. This evidence suggests that the anisotropy theory is untenable.

11.6. The gap hypothesis

In all the experiments reported so far it has been assumed that the dielectric rods or tubes were a tight fit in the copper waveguide. This was true for the cases of the PTFE and nylon rods, which were machined to the correct diameter so that a tight fit with the copper waveguide was possible. For the case of the alumina though, it was not possible to match the size of a standard alumina tube to that of a standard copper pipe without leaving a very small gap, around 0.2 mm wide between the outside of the alumina tube and the inside of the copper waveguide wall. Since the gap represents only 1% of the diameter of the copper tube, it was felt initially that the error in ignoring its effect would be similarly small. In this section the effect of having a small air gap between the dielectric liner and the waveguide is taken into account.

Checking this assertion that a small gap could have an effect is not easy because finding the dispersion relationship for a dielectrically loaded guide with a gap between the dielectric liner and the waveguide is a difficult theoretical problem. This is because the dispersion relation is given by an equation of the sort,

$$\det \underline{A} = \underline{0} \qquad 11.8$$

where $\underline{A}$ is 5x5 matrix of terms involving Bessel functions.

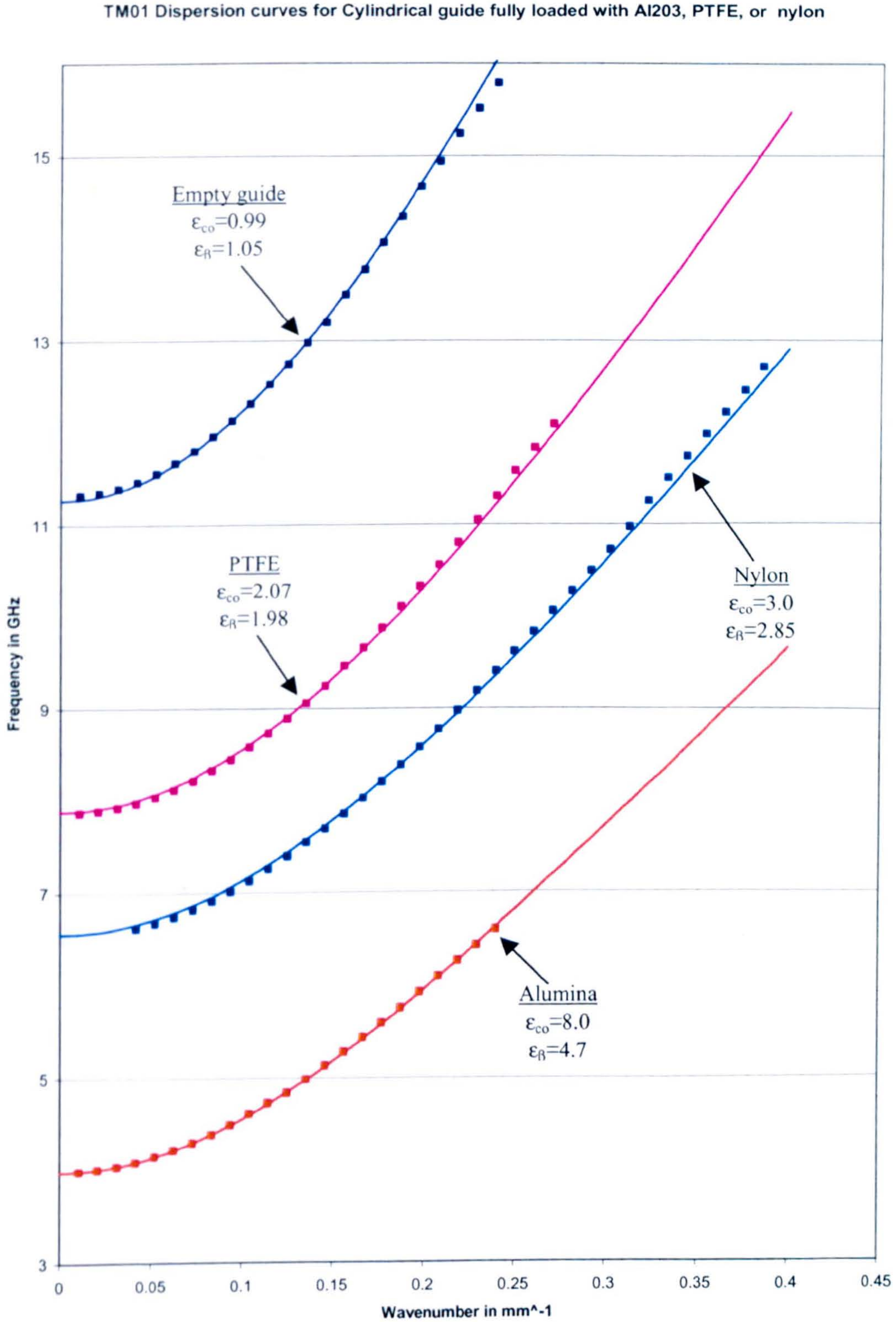

Figure 11.5. Theoretical and experimental TM01 dispersion curve for empty, alumina, PTFE and nylon loaded guide (varying dielectric constant).

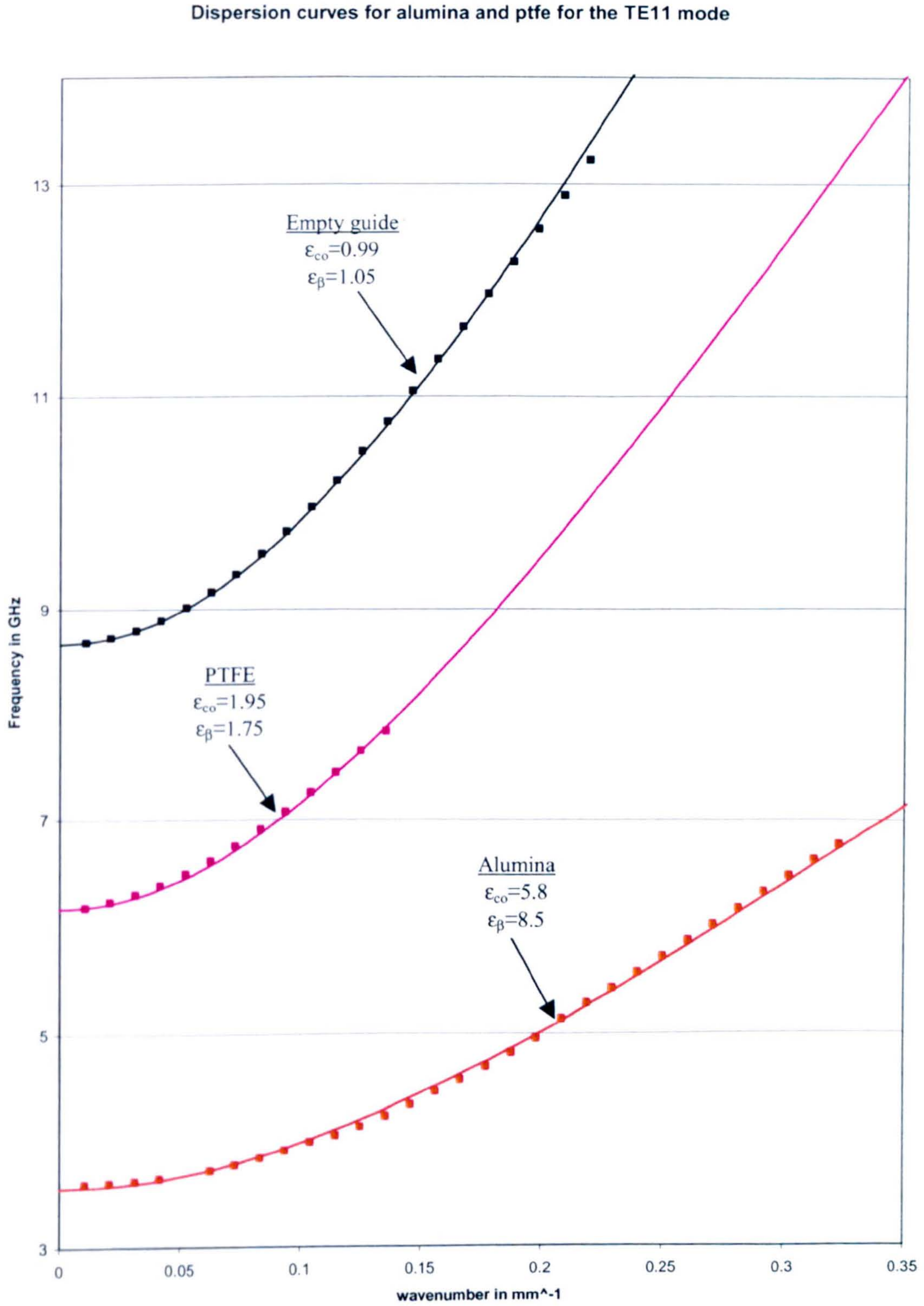

Figure 11.6. Theoretical and experimental TE_{11} dispersion curves for empty, alumina and PTFE loaded guide (varying dielectric constant).

Although many of the elements of the matrix are zero, the above equation when expanded still represents 16 terms on the left hand side (each composed of the product of 5 Bessel function values) compared with only 2 terms for the non-gap case, where each is composed of the product of only 3 Bessel function values. An alternative method of solution is to use CONCERTO. However, if sufficient mesh points are provided in the gap to give a satisfactory accuracy, the execution time becomes extremely long.

The results of two simulations on systems with similar dimensions to the one measured experimentally can be seen in Figure 11.7. The simulation taking into account the gap (solid line) does have a severe effect on the dispersion curve although the gap is small. The slope of the dispersion curve is increased markedly in comparison with the simulation ignoring the gap (dotted line). The shape of the solid line is now very similar to that of the dispersion curve observed experimentally (dots). The only difference between the experimental results and the simulation results with a gap is probably due to the fact that the dielectric constant used in the simulation is different from the real value.

To confirm the gap effect on the dispersion curve practically rather than computationally, a layer of conductive silver paint was applied to the outer surface of the alumina tube. The results of measuring the resonances of this structure are in Figure 11.8. There is now excellent agreement with the no – gap theoretical curve. Also the more layers of paint applied on the alumina tube the better the fit between the curves. Since the silver paint was not a very good conductor, a relatively thick layer had to be applied to simulate a metal guide. For the results shown in Figure 11.8, five layers of paint were applied. The only adjustable parameter used was the value of the dielectric constant, ε_r = 9.0, which was satisfyingly close to the manufacturer's specification of 9.2.

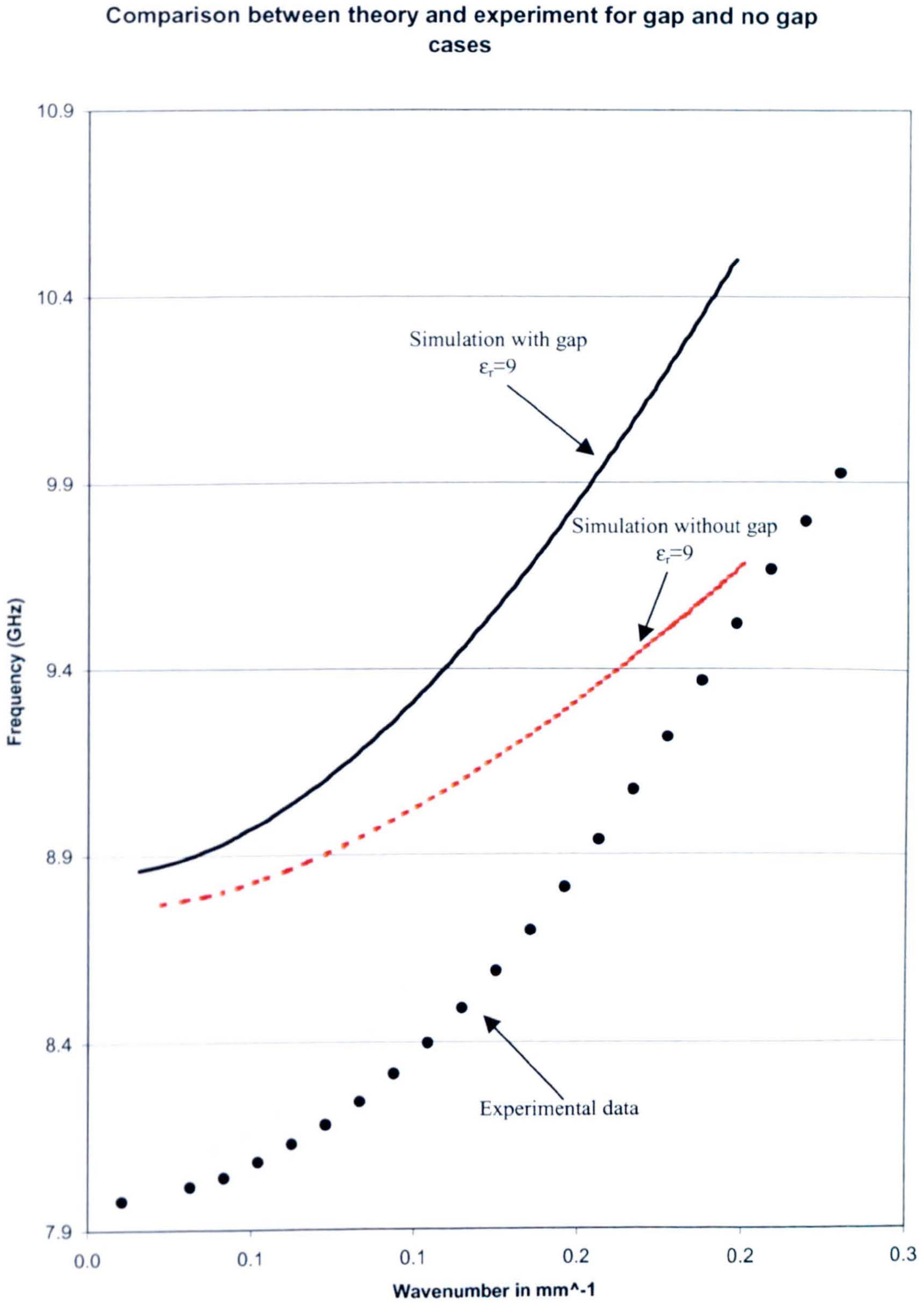

Figure 11.7. Graph that shows the effect of a small gap in a dielectrically loaded cavity.

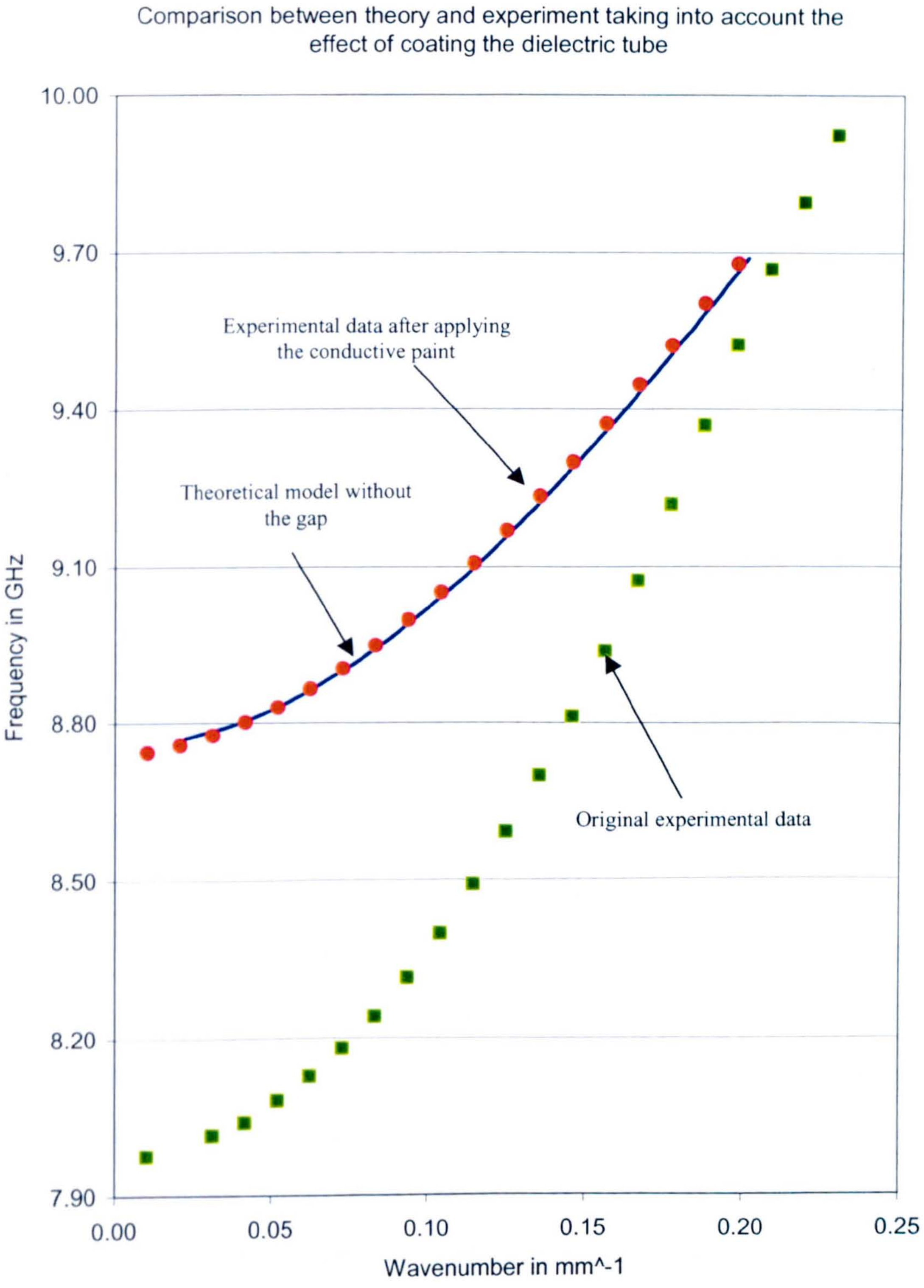

Figure 11.8. Graph proving that the elimination of the gap using layers of conductive paint matches the experimental data with the theory.

Chapter 12

Conclusions and Future Developments

12.1. Discussion and conclusions

This thesis has been concerned with the design, development and construction of a Cerenkov Free Electron Laser. This device has some important advantages over the more conventional FELs, chief of which is that it is simpler to construct. Its main element is a dielectric liner inserted inside a copper pipe. This takes the place of the expensive and difficult to construct wiggler magnet in a standard device. The initial reaction of the high power microwave tube world to Cerenkov devices, however, has been guarded – their suggestion being that there is a strong possibility electrons scattered from the beam could charge up the surface of the dielectric. If this charge were non-uniformly deposited along the surface of the liner, then the electron beam would be deflected off axis, seriously reducing the interaction and increasing the beam current necessary for the oscillations to start. A major purpose of this thesis was to investigate this assertion.

Two different systems were designed and built. By using a solenoid, it was found that under pulsed conditions, provided the direction of the electron beam was aligned accurately with the axis of the liner-waveguide system, a high percentage of the electron beam could be transported from one end of the liner to the other, so that electron charging effects do not seem to be a problem. This is in agreement with the work of MacDermott and his co-workers on dielectrically loaded gyrotrons [56]. However, disappointingly, no microwave output was observed even at maximum electron beam current for either system. This was in spite of the fact that the second system was specifically designed to have a very high small signal gain so that even if the combined losses in the waveguide and the dielectric liner were much higher than expected, the device should have been capable of oscillation using the available electron beam current.

Due to the fact that the diameter of the liner was much smaller for the second design, so that a more critical lining up procedure was required, it was decided to move the whole system into a horizontal position. This allowed a more accurate adjustment of the solenoid in order to achieve a high percentage of electron beam transportation. No serious differences in electron beam transport were observed compared with having the system in a vertical position. This was as expected since the earth's magnetic field is very small in comparison with the field strength of the solenoid. Also, for this new system it was decided to couple out power from the end of the system opposite to the electron gun using a metal probe connected to a standard N-type connector, rather than having a coupler attached to the side of the cylindrical waveguide. This meant that there had to be one method for checking the electron beam transportation and another for extracting the power from the resonant cavity. It was found impossible to incorporate both these systems in a single design simultaneously. However, it was found possible to first line up the electron beam, then de-mount the apparatus to attach the coupling device, and then re-position the solenoid accurately by means of two stands supporting the solenoid.

In view of the lack of microwave output in spite of the high electron beam current along the length of the liner, various possibilities were checked. From the theory point of view these included the small signal gain and the dispersion curve calculations. These depend for their accuracy on the value of the dielectric constant of the liner material and its loss tangent. Consequently, it was decided to try to determine the dielectric constant experimentally, and at the same time check out the calculations of the dispersion curve by measuring the resonances of closed section of dielectrically lined waveguide. A sample resonant cavity was constructed and tested. For an alumina liner, it was concluded that the TM_{01} mode resonance frequencies did not follow the predicted theoretical values. To check that the experimental technique was accurate, the dispersion relation of other materials was measured. These dispersion relations followed closely the theoretical model.

After considering several explanations for this discrepancy, it was found that the existence of a small gap between the alumina liner and the copper waveguide was responsible even though in our case this gap was only about 0.1 mm in thickness. In order to eliminate this gap a conducting layer was applied to the surface of the dielectric with silver paint. A good agreement between the experimental and the theoretical results was then achieved. Without this conducting layer, the dispersion curve was such that to achieve synchronism in either of our Cerenkov systems would have required a much higher electron beam accelerating voltage than was available, and consequently this explained the lack of microwave output from the both devices.

12.2 Future work

An important advance would be made if it were possible to design for our second system a means of checking both the transportation of the electron beam through the liner and the microwave output simultaneously.

Clearly, an immediate first step should be to coat an alumina liner with silver paint and then set up either one of the Cerenkov systems described in this thesis to see if some microwave output could be achieved. Preferably, the second Cerenkov system should be employed, since there is still no accurate information about the loss tangent of our sample of alumina used for the liner at X band microwave frequencies. It is anticipated that this simple alteration would achieve a successful interaction between the electron beam and the electromagnetic wave inside the loaded cavity at the required frequency and electron beam accelerating voltage. Consequently, measurements could then be made of the small signal gain of the device by measuring the rate of increase of microwave output with time as it grows from noise. How the gain is affected by various parameters such as electron beam current and accelerating voltage could also be investigated. Wright [57] has examined the jitter in the time for the microwave output to reach saturation after switch on in a standard FEL due to the random nature of the build up of oscillation from noise. Similar observations could be made with an operating Cerenkov device.

Chapter 13

List of Publications

[1] C. Petichakis, R. A. Stuart, C. C. Wright, A. I. Al-Shamma'a, J. Lucas, *Development of an X-band Free Electron Maser Output Coupler*, Proc. of the 15th Vector Fields European User Meeting, Chalmers Institute of Technology, Goteborg, Sweden, 2001.

[2] C. C. Wright, R. A. Stuart, C. Petichakis, A. I. Al-Shamma'a, J. Lucas, *Cut-off mode suppression in a waveguide FEM oscillator*, Nucl. Instr. and Meth. A 483, 2002, 235.

[3] C. Petichakis, R. A. Stuart, C. C. Wright, A. I. Al-Shamma'a, J. Lucas, *The Cerenkov Free Electron Maser*, Proceedings Strathclyde University, Strathclyde, Scotland, 2002.

[4] C. Petichakis, R. A. Stuart, C. C. Wright, A. I. Al-Shamma'a, J. Lucas, *The dispersion relation for a cylindrical Cerenkov Free Electron Maser*, Nucl. Instr. and Meth A, accepted for publication, 2003.

[5] C. C. Wright, R. A. Stuart, C. Petichakis, J. Lucas, A. I. Al-Shamma'a, *Design and construction of a table top microwave free electron maser for industrial applications*, to be published in vacuum, 2003.

[6] C. Petichakis, R. A. Stuart, J. Lucas, A. I. Al-Shamma'a, *The effect of a gap between dielectric and waveguide on the dispersion relation of the Cherenkov device*, to be published in vacuum, 2003.

Chapter 14

References

[1] J. Lucas and R.A. Stuart, *The Free Electron Laser - An Introduction*, DTI Contract No. EC/0124/87, 1987.

[2] M. Kong, *The Design of a Microwave Industrial FEL*, Ph.D. thesis, University of Liverpool, 1991.

[3] G. Dearden, *The Industrial Free Electron Laser*, Ph.D. thesis, University of Liverpool, 1993.

[4] E. G. Quirk, *A Pre Bunched Free Electron Laser*, Ph.D. thesis, University of Liverpool, 1994.

[5] A.I. Al-Shamma'a, *Wiggler System for an Industrial Free Electron Laser*, Ph.D. thesis, University of Liverpool, 1994.

[6] A. Shaw, *The Realisation of an Industrial Free Electron Laser*, Ph.D. thesis, University of Liverpool, 1995.

[7] C. Balfour, *The Design of a Backward Wave Free Electron Laser*, Ph.D. thesis, University of Liverpool, 1996.

[8] C.C. Wright, *Development of a Free Electron Maser for Industrial Applications*, Ph.D. thesis, University of Liverpool 2000.

[9] R. Kompfner, *The Travelling Wave Tube as Amplifier at Microwaves*, Proc. IRE, 35, 124-127, February 1947.

[10] M. Chodorow and R.A. Craig, *Some new Circuits for High Power Travelling Wave Tubes*, Proc. IRE, 45, 1106-1118, August 1957.

[11] J.V. Jelley, *Cerenkov Radiation and its Applications*, Pergamon press, 1958.

[12] I. Frank and I. Tamm, *Theory of the Coherent Radiation of Electrons moving in a Medium*, C.R.Ac.Sci.U.S.S.R, 14, 109, 1937.

[13] Pavel A. Cerenkov, *Radiation of Particles moving at a Velocity exceeding that of light, and some of the possibilities for their use in Experimental Physics*, Nobel Lecture, December 11, 1958.

[14] R. A. Stuart, *Calculation of the Dispersion Relation for a Partially Filled Cylindrical Waveguide*, University of Liverpool, 2000.

[15] MathWorks inc, *The Student Edition of MathCAD*, Prentice Hall, 1992.

[16] N. Boutin, *RF Oscillator Analysis and Design by the Loop Gain Method*, Applied Microwave & Wireless.

[17] J. M. Madey, *Stimulated Emission of Bremsstrahlung in a Periodic Magnetic Field*, Journal of applied physics, 42, 1971.

[18] L. K. Grover, R. H. Pantell, *Simplified Analysis of Free Electron Lasers using Madey's Theorem*, IEEE journal of Quantum Electronics, 21, July 1985.

[19] C.D. Child, *Discharge from Hot Cathode*, Phys. Rev. 32, 492, 1911.

[20] R. A. Stuart, *Private Internal Report*, University of Liverpool.

[21] Unpublished EEV Internal Report, *Document A137-2-5 Issue 3*, EEV Ltd.

[22] http://www.leyboldvac.de.

[23] J. F. O'Hanlon, *A User's guide to Vacuum Technology*, John Wiley & Sons, 1980.

[24] R.T. Bayard and D. Alpert, *Extension of the Low Pressure Range of the Ionization Gauge*, April 13, 1950, Rev. Sci. Instr. 21.

[25] D. Alpert, *New Developments in the Production and Measurement of Ultra High Vacuum*, July 1953, Journal of Applied Physics, Volume 24, Number 7, p. 860.

[26] MDC catalogue, *Caburn Vacuum Components*, 1997/98.

[27] W. F. Brunner, T. H. Batzer, *Practical Vacuum Technologies*, 1965.

[28] J. B. Fuller, *An Introduction to Microwave Theory and Techniques*, Third Edition, Pergamon Press, 1990.

[29] S. Y. Liao, *Microwave Devices and Circuits*, Third Edition, Prentice-Hall, 1990.

[30] VectorFields, *CONCERTO manual*, 2001.

[31] K. S. Yee, *Numerical Solution of Initial Boundary Value Problems Involving Maxwell's Equations in Isotropic Media, IEEE Trans. Antennas Propagation*, Vol. 17, May 1966.

[32] C. Petichakis, et. al., *Development of an X-Band Free Electron Maser Output Coupler, Vector Fields European User Meeting Proceedings*, September 2001, Goteborg, Sweden.

[33] L. Brillouin, *A theorem of Larmor and Its Importance for Electrons in Magnetic Fields*, Physical review, Volume 67, 1945, p.260.

[34] J.F. Gittins, *Power travelling wave tubes*, The English Universities Press LTD.

[35] J.T. Mendel, C.F. Quate, W.H. Yocom, *Electron Beam Focusing with Periodic Permanent Magnet Fields*, Proceedings of the I.R.E.

[36] R. A. Stuart, *Internal Report on Mangetic Field Calculations*, University of Liverpool, 2001.

[37] J.W. Gewartowski, H.A. Watson, *Principles of Electron Tubes*, D. Van Nostrand Company, Inc.

[38] User Guide, *PE2D Simulation Package,* version 7.1.

[39] A.G.A.M Armstrong, C.S. Biddlecombe, *The PE2D Package for Transient Eddy Current Analysis*, IEEE trans. on magnetics, vol. Mag. 18, no. 2, March 1982.

[40] John D. Kraus, *Electromagnetics*, Forth Edition, McGraw Hill Int. Edition, 1992.

[41] YUASA, *Material Safety Data Sheet*, Form #853021, 2001.

[42] Alfa Aesar Catalogue, *Research Chemicals Metals and Materials*, 2002-2003.

[43] James W. Lamb, *Miscellaneous Data on Materials for Millimeter and Submillimetre Optics*, Institute de Radio Astronomie Millimetrique.

[44] R. A. Stuart, *MathCAD program*, University of Liverpool.

[45] S. Ramo, J. R. Whinnery, T. V. Duzer, *Fields and Waves in Communication Electronics*, Third Edition, Wiley, 1994.

[46] H.P. Freund, *Nonlinear Analysis of High-power Cherenkov Masers,* Phys. Rev. Lett., 65, nr 24, 2993, 1990.

[47] C. Petichakis, et. al., *The Dispersion Relation for a Cylindrical Cerenkov Free Electron Maser*, Nucl. Instr. and Meth. A, 2002.

[48] W. Main, et. al., *Electromagnetic Properties of open and closed Overmoded Slow-wave Resonators for Interaction with Relativistic Electron Beams,* IEEE Trans. Plasma Sci. 22, pp 566-576, 1994.

[49] M. N. Afsar, K. J. Button, *Millimeter-wave Dielectric Measurements of Materials*, Proc. IEEE, vol 73, no. 1, pp 131-153, Jan. 1985.

[50] G. J. Simonis, R. D. Felock, *Index of Refraction Determination in the Near-millimeter Wavelength Range using a Mesh Fabry-Perot Resonant Cavity*, Applied Optics, Vol. 22, No. 1, Jan. 1983.

[51] Rufus G. Fellers, *Measurements in the Millimeter to Micron Range*, Proc. IEEE, vol. 55, no. 6, pp. 1003=1014, Jun. 1967.

[52] J. R. Birch, J. D. Dromey, *The Optical Constants of some common Low-Loss Polymers between 4 and 40* cm^{-1}, Infrared Physics, Vol. 21, pp 225 to 228, 1981.

[53] M. Halpern, et. al., *Far Infrared Transmission of Dielectrics at Cryogenic and Room Temperatures: Glass, Fluorogold, Eccosorb, Stycast, and various Plastics*, Applied Optics, Vol. 25, No.4, 1986.

[54] R. W. Haas, P. Zimmermann, *22-GHz Measurements of Dielectric Constants and Loss Tangents of Castable Dielectrics at Room and Cryogenic Temperatures*, IEEE Transactions on Microwave Theory and Techniques, November 1976.

[55] M. Seabaugh, et. al., *Sintering Technology Inc*, pp 341-348, 1996.

[56] K. C. Leou, et. al., *Large Signal Characteristics of a Wide-band Dielectric-loaded gyro-TWT Amplifier,* IEEE Trans. on Plasma Sci., Vol. 24, No. 3, June 1996.

[57] C.C. Wright, et. al., *An Experimental Investigation into the Evolution of the Output of a Free Electron Maser Oscillator*, Nucl. Instr. and Meth. A, 475, 2001, 308.

Appendix A

The Scattering Parameters

A.1. Introduction

When operating at low frequencies, any linear network can be adequately represented in terms of the voltages and currents at its input and output ports, as shown in Figure A.1.

This network can be completely represented using its impedance parameters z, hence,

$$\begin{aligned} V_1 &= z_{11}I_1 + z_{12}I_2 \\ V_2 &= z_{21}I_1 + z_{22}I_2 \end{aligned} \qquad \text{A-1}$$

The impedance parameters can also be represented in a matrix form as follows,

$$Z = \begin{pmatrix} z_{11} & z_{12} \\ z_{21} & z_{22} \end{pmatrix} \qquad \text{A-2}$$

In the same way, the network could be represented by its admittance parameters y, so that

$$\begin{aligned} I_1 &= y_{11}V_1 + y_{12}V_2 \\ I_2 &= y_{21}V_1 + y_{22}V_2 \end{aligned} \qquad \text{A-3}$$

where the admittance matrix is given by,

$$Y = \begin{pmatrix} y_{11} & y_{12} \\ y_{21} & y_{22} \end{pmatrix} \tag{A-4}$$

However, at microwave frequencies it is more usual to use wave amplitudes than voltage and current values in order to describe the microwave fields. Therefore, the network shown in Figure A.1 can be represented using the transmitted and reflected wave amplitudes as shown in Figure A.2. In this diagram, "a" represents the wave amplitude incident in the network at each port, while "b" is the wave amplitude reflected by the port.

The transmitted wave "a" and reflected wave "b" are related by the scattering parameters as shown below,

$$\begin{aligned} b_1 &= s_{11}a_1 + s_{12}a_2 \\ b_2 &= s_{21}a_1 + s_{22}a_2 \end{aligned} \tag{A-5}$$

or in matrix form as,

$$\begin{pmatrix} b_1 \\ b_2 \end{pmatrix} = \begin{pmatrix} S_{11} & S_{12} \\ S_{21} & S_{22} \end{pmatrix} \begin{pmatrix} a_1 \\ a_2 \end{pmatrix} \tag{A-6}$$

or more concisely as

$$b = Sa \tag{A-7}$$

where a and b are the column vectors $\begin{pmatrix} a_1 \\ a_2 \end{pmatrix}$ and $\begin{pmatrix} b_1 \\ b_2 \end{pmatrix}$.

and S is the Scattering Matrix and is given by,

$$S = \begin{pmatrix} S_{11} & S_{12} \\ S_{21} & S_{22} \end{pmatrix} \tag{A-8}$$

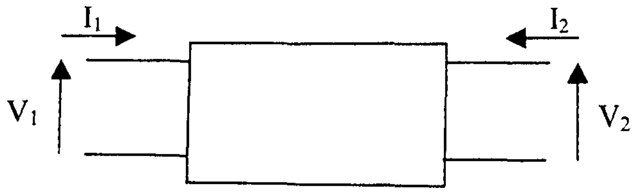

Figure A.1. A two port network.

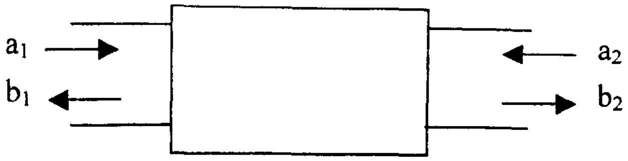

Figure A.2. Field representation of the two port network.

Equation A.7 can be expanded to any matrix size depending on the number of ports of the microwave network to be analyzed. In the same way, there is always a scattering matrix to represent any linear microwave network.

For the network shown in Figure A.2, if the two ports (input and output) are matched, then the scattering parameters for the network can be represented as follows,

$S_{11} = \frac{b_1}{a_1}$, where S_{11} is the input reflection coefficient

$S_{12} = \frac{b_1}{a_2}$, where S_{12} is the reverse transmitted coefficient

$S_{21} = \frac{b_2}{a_1}$, where S_{21} is the forward transmission coefficient

$S_{22} = \frac{b_2}{a_2}$, where S_{22} is the output reflection coefficient